ABSTRACT

Title of Dissertation: DESIGN AND CHARACTERIZATION OF AN ELECTROHYDRODYNAMIC (EHD) MICROPUMP FOR CRYOGENIC SPOT COOLING APPLICATIONS

Parisa Foroughi, Doctor of Philosophy, 2008

Dissertation Directed By: Professor Michael M. Ohadi
Department of Mechanical Engineering

High-temperature superconducting (HTSC) components are being incorporated into communication and monitoring electronic devices to increase their signal-to-noise ratio or their channel capacity. Those devices must be maintained at cryogenic temperatures to prevent the loss of their superconducting properties and retain their performance superiority. They are conventionally cooled via direct heat conduction, which leads to undesirable temperature differences among the various components being cooled. Compact micropumps capable of pumping liquid nitrogen at 77 K into liquid-cooling circuits would enable a much more compact and lightweight method of maintaining a uniform temperature across the cooling circuit. These pumps can also address the demand for delivering small doses of LN_2 to particular spots in bioengineering applications.

One of the main objectives of the present study was to develop an electrohydrodynamic (EHD) ion-drag micropump with LN_2 as the working liquid. EHD

ion-drag pumping phenomenon refers to liquid motion caused by an interaction between electric and hydrodynamic fields in a dielectric liquid.

To investigate the effect of each design parameter on the performance of the micropump, several prototypes with four distinct designs were fabricated and packaged. The designs included a variety of emitter shapes, inter-electrode spacings, electrode-pair spacings, and channel heights. The micropumps were tested at different DC voltages ranging from 0 to 2.5 kV. Two test rigs with novel measurement techniques were also designed, built, and calibrated to measure the generated static pressure head, electric current, and flow rate with an acceptable level of accuracy.

The relationships between pressure/current (P-I) and pressure/voltage (P-V) for various designs were investigated experimentally. The results showed good agreement with the general analytical trends reported for EHD pumping in the literature. The experimental results also demonstrated that electrode geometry and gaps are effective in determining the pressure onset voltage. The results also show that a maximum static pressure head of 160 Pa at 1400 V is achievable for a design with a combination of a 50-μm emitter-collector gap, a 200-μm electrode-pair gap, and a saw-tooth shaped emitter/flat collector.

DESIGN AND CHARACTERIZATION OF AN ELECTROHYDRODYNAMIC (EHD) MICROPUMP FOR CRYOGENIC SPOT COOLING APPLICATIONS

By

Parisa Foroughi

Dissertation submitted to the Faculty of the Graduate School of the
University of Maryland, College Park in partial fulfillment
of the requirements for the degree of
Doctor of Philosophy
2008

Advisory Committee:
Professor Michael M. Ohadi, Chair
Associate Professor Donald DeVoe
Professor Marino di Marzo
Associate Dean Gary A. Pertmer
Assistant Professor Bao Yang

DEDICATION

To my wonderful parents for their endless love and support

And

To my husband Reza for his continuing encouragement, support, and love

ACKNOWLEDGEMENTS

I would like to acknowledge, first and foremost, my academic advisor Dr. Michael M. Ohadi who always provided support and guidance and encouraged me to pursue my own interests throughout my entire graduate study.

I would also like to express my appreciation to the members of my advisory committee, Drs. Don DeVoe, Marino di Marzo, Gary Pertmer, and Bao Yang for their valuable time and helpful advice.

I would like to acknowledge a number of fellow scientists who assisted me in the technical aspects of my dissertation research, including, but not limited to, Drs. Amir Shooshtari, Serguei Dessiatoun, Yuan Zhao, John Lawler, Jianwei Qi, and Francis Franca.

I especially thank my wonderful friends and colleagues at the Smart and Small Thermal Systems Laboratory, both present and former, for their valuable technical and personal support. It was a true pleasure to work beside Vytenis Benetis, Sourav Chowdhury, Mihai Catalin Rada, Arman Molki, Jianlin Wu, Ebrahim Al-Hajri, Mohamed Alshehhi, Edvin Cetegen, and Elnaz Kermani.

I am grateful to Mr. Bernie LaFrance at the Engineering Machine Shop for providing technical assistance on manufacturing my first experimental test setup, and Mr. Thomas Loughran at the Maryland NanoCenter who assisted me with hands-on microfabrication processes.

I would also like to acknowledge the financial support of this project from AHX/EHD Consortium and ATEC, Inc.

I would like to thank my family for their unmatched love and support. Most of all, I thank my father, Mohammadreza, for his endless support and encouragement toward my higher education and my mother, Ashraf Sabbaghian, who always believed in me, and as my first teacher taught me that nothing is impossible if you believe in yourself. I am deeply grateful to my brother, Ali, and my sister, Mahsa, without whom life would be so meaningless.

And last but certainly not least, I would like to thank my husband, Reza Azarkhail, whom I first met during our graduate studies at UMD. Without all his help, encouragement, and constructive comments during our long hours of discussions, I could never have finished this work.

TABLE OF CONTENTS

LIST OF TABLES

LIST OF FIGURES

NOMENCLATURE

c_p	Specific heat [J/(kg.K)]
D	Diffusion coefficient (m^2/s)
e_0	Electronic charge, $1.60217646 \times 10^{-19}$ (C)
E_0	Characteristic electric field (V/m)
E_{val}	Energy of the valence levels broadening (eV)
$\mathbf{E}$	Electric field intensity (V/m)
$\mathbf{f_e}$	Electric body force (N/m^3)
g, $\mathbf{g}$	Gravitational acceleration (m/s^2)
Gr	Grashof number
h	Convective heat transfer coefficient ($W/m^2.K$)
I	Current (A)
I_g	Ionization energy of gas (eV)
I_l	Ionization energy of liquid (eV)
$\mathbf{J}$	Electric current density (A/m^2)
k	Thermal conductivity (W/m.K)
L	Characteristic length (m)
$\dot{m}$	Mass flow rate (kg/s)
p	Pressure (Pa)
P_r	Prandtl number
P_+	Polarization energy of cation (eV)
$\dot{Q}$	Heat transfer rate (W)

r_+	Cation radius (Å)
r_-	Anion radius (Å)
R	Cation radius (Å)
R	Electric resistance (Ω)
R_a	Rayleigh number
R_{air}	Gas constant [J/(kg.K)]
S_J	Joule heating source term (W/m^3)
t	Time (s)
T	Temperature (K)
u	Velocity (m/s)
U_0	Characteristic velocity (m/s)
V	Voltage (V)
$\dot{V}$	Flow rate (ml/min)
V_0	Conduction band energy in liquid (eV)

Greek Letters

α	Thermal diffusivity (m^2/s)
β	Coefficient of thermal expansion
ε	Permittivity (F/m)
ε_0	Vacuum permittivity, 8.86×10-12 (F/m) (or $C^2/(N.m^2)$)
ε_r	Relative permittivity (F/m)
η	Dynamic viscosity (Pa.s)
μ_e	Electric charge mobility ($m^2/V.s$)

μ_+	Cation mobility ($m^2/V.s$)
μ_-	Anion mobility ($m^2/V.s$)
v	Kinematic viscosity (m^2/s)
τ_e	Charge relaxation time (s)
ρ	Density (kg/m^3)
ρ_{e0}	Characteristic charge density (C/m^3)
ρ_e	Electric charge volume density (C/m^3)
τ_m	Mechanical transport time of ions (s)
σ_e	Electrical conductivity (S/m) (or $C^2.s/(kg.m^3)$)
φ	Work function of metal (eV)
Φ	Electric potential (V)

CHAPTER 1: INTRODUCTION

1.1. Background and Motivation

A new electronic era began with the discovery of high-temperature superconducting (HTSC) materials in 1987. HTSC components, which operate in temperatures from 20 K up to 138 K, are being incorporated into communication and monitoring electronic devices to increase their signal-to-noise ratio or their channel capacity. Those devices must be maintained at cryogenic temperatures to prevent the loss of their superconducting properties and retain their performance superiority. They are conventionally cooled via direct heat conduction to the cold fingers of a cryocooler, which limits their spatial configuration and can lead to undesirable temperature differences among the various components being cooled (Sugimoto et al. 2006, Walker et al. 1988, Foroughi et al. 2007).

Compact electrohydrodynamic (EHD) micropumps capable of pumping liquid nitrogen at 77 K into liquid-cooling circuits would enable a much more compact and lightweight method of maintaining a uniform temperature across the cooling circuit. Besides providing precise flow control, EHD pumps with no moving parts would not vibrate the electronic devices being cooled and would ultimately help isolate them from the typical mechanical vibrations of the cryocooler.

Although a significant amount of research has been conducted on the EHD pumping phenomena in ambient conditions, the author has found only a limited number of studies that used cryogenic liquids. Therefore, a thorough characterization of EHD micropumps for cryogenic applications is of vital interest to advancing the liquid cooling

technology for devices which contain HTSC materials, as well as the bioengineering applications where a small dose of LN_2 needs to be delivered to a particular spot.

The work summarized in this research focuses on demonstrating the feasibility of EHD ion-drag pumping phenomenon in liquid nitrogen and on studying the characterization of the micropump performance.

EHD ion-drag pumping phenomenon refers to liquid motion caused by an interaction between electric and hydrodynamic fields in a dielectric liquid. In an ion-drag pump, the ion-injection phenomenon is the key process for generating ions. The pumping effect occurs when a sufficiently-high electric potential difference is applied between a pair of electrodes, called the emitter and collector. The ions are generated mostly at the emitter/liquid interface and move towards the collector because of the electric body force (i.e. the Coulomb force). Friction between the moving ions and neutral molecules drags the working fluid and induces fluid motion.

For a successful pressure generation, the abundance of one ion polarity (i.e. unipolar condition) is preferred, since the generation of an equal number of ions of both polarities would result in no net pumping, as positive and negative ions offset the dragging action of each other. The charge injection process highly depends on the electrochemical characteristics of the working liquid, the electrochemistry of the electrode material, the strength of the electric field, and the electrode geometry. The right combination of those factors will ultimately establish a condition in which the metal/liquid energy barrier is overcome and a sufficient number of ions are generated to initiate the pumping process. This will in fact require a dielectric fluid with a large dielectric constant to sustain a strong electric field, an emitter electrode geometry that

locally intensifies the electric field (such as a saw-tooth geometry) at the metal/liquid interface, and a collector electrode that neutralizes the incoming flow of ions.

In this research, the micropump was composed of an alumina substrate on which gold electrodes of submicron thickness were deposited, a top-cover with an embedded channel and integrated inlet and outlet ports, and a bottom plate. All the components are bonded together by a cryogenic-compatible epoxy paste adhesive. Four designs of micropumps were selected to study the performance effect of various geometrical parameters. Those designs included various emitter shapes, inter-electrode spacings, electrode-pair spacings, and channel heights. The micropumps were tested in two test rigs at different DC voltages ranging from 0 to 2.5 kV. The first test rig was designed specifically to measure flow rate generation in a closed loop, while the other one was used to measure static pressure head and electric current

The present work extends the micropump research by Darabi (1999), Rada (2004) and Benetis (2005), former Ph.D. students and fellow researchers at the University of Maryland, to cryogenic applications. They developed several designs of micropumps, which were, for the most part, tested with HFE 7100. They demonstrated that incorporating saw-tooth emitters and increasing the number of stages could significantly improve the pumping performance and pressure generation. In addition, Rada (2004) investigated the EHD pumping of LN_2 using a meso-scale pump.

1.2. Dissertation Outline

This dissertation is divided into seven chapters. Chapter 2 reviews the fundamental operation mechanism of the EHD pumping followed by a selective literature survey of EHD ion-drag/ion-injection pumps in two main areas of application: ambient

temperature and cryogenic. Next, the physics of the EHD pumping phenomena, relevant governing equations, and a review of various controlling parameters on liquid nitrogen EHD pumping are presented.

In Chapter 3, the fundamentals of generation and transport of electric charge carriers in nonpolar liquids under the influence of intense electric field are reviewed, with emphasis given to the characteristics and behavior of liquid nitrogen, as it is the working fluid in this research. In particular, the energy barriers for positive and negative voltage polarities (i.e. field ionization and field emission, respectively) at different metal/liquid interfaces, i.e. Au/LN_2 and Au/Pt, are determined using the method suggested by Arii and Schmidt (1984).

The entire Chapter 4 is dedicated to the micropump design, material selection, fabrication methods, and packaging. Thin-film deposition and photolithography-etching techniques were employed to create several contiguous metallic electrode pairs (emitter and collector pairs) in a comb-like structure on the alumina substrate. The top-cover provides a flow channel as well as inlet and outlet ports. To evaluate the effect of various geometrical parameters on micropump performance, a series of micropumps with various electrode geometries and spacings are introduced for further tests and experimental investigations.

Chapter 5 introduces the two test rigs, which were designed and built for different measurement purposes, and explains the principle behind their operation. Experiments were performed by applying DC voltages to the micropumps while generated current and pressure were measured.

Chapter 6 covers the experimental results for onset voltage, pressure-current (P-I) characteristics, and pressure-voltage (P-V) characteristics. The P-I and P-V relationships show good agreement with the general analytical trends reported in the literature.

Finally, Chapter 7 draws conclusions, summarizes the key findings, and proposes future research directions.

CHAPTER 2: LITERATURE REVIEW - FUNDAMENTALS OF ELECTROHYDRODYNAMIC (EHD) PUMPING

This chapter introduces the fundamental principles and operating mechanism of the electrohydrodynamic (EHD) pumping phenomenon followed by a selective literature survey of the experimental and numerical studies of the EHD ion-drag/ion-injection pumps in two main areas of application: ambient temperature and cryogenic.

Next, the physics of the EHD pumping phenomena and its governing equations along with simplifying assumptions and modifications are explained. Finally, a review of various controlling parameters on liquid nitrogen EHD pumping and the relevant existing work in the development, optimization, and modeling of ion-drag pumps is provided.

In addition to the material presented in this section, introductory chapters from the dissertations of Rada (2004), Shooshtari (2004) and Benetis (2005) are recommended for more information on different aspects of the EHD phenomena.

2.1. EHD Pumping Phenomenon

2.1.1. EHD Definition

Electrohydrodynamics (also referred to as electrostrictive hydrodynamics studies) is the conversion of electrical energy into kinetic energy, and vice versa. It is a field of science that deals with the motions of ionized particles or molecules under the influence of electric field (Wikipedia, accessed October 2007).

EHD has many applications in different fields. In EHD pumps, the gradient of electric fields creates hydrostatic pressure (or motion) in dielectric media and produces

fluid motion. If the dielectric is a vacuum or a solid, no flow is produced. Common examples of EHD are air ionizers and EHD thrusters. In some cases, the reverse phenomenon can take place. For example, a powered flow of fluid within a well-defined electric field can add energy into the system. The excess energy will then be extracted as a potential difference by electrodes. In this case, the structure acts as an electric generator (Wikipedia).

In this research, only those motions that are produced by ion-drag / ion-injection mechanisms are reviewed. More comprehensive reviews on other types of EHD pumping devices such as conduction, induction and electrokinetic pumps can be found in the report by Ohadi et al. (2001), and dissertations of Rada (2004), Shooshtari (2004) and Benetis (2005).

2.1.2. EHD Ion-Drag Pumping

EHD ion-drag pumping refers to the liquid motion due to interaction of electric and hydrodynamic fields in a dielectric liquid. In an EHD ion-drag micropump, the pumping effect occurs when an electric potential difference is applied between the electrodes, called the emitter and collector. The ions are generated mostly at the emitter and move towards the collector due to the electric body force (mainly the Coulomb force). Friction between the moving ions and neutral molecules drags the working fluid and induces liquid motion.

In Figure 2-1, a simplified hypothetical model is given to show the LN_2 molecules' interaction with the metal electrodes. At the positive electrode, the fluid molecule loses an electron and becomes a positive ion, while at the negative electrode, it absorbs an electron and becomes a negative one.

For successful pumping, the abundance of one ion polarity is preferred since the generation of an equal number of ions of both polarities will lead to no net pumping. On the other hand, the ion generation process highly depends on the nature of the working liquid, the electrochemistry of the electrodes' material, the strength of the electric field, and the electrodes' geometry. The right collection of these factors ultimately establishes a net flux of one ion polarity (in this model, positive) from the emitter toward the collector, which drags the neutral molecules and creates a flow.

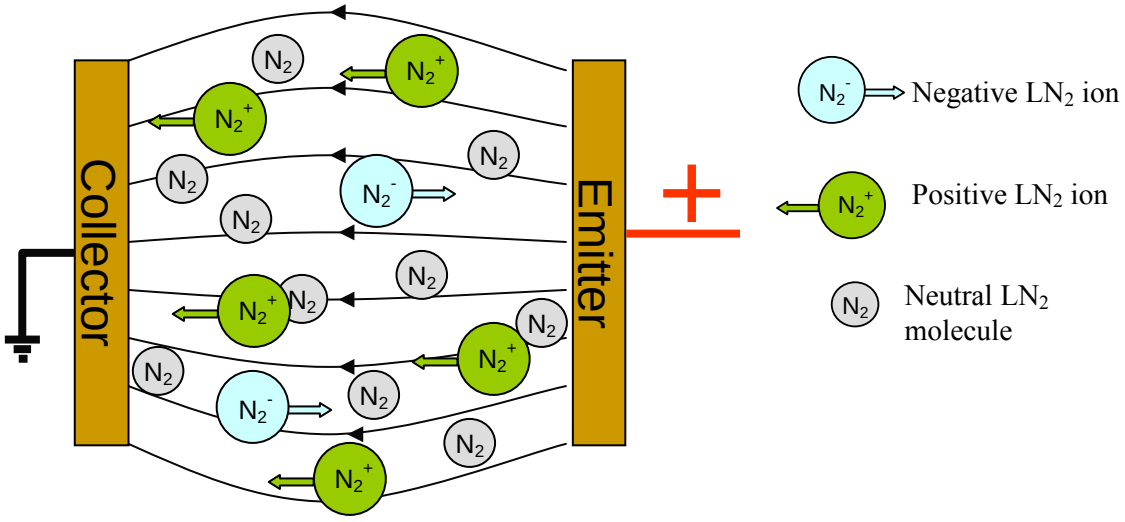

Figure 2-1 EHD ion-drag pumping mechanism

Over the past decades, various studies have been conducted to address the theoretical and experimental aspects of EHD pumping phenomena. The main objective of these studies was to improve the performance of EHD pumps by means of producing local, highly intensified electrical fields to generate a large number of ions with a certain polarity. This would be achieved by the right selection of working liquid and proper electrode design. A key issue here is that the two electrodes must be designed so as to

generate very different electrical field intensities; that is, ions with the same polarity are preferred since the movement of opposite ions would cause opposite movement in the fluid and result in less or no net pumping effect on the fluids. Therefore in most cases, as will be explained in section 2.1.3, the emitter electrodes were designed to have sharp features with low radii of curvature to increase the number of ions with one polarity, while the collector electrodes were kept smooth.

It should be noted that the ion-injection phenomenon is the dominant process for generating ions in the ion-drag pumps but not the only one. Charge injection occurs at the liquid/metal interfaces when the electric field is strong enough to overcome the fluid/metal energy barrier and generate the injection process with enough ions to initiate a pumping process instead of only generating electrochemical ions. This requires a dielectric fluid with a large dielectric constant, which helps sustain a strong electric field.

2.1.3. Ion-Drag Pumping History and Experimental Results

This section provides a selective literature survey of the experimental and numerical studies of the EHD ion-drag/ ion-injection pumps. Two main areas of ambient temperature and cryogenic applications are reviewed, either of which includes micro- and macro-scale pumps.

2.1.3.1. Ambient Temperature Applications

Macro- and meso-scale pumps

Electrohydrodynamic phenomena have been known since the 17th century; but it was not until the late 20's when Gemant (1929 as cited in Tobazeon 1984) brought up the hypothesis of liquid motion due to the presence of space charges between parallel plates. A few years later, Hofmann (1934, cited in Tobazeon 1984) reported a fluid motion under

a high step voltage. Avsec and Luntz described various flow patterns in insulating liquids calling them "electroconvective eddies" (Avsec and Luntz 1936, 1937, 1939 as cited in Tobazeon 1984). Ostroumov (1954, cited in Tobazeon 1984) introduced the first mathematical formulation of the phenomenon by combining the electrical conduction equations and the hydrodynamic (Navier-Stokes) equations. He identified the significance of the Coulomb force and concluded that a fluid subject to electric field cannot remain motionless.

Stuetzer and Pickard were amongst the firsts to investigate the EHD phenomenon as a pumping mechanism in the early 60's (Stuetzer 1959, 1960; Pickard 1963a, 1963b). Using a simplified model, they showed the following relationship between the maximum pressure inside an ion-drag pump and the electric field intensity:

$$P_1 - P_0 \propto \varepsilon(E_1^2 - E_0^2) \tag{2-1}$$

where P_1 and P_0 are the pressure, E_1 and E_0 are the corresponding field strength at the emitter and the collector, respectively, and ε is the permittivity of the liquid.

Stuetzer also demonstrated for the first time the I-V curve which distinguishes three distinctive regions of the current measurement vs. the applied voltage. His work was later expanded by Schmidt (1997).

Pickard (1963a) followed the terminology of Middendorf and Brown (1958), which divides the motion of a dielectric liquid under electric field into two categories: *co-field* when the motion is along the electric field lines; and *cross-field* when the motion is perpendicular to the field lines. In this research, only co-field motions which are produced by ion-drag mechanism are reviewed.

Melcher (1981) performed a series of theoretical studies on continuum electromechanics, which were published in his book, *Continuum Electromechanics*. He determined solutions for the space charge density and the electric field distribution based on two different analyses. Most of the assumptions made by Stuetzer and Pickard were included in his analyses. However, Melcher's analyses were more general as he presented his results in nondimensional forms. He was the first to nondimensionalize the EHD governing equations. He introduced a new dimensionless parameter, the so-called electric Reynolds number, which affects the pressure generation and efficiency of the pumps working with DC voltage.

During the last few decades, numerous studies have been devoted to the development and behavior of macro- and meso-scale ion-drag pumps. Many researchers, such as Sharbaugh and Walker (1985), Bryan and Seyed-Yagoobi (1991, 1992), Barbini and Coletti (1995), Asano and Yatsuzuka (1999), Bologa et al. (2000), Yanada et al. (2002), and Rada (2004), studied different electrode designs and their effect on the pumping performance. Their designs included screen electrodes with sharp points, ring-needle electrodes, punched-hole plate/screen electrodes, needle-cylinder electrodes, wire-mesh electrodes, needle-mesh electrodes, and crown-shape needle/ ring electrodes, respectively. They showed through experiments that the electrode geometry and working liquid are the prominent factors determining the pump performance. Some of the issues common in most studies were the lack of repeatability of the test results and most often the short lifetime of the specimen. These problems could be due to many known and unknown factors affecting the pumping environment such as electrochemical reactions between electrodes and working liquid, which causes permanent damages (i.e. corrosion,

etc.) to the electrodes. Many researchers, such as Crowley et al. (1990), Bryan and Seyed-Yagoobi (1991), and Coletti and Bozzo (1996) and Yanada et al. (2002), studied the effect of working liquid properties on the pumping performance through experiments and different electrode geometries. More on this topic can be found in Chapters 3 and 4.

Micro-scale pumps

The major drawback of the meso- and macro-scale EHD pumps is their need for a high operational voltage (typically above 10 kV), which eliminates many potential applications. During the last decade, improvement in microfabrication techniques has allowed researchers to greatly reduce this voltage by fabricating micron-sized electrodes and electrode gaps, resulting in development of EHD micropumps.

By incorporating MEMS techniques, Richter and coworkers built the first successful grid-type EHD ion-injection micropump (Richter et al., 1991). Their pump consisted of two opposed grids which were covered by gold, micromachined on single crystal silicone substrates, and bonded together anodically. The distance between grids was 350 μm and the total grid area was 3 x 3 mm^2. A maximum pressure head of 2500 Pa was reported at 700 V with ethanol as the working fluid. A flow rate of 14 ml/min at a pressure of 420 Pa was also achieved.

Wong and co-workers (1995) developed an EHD injection micropump using laser micromachining technology. They fabricated two different designs. The first design had two silicon substrates with etched and laser-drilled holes stacking on the top of each other. Gold was deposited on one side to act as the electrode. The second design had the silicon substrates oriented back-to-back and bonded together. The back-to-back design

decreased the grid distance and the required voltage for pumping. They reported a pressure head of 287 Pa with an applied voltage of 120 volts.

Ahn and Kim (1998) used the microfabrication advances to fabricate the first planar ion-drag micropump, which consisted of 30 stages of gold-coated electrode pairs in a 3-mm wide channel with a channel height of about 200 μm. The gap between stages was 200 μm, while the gap between each emitter and collector was kept at 100 μm. A flow rate of 55 μl/min with ethyl alcohol was reported at a positive DC voltage of 120 V. Also, a maximum pressure head of 225 Pa was obtained at 100 V with a current of about 3 mA.

Darabi et al. (2002) designed a micropump with planar electrodes and 3D features in order to maximize the local electric field responsible for the EHD pumping. They proposed several different electrode designs, including flat electrodes, saw-tooth electrodes, and electrodes with 3D bump structures. They tested a micropump with 50-μm electrodes gap using HFE 7100 as the working fluid and reported a pressure head of 800 Pa at a DC voltage of 700 V.

Benetis et al. (2003) continued the work of Darabi and co-workers and evaluated the effects of inter-electrodes spacing, electrode pair spacing, and pump channel height on the pumping performance of the micropump. They demonstrated with many tests using HFE 7100 as the working fluid that saw-tooth emitters and increasing the number of stages can significantly improve the pumping performance and pressure generation. They reported a flow rate of about 8 ml/min at a DC voltage of 500 V. A typical design of their micropump substrate and its electrodes is shown in Figure 2-2. Later Benetis in

his Ph.D. dissertation (2005) reported comprehensive experimental and numerical studies on different designs of the micropump.

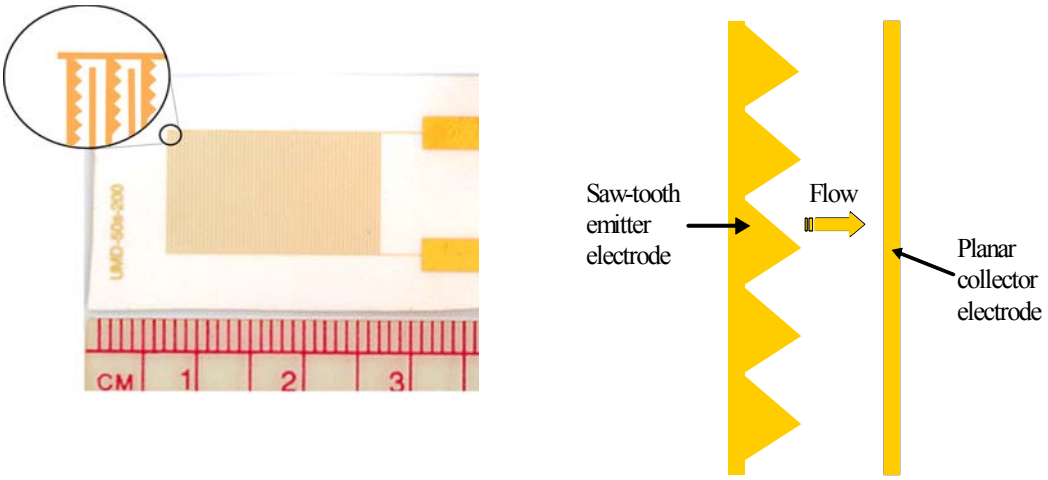

a) Picture of a micropump substrate

b) Schematic diagram of a saw-tooth shape emitter and a planar collector

Figure 2-2 Picture of a micropump substrate and its electrodes (Benetis et al. 2003)

Yang et al. (2003) fabricated an ion-drag micropump with indium-tin-oxide (ITO) planar electrodes which enabled them to use anodic bonding in the packaging process of the glass substrate with the silicon microchannels. A flow rate of 87 ml/min at DC voltage of 40 V was obtained with ethyl alcohol.

Shooshtari (2004) used microfabrication techniques to build a grid-type EHD ion-injection pump. At the same time, he developed a numerical model to describe the performance of the pump. The pump was tested in a closed-loop test section and the experimental results showed good agreement with the numerical ones.

Darabi and Wang (2005) reported experimental results on a new design of the micropump that Darabi and his co-workers (2002) had developed previously at the University of Maryland, College Park. Their new design, developed at the University of

South Carolina, had saw-tooth shape emitters and planar collectors with 20 μm emitter-collector spacing and 40 μm stage spacing with a channel height of 50 μm. They reported a maximum pressure head of 550 Pa at an electric field of 9 V/μm with HFE 7100. They performed static pressure head tests in an open dish and measured the rise of the liquid column. They also reported a maximum mass flow rate of 3.9 g/min at 180 Pa pressure drop, which was performed in a closed loop system with the same working liquid. At the same time, Benetis (2005) performed experimental studies on different designs of the micropump, which also included Darabi and Wang's design. He obtained a maximum pressure head of 550 Pa and a flow rate of 2.7 ml/min at a DC voltage of 500 V. Benetis performed both static pressure head and flow rate experiments within a closed loop system.

Very recently, Chen and co-workers (2007) reported development of a planar ion-drag micropump on a flexible Parylene-C substrate. Their design is very similar to the design of the University of Maryland's research team: saw-tooth emitters, planar collector, 20 μm emitter-collector spacing, and 80 μm stage spacing. They patterned Au electrodes using a lift-off process and made channel walls of 80 μm height with SU-8. No discussion of the channel top-cover is ever mentioned. They obtained a flow velocity of about 190 mm/min at 20 V and a pumping pressure of 490 Pa at 30V with isopropanol. Their discussion implies that their experimental results were obtained with a similar pump created on oxidized silicon substrate and not from the flexible Parylene pumps. Of course, one of the disadvantages of a flexible pump is that it can easily get pinched or twisted, which may result into blockage of the flow cross-sectional area. This also stresses the electrodes and may result into cracking or peeling.

Table 2-1 compares test conditions and experimental results obtained by many researchers with different working liquids and various designs of the micro-scale ion-drag pumps. These pumps were mainly developed for ambient temperature applications.

Table 2-1 Summary of selected experimental studies on ion-drag micropumps

No.	Reference	Pump Dimension	Electrode Geometry	Electrode Gap (μm)	Stage Gap (μm)	Number of Stages
1	Richter et al. (1991)	Grids active area: 3 x 3 mm^2	E & C: microfabricated grids	70, 140	350	1
2	Wong et al. (1995)	≈ 9 x 9 mm^2	E & C: microfabricated grids	127, 178, 330	------	1
3	Ahn and Kim (1998)	Channel width: 3 mm Channel height: 100, 200 μm	E & C: planar strips	100	200	30
4	Darabi et al. (2002)	≈ 20 x 30 x 10 mm^3	E: planar saw-tooth, saw-tooth with bumps C: planar strips	50, 100	100, 200	95, 80, 50
5	Benetis et al. (2003)	≈ 25 x 35 x 1 mm^3 Channel height: 100, 220, 350, 450 μm	E: planar saw-tooth C: planar strips	20, 50	80, 100, 200	94, 73, 54
6	Yang et al. (2003)	Channel width:100μm Channel height:26 μm	E & C: indium-tin-oxide (ITO) planar	80	------	20
7	Shooshtari (2004)	≈ 25 x 30 x 10 mm^3	E & C: microfabricated grids	250	------	------
8	Darabi and Wang (2005)	≈ 20 x 30 x 10 mm^3	E: planar saw-tooth C: planar strips	20	40	200
9	Benetis (2005)	≈ 25 x 35 x 10 mm^3	E: planar saw-tooth C: planar strips	10, 20, 50	20, 40, 80, 100, 200	94, 73, 54
10	Chen et al. (2007)	5 x 7 x 0.1 mm^3 Channel height: 80μm	E: planar saw-tooth C: planar strips	20	80	75, 200

No.	Reference	Working Liquid	Applied Voltage (V)	Measured Current	Max Pressure Head	Volume Flow Rate
1	Richter et al. (1991)	Ethanol	0 - 700	------	2500 Pa at 700 V	14 ml/min with 420 Pa
2	Wong et al. (1995)	Proponal	0 - 100	≈ 1 mA	287 Pa at 120 V	------
3	Ahn and Kim (1998)	Ethyl alcohol	0 - 120	3 mA	225 Pa at 100 V	55 µL/min at 120 V
4	Darabi et al. (2002)	HFE 7100	0 - 700	------	700 Pa at 300 V	------
5	Benetis et al. (2003)	HFE 7100	0 - 500	≈ 100 µA	700 Pa at 450 V	7.92 ml/min at 450 V
6	Yang et al. (2003)	Ethanol	0 - 90	------	------	87 nl/min at 40 V
7	Shooshtari (2004)	HFE 7100	0 - 1500	≈ 17 µA	270 Pa	35 ml/min
8	Darabi and Wang (2005)	HFE 7100	0 – 400 (calculated)	------	550 Pa at 9 V/µm	3.9 g/min with 180 Pa
9	Benetis (2005)	HFE 7100	0 - 600	≈ 100 µA	550 Pa	2.7 ml/min at 500 V
10	Chen et al. (2007)	Isopropanol	0 - 100	------	490 Pa at 30V	Flow velocity: 190 mm/min at 20 V

2.1.3.2. Cryogenic Applications

To the best of author's knowledge, only a few studies have been reported on EHD pumping phenomena specifically with cryogenic liquids. Boyarintsev and co-workers (1992) reported experimental results from a meso-scale EHD pump made with thin wire-grid electrodes. The inner diameter of the pump was 22 mm, and it was tested using LN_2 as the working fluid. They examined the effect of the number of pumping stages (pairs of emitters and collectors) and electrode wire thickness on the pumping performance. They achieved the highest amount of pumping with both emitter and collector thickness of 0.05 mm diameter and the number of stages was seven. A pumping head of up to about 900 Pa was reported at 40 kV.

Rada (2004) developed a meso-scale EHD pump with a crown-shape emitter and a ring collector to work with LN2 as the working liquid as shown in Figure 2-3. He demonstrated some pressure generation at a DC voltage of 12 kV with this pump.

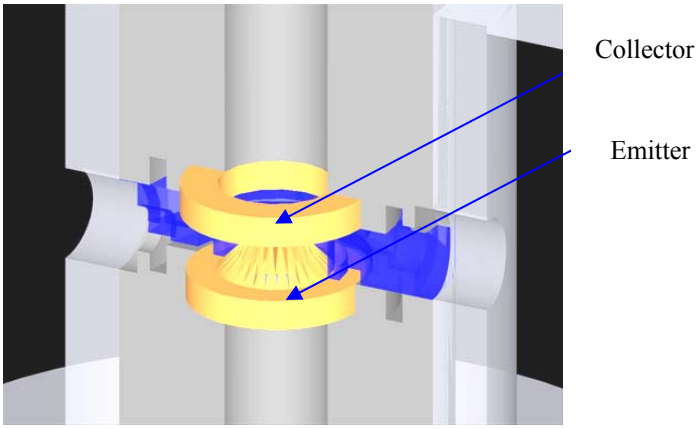

Figure 2-3 Drawing of a meso-scale ion-drag pump, adopted from Rada (2004).

Zhao et al. (2003) and Foroughi et al. (2005) extended the University of Maryland research on the micropump and demonstrated for the first time the successful fabrication

and testing of a micropump for the purpose of LN_2 pumping. Their micropump had saw-tooth emitter and planar collector pairs with 50 μm emitter-collector spacing and 200 μm stage spacing, and was capable of pumping liquid nitrogen at a flow rate of 2.3 g/min at a DC voltage of 1000 V.

Darabi and Wang (2005) in their recent publication also presented some experimental results with LN_2. They reported a maximum pressure head of 205 Pa at an electric field of 11 V/μm. They performed static pressure head tests inside a Dewar flask with a transparent cover and measured the rise of the liquid column. One problem with their measurement method was that their experiments were not run in a closed well-vacuumed system, and therefore the effect of oxygen solubility in LN_2 was not taken into account. Oxygen's boiling point is 90 K, much less than that of LN_2, which allows it to condensate easily into the LN_2 flask where the tests are performed. Another problem was that the experiments were run at atmospheric pressure, at which a small amount of heat can cause LN_2 boiling and bubble formation inside the pump, which could also contribute to less accuracy of measurement.

Other researchers have observed liquid nitrogen motion while measuring conduction current and mobility in LN_2 under high electric field (Butcher 2005, Takashima et al. 1988, Doake and Gribbon 1971, Byatt and Secker 1968).

2.2. EHD Governing Equations

The EHD pumping phenomenon is a direct result of the interaction between electric and fluid flow fields. When an electric potential difference is applied to a dielectric fluid, an electric field is formed within the fluid. If the field sets the liquid into motion, the distributions of both charge density and electric field change. This

complicated and nonlinear behavior of the electric force and liquid motion makes EHD difficult to quantify.

In order to better understand the phenomenon, the first step is to develop a theoretical model in which the liquid behavior under the influence of an electric field can be analyzed. For this study, we start with two basic series of governing equations which describe the electric field and the flow field. Later, the electric body force is introduced. And finally, these equations are nondimensionalized, and the importance of dimensionless parameters is discussed.

2.2.1. Electric Field Equations

Melcher (1981) in his book has explained extensively that the electromagnetic field in a system can be considered as a quasi-static electric field system. Since dielectric fluids exhibit a very low conductivity, the conduction current becomes so small that the magnetic induction will be negligible. Therefore in a simplified system, such as a parallel plate electrodes system, Maxwell's equations (a set of four basic equations) are reduced to only electrostatic laws. Gauss's law relates the free charge density, ρ_e, to the electric field intensity $\mathbf{E}$

$$\nabla . \mathbf{E} = \frac{\rho_e}{\varepsilon} \tag{2-2}$$

where ε is the permittivity of dielectric liquid.

Since the magnetic field is negligible, Faraday's law reduces to

$$\nabla \times \mathbf{E} = 0 \tag{2-3}$$

and therefore, the electric field can be expressed as the gradient of a potential field

$$\mathbf{E} = -\nabla \Phi$$

(2-4)

And finally, the charge conservation law states

$$\nabla \cdot \mathbf{J} + \frac{\partial \rho_e}{\partial t} = 0$$

(2-5)

where J is the electric current density. Three terms in Equation (2-6) represent different mechanisms for the current flow: convection, migration and conduction,

$$\mathbf{J} = \sigma_e \mathbf{E} + \mu_e \rho_e \mathbf{E} + \rho_e \mathbf{u}$$

(2-6)

where $\mu_e, \rho_e,$ and σ_e are the mobility, unipolar charge density, and bipolar conductivity of the bulk fluid, respectively (Melcher and Taylor 1969).

The first term in Equation (2-6) represents the conduction term, which refers to the bipolar conduction and is given by the Ohmic constitutive law. When an electric potential difference is applied to a dielectric fluid (with resistivity usually above 10^7 Ω-m and permittivity below 20), the electrical conduction process starts as a result of dissociation of either impurity molecules inside the liquid or the liquid molecules themselves. Dissociation always creates an equal number of positive and negative ions which under the influence of electric field does not affect the net force on the liquid but only appears as additional input power requirements for the pump (Crowley et al. 1990). In most areas of EHD for dielectric liquids of high enough resistivity, Ohm's law and electroneutrality often fail to be valid. An excellent review on the electrohydrodynamics of liquids in the ohmic regime and subjected to Coulomb forces has been written by Melcher and Taylor (1969), and more recently by Ohadi et al. (2001).

The second and last terms, the so-called migration and convection currents, represent the motion of the net space charges, which are always free to move inside the fluid. In a stationary fluid, electric force applied to the charges tends to pull them through the fluid at the velocity $\mu_e \mathbf{E}$ relative to the fluid (Crowley et al. 1990). If the fluid is set into motion, the distribution of charge density changes (via the charge conservation law), which in turn changes the velocity field (via the Navier-Stokes equation) (Castellanos 1991). Therefore, the convection term $\rho_e \mathbf{u}$ accounts for the convection of charge density by the velocity field.

2.2.2. Fluid Dynamic Equations

The equations of motion for an incompressible Newtonian fluid are continuity

$$\nabla \cdot \mathbf{u} = 0 \tag{2-7}$$

and Navier-Stokes equations with an electric body force $\mathbf{f_e}$

$$\rho\left[\frac{\partial \mathbf{u}}{\partial t} + (\mathbf{u} \cdot \nabla)\mathbf{u}\right] = -\nabla p + \eta \nabla^2 \mathbf{u} + \rho \mathbf{g} + \mathbf{f_e} \tag{2-8}$$

Electric body force, as will be explained further in detail, represents the interaction between electric and flow fields. Equation (2-9) represents the energy equation for an incompressible fluid

$$\frac{\partial T}{\partial t} + \mathbf{u} \cdot \nabla T = \nabla \cdot (\alpha \nabla T) + \frac{\nu}{c_p}\phi + \frac{S_J}{\rho c_p} \tag{2-9}$$

where S_J is the Joule heating source term. Joule heating or ohmic heating refers to the increase in temperature of the bulk liquid as a result of resistance to an electrical current

flowing through it. For a fluid with unipolar charge migration and ohmic conduction, the Joule heating term is defined by Equation (2-10) (Castellanos 1998).

$$S_J = \sigma_e E^2 + \mu_e \rho_e E^2 \tag{2-10}$$

In ion-drag micropumps, the power consumption is very low; as a result, the amount of heat generation in the bulk liquid is very low, which results in no apparent temperature variation as observed during the experiments. Therefore, the energy equation and the joule heating terms are often negligible except in the numerical modeling case, in which an additional variable T is added to the system of equations.

2.2.3. EHD Body Force

As explained earlier, the influence of the electric field on the fluid field is expressed by the electric body force, $\mathbf{f_e}$. The body force cannot be determined using the molecular thermodynamic principles due to the complexity of the problem. Instead, an energy balance method is used to derive the equation by Stratton (1941) and Panofsky and Phillips (1962). A comprehensive review of the derivation of the body force is also presented by Darabi (1999).

Equation (2-11) expresses the electric body force acting on the fluid:

$$\mathbf{f_e} = \rho_e \mathbf{E} - \frac{1}{2} E^2 \nabla \varepsilon - \frac{1}{2} \nabla \left[\rho \, E^2 \left(\frac{\partial \varepsilon}{\partial \rho} \right)_T \right]$$

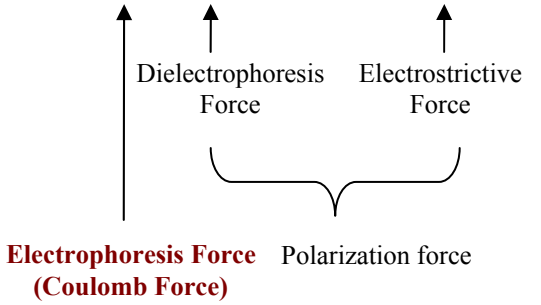

(2-11)

The three terms on the right hand side of the equation represent different types of electrical forces acting on the fluid, which are known as the electrophoretic, dielectrophoretic, and electrostrictive forces, respectively.

Electrophoretic force represents the Coulomb force and is the force that acts upon free charges within the fluid. As the Coulomb's law states, the magnitude of the electrostatic force between two charged particles is directly proportional to the magnitudes of each charge and inversely proportional to the square of the distance between the charges. It also indicates that when a DC potential difference is applied to free charges within a fluid (dipoles are not free charges), charged particles move along the electric field according to their charge sign and generate fluid motion. In an incompressible single phase flow, the Coulomb force is expected to be responsible for most of the fluid motion. In the first term, $\mathbf{f_e}$ is the force density and ρ_e is the charge density which represents the sum of all charge densities including positive and negative. It therefore defines only one direction for fluid motion under the DC electric field and oscillation under AC fields. The Coulomb force requires the existence of free charges within the working fluid. There are different methods by which free charges can be

generated in a dielectric liquid. In ion-drag pumps, charge injection is the dominant process of free charge generation. Charge injection is initiated at or close to the electrode/fluid interface if a sufficient voltage potential is applied across the electrode pairs as shown in Figure 2-1. For a successful pumping, the abundance of one ion polarity is preferred since the generation of an equal number of ions of both polarities will lead to no net pumping.

The second and third terms, known as polarization forces, are more important in two-phase and/or compressible fluids. The dielectrophoretic force, given by $\frac{1}{2}E^2\nabla\varepsilon$, is implemented as the interaction of a non-uniform electric field with the dipole moments induced in the neutral molecules of the fluid. In a uniform electric field, the forces acting on two charges of a dipole molecule cancel out, however in a non-uniform field; the polarization force on the side located at a more intense electric field exceeds the force on the other side and moves the dipole toward the direction of increasing electric field strength. As it is expanded and shown by Equation (2-12), the dielectrophoretic force is generated as a result of permittivity gradient at the liquid-vapor interface in the two-phase flow or due to a temperature gradient in the non-isothermal fluids.

$$\frac{1}{2}E^2\nabla\varepsilon = \frac{1}{2}E^2\left(\left(\frac{\partial\varepsilon}{\partial\rho}\right)_T\nabla\rho + \left(\frac{\partial\varepsilon}{\partial T}\right)_T\nabla T\right) \quad \textbf{(2-12)}$$

The last term in Equation (2-11) is a gradient term called electrostrictive force which similar to dielectrophoretic forces, acts upon the dipoles in dielectric liquid. A single-phase dielectric liquid becomes polarized when the permittivity (or dielectric constant) changes with position or density. In cases where the liquid becomes elastically deformed by electrostrictive field, the fluid flow is not generally affected, and only the

pressure changes. In an isothermal single-phase flow, the effect of polarization forces can generally be neglected as $\nabla\varepsilon$ vanishes.

The main goal of this study is to characterize the EHD ion-drag pumping mechanism as applied to micro pumping of liquid nitrogen. Ion-drag micropumps are designed to employ a single-phase incompressible liquid with a large dielectric constant as the working liquid. Therefore, the major driving force in an ion-drag EHD micropump is the Coulomb force, which requires the existence of free charges within the working liquid.

2.2.4. Dimensionless Form of the Governing Equations

To make the EHD governing equations independent of the measured units, the EHD governing equations are rewritten in terms of dimensionless parameters. Dimensionless parameters are chosen according to the recommendations of the IEEE-DEIS EHD Technical Committee (2003). The system of equations, which was developed based on a unipolar charge injection assumption is mainly adapted from Shooshtari's work (2004).

To nondimensionalize the governing equations, the following terms are used

$$\nabla^* = L\nabla \ , \quad \rho_e{}^* = \frac{\rho_e}{\rho_{e0}}, \quad \mathbf{E}^* = \frac{\mathbf{E}}{E_0}, \quad \mathbf{u}^* = \frac{\mathbf{u}}{U_0} \tag{2-13}$$

The dimensionless parameters used in this study are tabulated in Table 2-2.

Table 2-2 Dimensionless parameters based on conservation equations (Tabulated in Table 2, IEEE-DEIS EHD Technical Committee 2003).

Symbol	Expression	Name
Re	LU_0/ν	Reynolds number
E_{hd}	$\rho_e E_0 L^3/\rho\nu^2$	EHD number (conductive electric Rayleigh number)
Md	$\varepsilon_0 E_0^2 L^2/\rho\nu^2$	Masuda number (dielectric electric Rayleigh number)
Sc_i	ν/D	Ion Schmidt number
F_E	$\mu_e E_0 L/D$	Ion drift number
Re_e*	$\varepsilon U_0/\sigma_e L$	Electric Reynolds number

* Re_e is calculated in terms of dimensionless parameters based on physics (Table 1, IEEE-DEIS EHD Technical Committee 2003).

Equation (2-4) can now be expressed as

$$\nabla^* \cdot (\varepsilon_r \mathbf{E}^*) = \frac{\mathrm{E_{hd}}}{\mathrm{Md}} \rho_e^* \tag{2-14}$$

The charge conservation law, shown as Equation (2-5), changes to

$$\frac{\partial \rho_e^*}{\partial t^*} + \frac{\mathrm{F_E}}{\mathrm{E_{hd}} \cdot \mathrm{Re} \cdot \mathrm{Sc_i}} \nabla^* \cdot \mathbf{J}^* = 0 \tag{2-15}$$

where the dimensionless current density is defined as

$$\mathbf{J}^* = \frac{L^3}{\rho\nu^2\mu_e}\mathbf{J} \tag{2-16}$$

Therefore, equation (2-6) can be nondimensionalized as

$$\mathbf{J}^* = \frac{\mathrm{ReSc_i Md}}{\mathrm{Re_e F_E}}\mathbf{E}^* + \mathrm{E_{hd}}\,\rho_e^*\mathbf{E}^* + \frac{\mathrm{ReSc_i E_{hd}}}{\mathrm{F_E}}\rho_e^*\mathbf{u}^* \tag{2-17}$$

The momentum equation, equation (2-8), can be rewritten as

$$\left[\frac{\partial \mathbf{u}^*}{\partial t^*} + (\mathbf{u}^* . \nabla^*)\mathbf{u}^*\right] = -\nabla^* p^* + \frac{1}{\mathrm{Re}}\nabla^{*2} \cdot \mathbf{u}^* + \mathbf{g}^* + \mathbf{f_e}^*$$

(2-18)

where the dimensionless electrohydrodynamic body force is defined as

$$\mathbf{f_e}^* = \frac{L\mathbf{f_e}}{\rho U_0{}^2}$$

(2-19)

And finally, the EHD body force for a non-compressible single-phase flow can be expressed as in equation (2-20)

$$\mathbf{f_e}^* = \frac{\mathrm{E_{hd}}}{\mathrm{Re}^2}\rho_e^* \mathbf{E}^*$$

(2-20)

2.3. Summary

This chapter reviewed the fundamental operation mechanism of the EHD pumping followed by a selective literature survey of EHD ion-drag/ion-injection pumps in two main areas of application: ambient temperature and cryogenic. Next, the physics of the EHD pumping phenomena, relevant governing equations, and a review of various controlling parameters on liquid nitrogen EHD pumping were presented.

CHAPTER 3: ELECTRIC CHARGE GENERATION PHENOMENA IN NONPOLAR CRYOGENIC LIQUIDS

As mentioned earlier (Chapter 2), interaction between the electric charge carriers and electric field is crucial for understanding the EHD phenomenon, especially for the ion-drag pumping mechanism where the Coulomb force has the dominant effect.

In this section, fundamentals of generation and transport of electric charge carriers in nonpolar liquids under the influence of intense electric field is studied. In particular, more attention is paid to the characteristics and behavior of liquid nitrogen, as it is the working fluid in this research.

3.1. Polar and Nonpolar Liquids

Polar liquids such as aromatic hydrocarbons (e.g. chlorobenzene), acetone, water, and ethanol have permanent dipoles in the absence of external electric field. Permanent dipoles are formed when there is a large difference in electronegativity between two atoms bonded together in a covalent bond. This causes the shared pair of electrons to be shared unequally and pulled towards the more electronegative atom. As a result of this, polar liquid purification is extremely difficult as the liquid tends to make strong bonds with the impurity molecules. Polar liquids with a high degree of purity exhibit very low conductivity and a large dielectric constant, usually more than 30, and therefore are very attractive as dielectric media (Gallagher 1975).

Nonpolar liquids, in contrast, are comprised of atoms or molecules with no permanent electric dipole moment. In an ultra-pure nonpolar liquid, dipoles are only

formed under the influence of an external agent (e.g. electric field in EHD application). These dipoles are not permanent and will relax once the electric field is removed. Most of the insulating liquids such as liquefied rare gases (e.g. liquid helium), simple molecular liquids (e.g. liquid nitrogen), hydrocarbons and their derivatives are non-polar. Highly-pure nonpolar liquids are used as liquid insulators in power transformers, transmission cables and in other industrial apparatus and processes (Schmidt 1999).

3.2. Electric Charge Generation in Cryogenic Liquids

The presence of electric charge carriers in a liquid medium is necessary for the EHD pumping phenomenon to take place. In nonpolar dielectric liquids, such as LN_2, with high degree of purity, molecular dissociation is very weak due to the strong covalent bond, and the space charges are mainly created at the metal electrode/ liquid interface under the influence of high electric field. Electric charge generation at the liquid/metal interface, also known as ion injection, is often governed by two main mechanisms: *field emission* and *field ionization* (Arii and Schmidt 1984). Both processes occur at the interface when the electric field is strong enough to overcome the energy barrier at the interface. The injected ions, which are of the same polarity as the electrodes, can create *momentum* and set the bulk liquid in motion. This phenomenon is often referred to as ion-drag (or ion-injection) pumping.

Field ionization occurs near a positively charged electrode where shell electrons from the liquid molecules or atoms tunnel into the metal and make the liquid molecules positively ionized. According to Arii and Schmidt (1984), the energy barrier for an atom being ionized by a field ionization process is

$$\Delta E_{fi} = | I_l + V_0 - \varphi |$$

(3-1)

where I_l is the ionization energy of the liquid, φ is the work function of the electrode metal, and V_0 is the conduction band energy in the liquid.

Field emission occurs near a negatively charged emitter where the electrons from the metal surface tunnel into the liquid and make the liquid molecules negatively ionized. This process is controlled by the difference between the energy of the liquid conduction band, V_0, and the work function of the electrode metal, φ, as stated by Equation (3-2) (Arii and Schmidt 1984).

$$\Delta E_{fe} = | \varphi - V_0 |$$

(3-2)

As stated by Sakai and co-workers (1993), the injected electron which has equal or higher energy than the conduction band lower limit, V_0 (see Figure 3-1), will become, most probably in case of LN_2, a localized electron in the bulk liquid and surrounded by a "bubble" of nitrogen molecules.

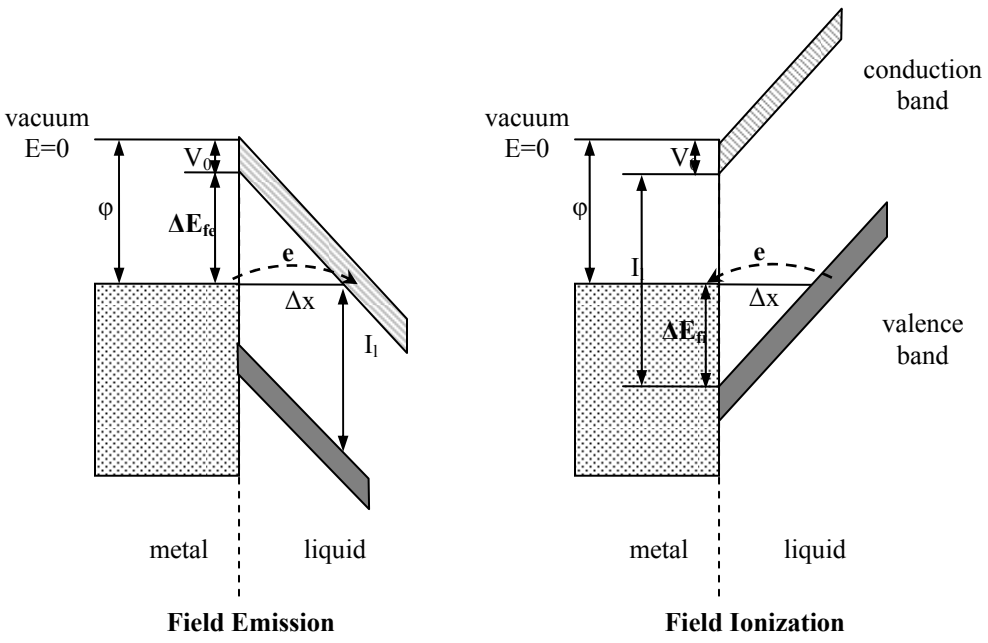

Figure 3-1 Energetic condition at the metal/liquid interface (Redrawn from the data of Arii and Schmidt (1984)).

The energy barriers, ΔE_{fi} and ΔE_{fe}, are usually not equal for a particular metal electrode/liquid interface. The field emission becomes the dominant process when ΔE_{fi} exceeds ΔE_{fe}, which indicates that under identical experimental conditions less voltage (with negative polarity) is required to overcome the energy barrier of the field emission and to initiate the current. Conversely, a similar argument is valid for the positive polarity and the field ionization onset voltage.

Halpern and Gomer (1969a and 1969b) did an extensive study on the field emission and field ionization phenomena while investigating I-V characteristics of cryogenic liquids at the point-plane tungsten electrodes. According to what they found at lower currents, the I-V characteristics are controlled by the mechanism of charge carrier generation at the electrode tip. However, as the rate of charge generation increases at higher voltages, the space charge limited current (SCL) sets in. According to what they

found for liquid Ar (LAr), the field ionization onset voltage is more than two times higher than that of the field emission. Their data were in agreement with the experimental and analytical data of Arii and Schmidt (1984).

Arii and Schmidt (1984) initially used the electronic energy conditions at the LAr/tungsten interface to calculate the energy barriers at the interface ΔE_{fe} and ΔE_{fi}. They demonstrated $\Delta E_{fe} << \Delta E_{fi}$ at the LAr/tungsten interface, which was later confirmed by their experimental data. They also calculated the energy barriers at the LXe/ tungsten interface and found that $\Delta E_{fe} \approx \Delta E_{fi}$. Their experimental results also supported that assessment, since with both negative and positive voltage polarities, similar conduction currents were obtained at the LXe/ tungsten interface.

3.2.1. Electric Charge Generation in Liquids Nitrogen (LN_2)

For the current research, it is necessary to find out which polarity works best with the micropumps and the working liquid (LN_2) considered in this study. Therefore, the energy barriers at different metal/liquid interfaces for positive and negative polarities (ΔE_{fi} and ΔE_{fe}) are first calculated following the footsteps of Arii and Schmidt (1984). For that, we start with calculating the *ionization energy of the liquid*, I_l, which is the energy required for the creation of an electron/hole pair inside the liquid. For liquids, similar to solids, the electronic energy band model can be used for estimating I_l (Schmidt 1991).

Atoms or molecules in the gas phase are distinguished by their ionization energy, I_g, which is defined as the energy required to remove the outermost valence electron completely from its atom. During condensation, a shift of the ionization energy takes place due to the polarization energy of the positive charge carrier and because the

electron is promoted into an electronic conduction band. Figure 3-2 shows a schematic of the change of electronic energy levels upon condensation.

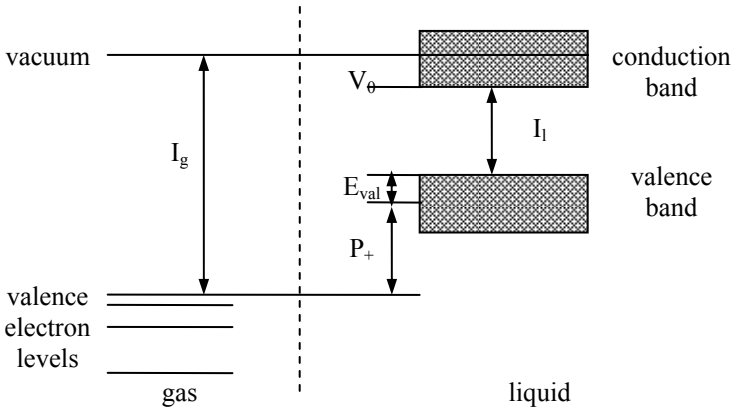

Figure 3-2 Electronic energy levels in gas and liquid molecules (Redrawn from the data of Schmidt (1991)).

In nonpolar dielectric liquids, valence and conduction bands are separated by energy of ≥ 5eV (Schmidt 1991). The energy of vacuum is set equal to zero. As shown by Equation (3-3), I_l is related to the ionization potential of the gas atoms or molecules, I_g, as

$$I_l = I_g - P_+ - V_0 - E_{val} \tag{3-3}$$

where V_0 denotes the e*nergy of the conduction band* and is defined as the energy required for the transfer of an electron from liquid to vacuum.

For most nonpolar liquids, V_0 varies between +0.5 eV and -0.7 eV and for liquid nitrogen has been estimated to be +0.35 eV (Lewis 1994). E_{val} describes the *broadening of the valence levels* caused by condensation and has a negative quantity on the order of 0.1 eV for liquid insulators (Schmidt 1997). P_+ is the *polarization energy of the cation* and is always negative. It is worth noting that the accurate values of P_+ and V_0 cannot yet

be determined but can be estimated with some degree of confidence from the simplified models.

According to Born's model (Born 1920), polarization energy of a positive ion (cation) of a radius R in a nonpolar dielectric liquid of ε_r can be expressed as

$$P_+ = -\frac{e_0^2}{8\pi\varepsilon_0 R}\left(1-\frac{1}{\varepsilon_r}\right) \quad \textbf{(3-4)}$$

where e_0 is the electronic charge and ε_r is the relative permittivity. R is the distance from the center of the ion beyond which the medium if fully polarized. The value of R is usually taken as one or two molecular radii (Freeman 1987). Based on Born's model, the estimated value of P_+ is about -2.9 eV (Table 3-1). Energies of the electronic levels of nitrogen in the gas and liquid phases are tabulated in Table 3-1.

Table 3-1 Energies of the electronic levels in the gas and liquid nitrogen

I_g (eV)	P_+ * (eV)	V_0 (eV)	E_{val} (eV)	**I_l (eV)**
-14.5	-2.9	+0.35	-0.1	-11.85

* P_+ is calculated from Equation (3-4) based on the following parameters:

$e_0 = 1.60217646 \times 10^{-19}$ C
$\varepsilon_0 = 8.85419 \times 10^{-12}$ C^2/Jm
$\varepsilon_r = 1.43$
R = 0.746 Å (Moeller 1982)

Energy barriers of the field ionization and the field emission are finally calculated using the I_l value from Table 3-1 and Equations (3-1) and (3-2) with two different interfaces: gold and platinum electrodes with LN_2 as the working liquid. The energy barriers are compared in Table 3-2. At both metal/liquid interfaces, the field emission and field ionization energy barriers have close values, which predicts a similar trend of

conduction currents with both voltage polarities. In other words, the probability of creating negative and positive ions is expected to be similar with both voltage polarities.

Table 3-2 Field emission and field ionization energy barriers at the metal/LN_2 interfaces

φ (eV)		**ΔE_{fe} (eV)**	**ΔE_{fi} (eV)**
gold	-5.1	**5.45**	**6.4**
platinum	-5.65	**6**	**5.85**

Our experimental results in Chapter 6 strongly agree with this claim, as similar pumping heads and conduction currents were obtained with both voltage polarities at the Au/LN_2 interface.

Finally, it is worth noting that assuming pure field emission or field ionization as the main mechanism of charge generation is an ideal model. In reality, other processes, such as *collisional ionization*, may also take place in the high field region around the tip, which can cause micro discharges from which unipolar charge carriers can be injected into the bulk (McClintock 1973).

3.3. Charge Carriers Mobility in Liquid Dielectrics

One of the important transport properties of electrons and ions is their drift mobility, μ_e, which is defined as the ratio of the observed drift velocity (u) to the applied electric field (E) as shown in Equation (3-5).

$$\mu_e = \frac{u}{E} \tag{3-5}$$

The charge carrier's mobility, in addition to other factors such as electrode geometry, liquid density and polarity of the applied voltage play a key role in the breakdown strength of a dielectric liquid (Gee et. al 1985). Also according to Crowley et al. (1990), mobility has an important effect on the performance of the EHD pumps. Based on his definition of efficiency, low mobility promotes high efficiency, or in other words, the efficiency is 100 percent when the mobility vanishes, so that the liquid is forced to move at the same speed as the charges. Mobility can also help distinguish the type of the electric charge carriers present in a dielectric liquid. An example is the higher mobility of electrons compared to anions.

Schmidt (1997) and Freeman (1987) have collected and reported electron and ion mobility data for more than 100 liquids in their books and research papers; these data will be referred to as the main source of information here. Different methods have been used for measuring the charge mobility and detecting the type of electric charges in dielectric liquids. In most cases, an external means of charge generation is used, such as injection or ionization. Ionization often takes place using single or multi-phonon absorption or high-energy radiation, whereas injection occurs at the metal electrode/liquid interface. The type and the mobility of the ions/electrons generated can be monitored by the following methods (Holroyd and Schmidt 1989):

1. *Measurement of DC conductivity*: (the time of flight method): The fact that electrons move faster than molecular ions shows that the current at short times is due to electron motion.
2. *Measurement of microwave conductivity*: This measures the absorption of electromagnetic radiation by free charges.

3. *Measurement of optical absorption*: This method is particularly useful in liquids with low mobility, such as in some alkane liquids.

In these experiments, the liquid is initially at rest. But under some experimental conditions where many ions are generated at the electrode tips or blades, the ions may transfer momentum to the liquid molecules and cause some liquid motion. In this case, the measured mobility may be several times higher than the actual ion mobility, and the EHD effect on the mobility measurement has to be taken into account (Tobazeon 1984). As stated by Gray and Lewis (1969), the influence of EHD on ionic mobility mainly depends on the injection current strengths, i.e. in the measurement experiments, such as in pulse radiation, where the ionic concentration is so small that the total energy dissipated by the moving ions is not sufficient to induce any liquid motion (Schmidt 1997).

3.3.1. Models of Electron Transport in Dielectric Liquids

As mentioned earlier, electric charge carriers have different mobility values depending on their size and electric charges. According to Jortner and Gaathon (1977), the electronic states of excess electrons in dielectric liquids can be classified into three regions in accordance with their mobility (Schmidt 1997 and 1999):

1. $\mu_e > 10\ cm^2V^{-1}s^{-1}$
2. $\mu_e < 0.1\ cm^2V^{-1}s^{-1}$
3. $0.1 < \mu_e < 10\ cm^2V^{-1}s^{-1}$

In region (1), the electron moves in the *delocalized* state (An electron can only be considered completely free in the vacuum.). As shown by Gee et al (1985), the electrons stay nearly free in LAr and liquid methane.

In region (2), the excess electron can be viewed as being *localized* in preexisting traps (e.g. holes) or in potential fluctuations, and the state of the electron is described by a localized wave function. In this state, the electron's mobility is ionic, and electrons usually exist in the form of anions. Examples are the electron bubbles in LHe, LNe, and LN_2 (Schmidt 1997).

In region (3), the electron may be considered as being *partially delocalized*, where it spends comparable amounts of time in the localized and delocalized states. Examples in this region are liquid iso-octane and liquid cyclo-pentane (Schmidt 1997).

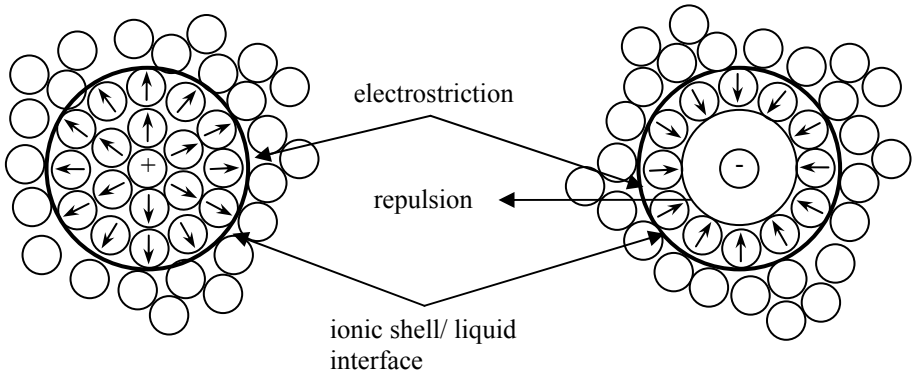

Figure 3-3 Orientation of neutral atoms/molecules around a positive and a negative ion; the dipole moment depicts the conventional direction from '-' toward '+'. (Redrawn from the data of Schmidt (1997))

Experiments have shown that most often the negative ions exhibit a higher mobility than positive ones. According to Schmidt (1997), the main difference lies in the interaction of positive and negative ions with the molecules in the bulk due to possible electrostriction and repulsion effects around the positive and negative ions. In the case of positive ions, a few layers of neutral molecules are firmly bound to the core of the ion and form a temporary ionic cluster with a greater radius than that of the hard core. The ionic cluster eventually has a higher density and viscosity than the bulk. In the case of negative ions, however, the clustering is reduced as the electrostriction effect is partially

counterbalanced by the repulsive potential between the excess electron of the ion and the electrons of the surrounding molecules (Figure 3-3). As a result, the mobility of the positive ionic cluster becomes less than that of the negative one of similar size.

3.3.2. Positive and Negative Ion Mobilities in LN_2

Only a limited number of studies have been conducted on the mobility measurement of LN_2; many of those were parts of studies done on the breakdown or the electric field effect on ion generation in LN_2. The reported mobility data in most cases had certain variations. This could be a direct result of different impurity levels existing in the experimental test setups, which in the end altered the mobility data significantly. Gee et al. (1985) and Ramanan and Freeman (1987) have written clear reviews on the reported work in this area. Table 3-3 summarizes some of the data that are less scattered and are mainly adapted for this research.

Table 3-3 Liquid nitrogen mobility measurement data

Reference	**Temperature (K)**	**Anion Mobility, μ_- ($cm^2V^{-1}s^{-1}$)**	**Cation Mobility, μ_+ ($cm^2V^{-1}s^{-1}$)**	**Electric Field Strength (MV/m)**
Ramanan and Freeman (1987)	77.1	$2.5x10^{-3}$	$1.4x10^{-3}$	0.3 - 6
	98.0	$4.7x10^{-3}$	$3.0x10^{-3}$	0.3 - 6
Gee et al. (1985)	77.1	$2.5\ x10^{-3}$	$1.3x10^{-3}$	0.3 - 6
	98.0	$4.2x10^{-3}$	$2.7x10^{-3}$	0.3 - 6
Halpern and Gomer (1969a and 1969b)	77	$8\pm4\ x10^{-3}$	10^{-2}	≈ 0.1

According to the data from Ramanan and Freeman (1987) and Gee et al. (1985), the cation and anion mobilities in liquid nitrogen are independent of the electric field over the wide range of $0.3 < E\ (MV/m) < 6$.

Liquid nitrogen mobilities remain nearly constant over the temperature range of $77 < T\ (K) < 85$ where our interest lies, and far from the critical temperature. As the temperature increases toward the critical point, the viscosity decreases and the cation mobility, μ_+, increases, but at the same time, the product of the cation mobility and viscosity remains constant up to $T_c - 10$ K. The constant $\eta\mu_+$ substantiates Stokes' law (or Walden's rule), which can be used to estimate the cation radius:

$$r_{+/-}(m) = \frac{e_0}{6\pi\eta\mu_{+/-}} = \frac{8.49\times10^{-21}}{\eta\mu_{+/-}} \qquad \textbf{(3-6)}$$

which gives $r_+ = 3.5$ Å for cation in nitrogen at $T \leq 116$ K for $\eta\mu_+ = 2.42\times10^{-11}\, kg.m/V.s^2 = 2.42\times10^{-6}\, P.cm^2/V.s$.

The LN_2 anion mobility was found to be 1.7±0.1 times larger than that of the cation (Gee et al. 1985). The low mobility of the electrons confirms that the injected electrons in LN_2 exist in the form of anions. The product of the anion mobility and viscosity, $\eta\mu_-$, is approximately constant over the temperature range similar to that of the cation. The rapid increase in $\eta\mu_-$ at $T \geq 120$ K indicates that the anion is no longer stable at those conditions. Based on this, Gee et al. (1985) argued that the electron in LN_2 is not localized in a bubble (contrary to Sakai et al. 1993), but rather attaches to nitrogen molecules to form a temporary anion (Equation (3-7)).

$$e^- + m\mathrm{N}_2 \longleftrightarrow \left[\mathrm{N}_2\right]_m^- \qquad \textbf{(3-7)}$$

The anion radius, r_- , is calculated using Equation (3-6) to be approximately 2.2 Å.

3.4. Charge Relaxation Time and Electric Reynolds Number

According to Panofsky and Phillips (1962), in a stationary homogeneous medium, the continuity equation (2-5) can be combined with the conductivity equation $\mathbf{J} = \sigma_e \mathbf{E}$ and the source equation (2-2) to find a differential equation for ρ_e :

$$\frac{\partial \rho_e}{\partial t} + \frac{\sigma_e \rho_e}{\varepsilon} = 0 \tag{3-8}$$

Equation (3-8) is an ordinary differential equation, and its solution can be found by integrating with respect to time:

$$\rho_e = \rho_{e0}\, e^{-t/\tau} \tag{3-9}$$

where the characteristic time, τ_e, is

$$\tau_e = \frac{\varepsilon}{\sigma_e} \tag{3-10}$$

The characteristic time, τ_e, is usually known as the charge relaxation time of the medium. It is the time it takes for the stationary condition to take place after the initiation (or injection) of an electric charge flow. Charge relaxation time has the typical values illustrated in Table 3-4 (Haus and Melcher 1998).

Table 3-4 Charge relaxation times of typical materials

Substance	**σ (S/m)**	**ε/ε$_0$**	**τ$_e$ (s)**
Copper	5.8×10^{7}	1	1.5×10^{-19}
Water, distilled	2×10^{-4}	81	3.6×10^{-6}
Corn oil	5×10^{-11}	3.1	0.55
Mica	10^{-11} - 10^{-15}	5.8	5.1 - 5.1×10^{4}

As shown in Table 3-4, the relaxation time in conductive media is much less than in insulators because it takes less time for the charges to dissipate in a conductive media. It should also be noted that the above discussion only applies to homogenous media. If the medium is not homogenous, the spatial dependence of the conductivity and the dielectric constant must be taken into account in the integration of Equation (3-8).

3.4.1. Electric Reynolds Number

Electric Reynolds number, Re, is a well-established number which reflects the efficiency of the energy conversion process within an EHD pump. It is defined as the ratio of two characteristic times: the charge relaxation time of the fluid, τ_e, and the mechanical transport time, τ_m:

$$\mathrm{Re}_e = \frac{L/U}{\varepsilon/\sigma_e} = \frac{\tau_m}{\tau_e} \qquad \textbf{(3-11)}$$

In EHD pumps with dielectric working liquids, the pumping phenomenon takes place when the charge relaxation time is much shorter than the mechanical transport time or, according to Crowley et al. (1990), when the fluid passes from one electrode to the

other before the charge has time to flow backward. They showed that for high efficiency, the Reynolds number should be low. That requires a longer charge relaxation time, τ_e, or a high-speed flow:

$$U > \sigma_e L / \varepsilon \tag{3-12}$$

That also indicates that during actual pumping phenomenon within a dielectric liquid, the conduction current, $\sigma_e \mathbf{E}$, is negligible compared to the convection current, $\rho_e \mathbf{u}$ (see 2.2.1).

Because of its very small conductivity, liquid nitrogen has a pretty high charge relaxation time (ε/σ_e) compared to more conductive liquids such as HFE-7100. That means that the generated ions inside LN_2 tend to retain their charge for a longer time and thus, result in a higher efficiency of the ion-injection pump.

3.5. Current – Voltage Characteristic Curve

In nonpolar dielectric liquids, the electric current displays a dependence on the electric potential difference. Generally, four regions can be distinguished in the trend shown in Figure 3-4 (Schmidt 1997).

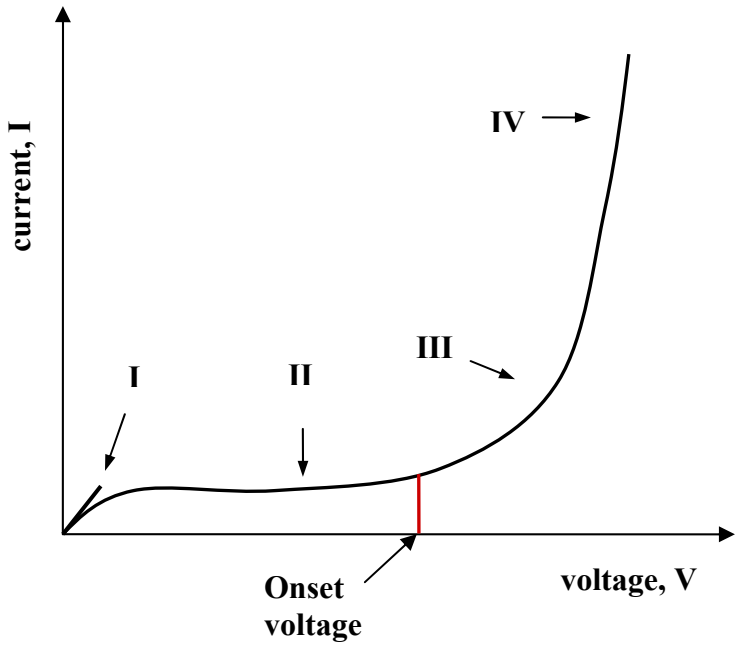

Figure 3-4 I-V Characteristic of a nonpolar liquid (Schmidt 1997).

In Region I, where the electric field is at its lowest, the conduction mechanism is Ohmic. The slope in this region represents the conductivity of the liquid (3-13). In insulating liquids, this is associated with the dissociation of the impurity molecules existing in the working fluid.

$$V = R\,I \tag{3-13}$$

Region II is established as we move to higher voltages. In this regime, the current remains nearly constant with the voltage as it reaches a saturation state or the so-called space charge limited current (SCLC). The space charge limit sets in at relatively low electric fields when the ion generation rate is faster than the rate at which ions reach the opposite-side electrodes. In this situation, each additional unipolar charge weakens the electric field. When the electric field becomes too low, charges can no longer be removed from the electrodes, as the charges already present in the liquid repel them.

That is why it is not always possible to inject a large amount of ions into a medium (Crowley et al. 1990).

At higher voltages, a sharp increase of current with voltage begins (Region III). This is due to either charge injection at the electrodes or charge multiplication in the bulk. In simple molecular liquids, the dissociation of the bulk liquid molecules is weak, and the charge carriers are mainly injected at the electrode/liquid interface. If the voltage is further increased, the dielectric strength of the liquid can be exceeded. This eventually leads to dielectric breakdown of the liquid and causes a destructive short circuit between electrodes (Region IV).

In going from Region I to II, the ions generated from dissociation of impurity molecules within the liquid are often accumulated and absorbed by the electrodes. This can change the electrodes' work function and thus change the voltage required for the emission process in the ion-injection regime (Region III). Therefore, care must be taken in handling the working liquid and the test rig properly, as any level of impurity changes the ionization process and even leads to dielectric breakdown of the liquid. In dealing with EHD pumps, the goal is to limit the operation regime in Region III to prevent a possible breakdown, and thus to ensure a repeatable and stable performance. The voltage at which the transition from Region II to III begins is called the onset voltage. An entire section in Chapter 6 is specifically devoted to this subject.

3.5.1. Breakdown in Dielectric Liquids

A dielectric, or so-called electrical insulator, is a substance that is highly resistant to the flow of an electric current. When high electric field is applied to a dielectric liquid via metal electrodes, space charges are redistributed within the bulk liquid, and additional

electric charges can be injected into the medium at the electrode/liquid interface. This alters the shape of the applied electric field inside the bulk and generates an electric current. However, there is a limit to the current that can be carried by a dielectric medium. If the applied electric field exceeds the dielectric strength of the medium, breakdown occurs. At breakdown, the electric field frees bound electrons. If the applied electric field is sufficiently high, free electrons may accelerate to velocities that can liberate additional electrons during collisions with neutral atoms or molecules in a process called "avalanche" breakdown. Breakdown occurs quite abruptly (typically in nanoseconds), resulting in the formation of an electrically conductive path and a disruptive discharge through the material (Wikipedia, accessed October 2007).

In an EHD micropump, breakdown often generates electric short circuits which severely damage metal electrodes, and thus change the performance drastically. Therefore, it is always advisable to operate the micropump below the possible breakdown threshold.

Many studies were conducted on the dielectric breakdown of insulating liquids ranging from simple atomic rare-gas liquids to polar liquids; however, a single theory is still lacking. One reason is the complex nature of liquids, which makes the theoretical analysis more difficult compared to solids and gases. The other reason is the liquid purity, which has a critical influence on the development of final breakdown (Lewis 1994, Butcher 2005). According to Lewis (1994), insulating liquids generally exhibit low, fluctuating conductivities which are sensitive to electrode conditions and impurities in unspecific ways.

The predominant theory of liquid breakdown is the bubble theory. However, the process of bubble or low-density region formation in the liquid is still not completely understood. Microscopic bubbles can pre-exist in the bulk or can be generated as a result of local heating or electrical stress on the liquid molecules (Jones and Kunhardt 1994, Denat et al. 1999). When one "seed" electron forms within a low density region, it then leads to further ionization and electrical discharges within the vapor bubble, resulting in a complete breakdown. Denat and co-workers (1999) in their report discuss the processes leading to bubble formation in LN_2 as a function of various parameters. They show that once the bubble is created, electrical discharges into the vapor have the largest probability to take place in LN_2 compared to those in hydrocarbons. They also demonstrate that applying P >1.6 MPa can completely prevent bubble formation and electrical discharges into the bubbles. In a literature review conducted by Krahenbuhl et al. (1994), it was also emphasized that pressurizing the system greatly reduces the partial discharge intensity and raises the inception stress.

As will be explained in Chapter 5, in this study, after the system is fully charged with liquid nitrogen before the experiments begin, helium gas at a gauge pressure of about 120 kPa is added to the system to keep the LN_2 subcooled during tests and to prevent the forming of micro-bubbles (the boiling temperature of helium at a gauge pressure of 120 kPa is 5.2 K).

3.5.1.1. Pre-Breakdown Regime in LN_2

Pre-breakdown regimes are observed in many liquids and are often precursors to final breakdown by generating bubbles at the electrode tip (Butcher 2005). Many investigations have studied the bubble formation and pre-breakdown phenomenon in

insulating liquid that includes LN_2: Coelho and Sibillotn (1969), Nosseir and Megahed (1970), Kattan and co-workers (1991), Hanaoka and co-workers (1993), Tobazeon (1994), Pompili and Mazzetti (1995), McCluskey and Denat (1996), and Denat et al. (1999), to name a few.

Butcher (2005) in his Ph.D. dissertation investigates the mechanisms, conditions, and effects of current conduction and liquid breakdown in transformer oil and liquid nitrogen. He shows through a series of experimental results that in LN_2, pre-breakdown spikes occur several microseconds prior to breakdown and that the amplitude of those pulses increases as they approach final breakdown. His results also demonstrate that the light pulses correlate directly with the current spikes.

3.5.1.2. Effect of Polarity on LN_2 Breakdown

Butcher (2005) shows through experimental observations that positive pre-breakdown current pulses (or partial discharges (PD)) in LN_2 are typically broader than negative pulses and lower in amplitude. His results demonstrate that the amount of charge injected is approximately the same for both positive and negative pulses. The luminosity is factor of 3 lower for the positive case which corresponds to the slower injection mechanism. He concludes that the formation of pre-breakdown current pulses for both polarities is related to the properties of the liquid. Since LN_2 is at a temperature very close to its boiling point, the minimal energy required to produce a bubble can easily be attained by the impact of charged particles injected into the fields at either polarity.

Images of LN_2 breakdown taken by Frayssines and co-workers (2002) show that negative breakdown images are “bushy” and appear to be gaseous in nature, and positive events have a thin “streamer-like” filamentary structure, as they occur within the liquid

state. They report that positive breakdown in LN_2 does sometimes exhibit a gaseous nature at pressures below several atmospheres.

Butcher (2005) confirms that LN_2 breakdown shows dual characteristic for given test conditions, meaning that in some cases, positive breakdown appeared to be bushy similar to negative events. According to his results, these characteristics are defined by the fluid properties and energy injection process. A fast rate of energy injection into the liquid even with positive ions can be sufficient for a phase change to occur, while an initially slow rising current does not produce a bubble in the liquid phase. The breakdown under this condition is more likely to appear stream-like.

3.6. Summary

In this chapter, the fundamentals of generation and transport of electric charge carriers in nonpolar liquids under the influence of intense electric field were reviewed, with emphasis given to the characteristics and behavior of liquid nitrogen, as it is the working fluid in this research. In particular, the energy barriers for positive and negative voltage polarities (i.e. field ionization and field emission, respectively) at different metal/liquid interfaces, i.e. Au/LN_2 and Au/Pt, were determined using the method suggested by Arii and Schmidt (1984).

CHAPTER 4: MICROPUMP DESIGN, FABRICATION, AND PACKAGING

The main focus of this chapter is micropump design, material selection, fabrication, and packaging. The pump was designed in accordance with the importance of geometrical parameters on its performance. To evaluate the performance and select the most optimized design, a series of micropump substrates with various electrode geometries and spacing was fabricated using appropriate microfabrication techniques, and packaged by a novel packaging methodology tailored specifically for cryogenic applications in this research.

4.1. Micropump Design

The micropump in this study is a planar ion-drag micropump made of three major parts: a substrate with metal electrodes deposited on its upper surface, a substrate top-cover with an embedded flow channel and inlet/outlet ports, and a bottom plate (Figure 4-1). The primary objective was to design and fabricate a micropump that could generate the desired pressure head at the lowest operating voltage. To do that, each design parameter that contributed to the performance was carefully examined. Among those, electrode geometry, electrode spacing, electrode-pair spacing, and the pump channel height were the most influential. In addition, material selection and compatibility with cryogenic condition were also carefully studied and will be explained in detail in the next sections.

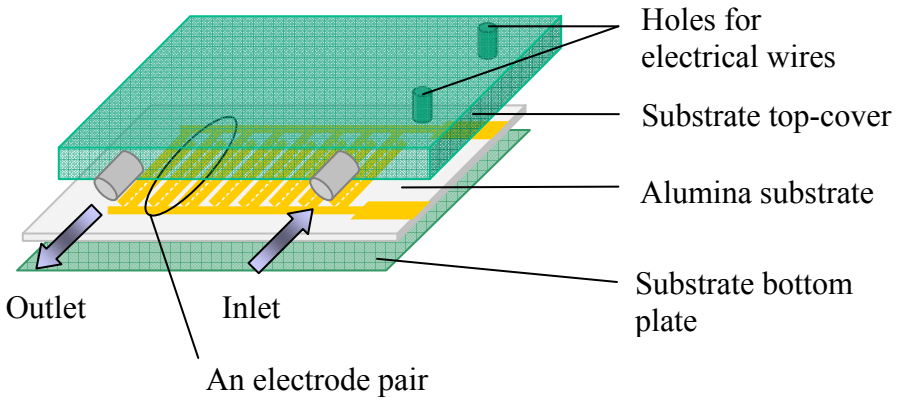

Figure 4-1 Schematic drawing of a micropump

Figure 4-1 shows a schematic drawing of a micropump. It is composed of an alumina substrate on which gold electrodes of submicron thickness were deposited, a top-cover with an embedded channel and integrated inlet and outlet ports, and a bottom plate. All the components were bonded together with a cryogenic-compatible epoxy paste adhesive.

4.1.1. Electrode Design and Geometry

In an ion-drag micropump, the ion-injection phenomenon is the dominant process for generating ions. The pumping effect occurs when a sufficiently high electric potential difference is created between a pair of electrodes, called emitter and collector. The ions are generated mostly at the emitter/liquid interface and move towards the collector because of the electric body force (i.e. the Coulomb force). Friction between the moving ions and neutral molecules drags the working fluid and induces fluid motion.

Electric body force is the main determining factor in the pumping capability of an EHD ion-drag pump and is proportional to the electric field intensity and the rate of ion generation (Equation (2-11)). Electric field intensity and the rate of ion generation at a given electric voltage are related to the mechanical and electrical properties of the

working liquid, the electrode material, and the electrode geometries. Therefore, for an optimized design, one must choose the best working liquid along with a carefully designed electrode geometry, and optimized electrode spacing and channel size, which can together create a strong electric body force and, thus, generate a high momentum transfer to the bulk liquid.

For a given liquid and electrode material, geometrical considerations are the most important factors in the design. The shape of the electrode and the distance between them can highly influence the magnitude and direction of the electric field and therefore make an impact on the rate of electric charge generation at the electrode/liquid interface. Although the EHD charge generation principles are not completely understood, it is well-established that the charge density is a function of electric field and occurs when the electric potential barrier at the electrode metal/liquid interface is overcome (Chapter 3). Therefore, the maximum pump performance can be achieved when the electric field intensity and the charge density are maximized.

For parallel flat electrodes, the maximum electric field intensity is equal to the electric potential difference between them divided by their distance. But for complex geometries, Gauss' theorem should be applied to the boundaries at known potential values (Jackson 1999) and possibly solved numerically in order to find the electric field distribution.

One way to increase the flow rate is to increase the electric field intensity between each emitter and collector pair by lowering the electrode distance (D_{el}), and at the same time reducing the backward flow by increasing the electrode-pair distance (D_{pel}) in order to decrease the opposite electric field formed between adjacent pairs. However, one

should keep in mind that the distance between adjacent pairs on a constant-size substrate cannot be increased too much because of its compromising effect on the number of electrode pairs, leading to fewer ion-injection sites. Nor can the electrode distance be decreased too much, as it increases the probability of liquid breakdown.

Another way to increase the flow rate is to increase the electric field intensity at the electrode edges by designing electrodes with more a sophisticated geometry compared to flat ones. One example is the saw-tooth shape electrodes, which can substantially enhance the ion generation (Benetis 2005) due to the creation of a very high electric field, sometimes on the order of a few megavolts per meter at the electrode tips. In this study, the electrode shape design is restricted to flat and saw-tooth where the saw-tooth electrodes have a fixed 53° angle at the tips (Figure 4-2 a-b).

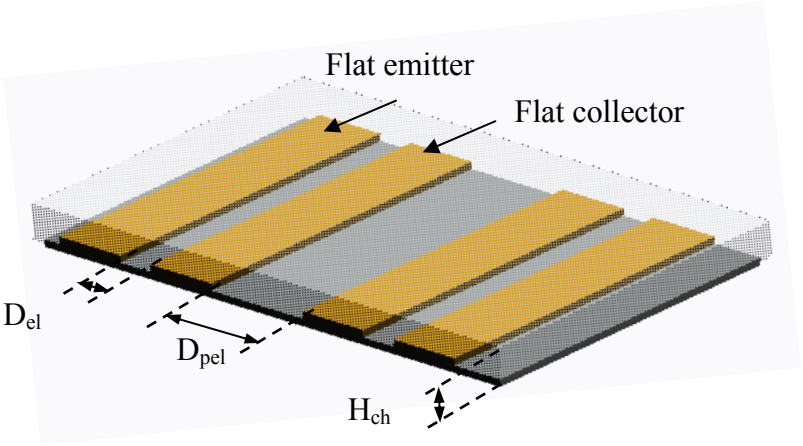

a) flat-flat combination electrodes

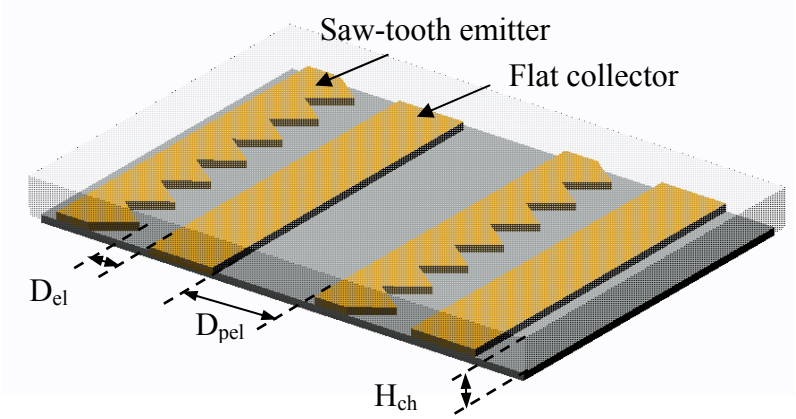

b) saw-tooth-flat combination electrodes

Figure 4-2 Schematic drawings of the micropump's electrodes

In the present study, thin-film deposition techniques are employed to create several contiguous gold electrode pairs (0.3 μm thickness) in a comb-like structure on the alumina substrate. The fabrication technique will be explained in detail later in this chapter.

To investigate the effect of various parameters on the performance, four designs of micropumps were selected. Each design had one or two parameters different from one another. As shown in Table 4-1, the designs included different emitter shapes: flat and saw-tooth; inter-electrode spacing (D_{el}): 20 and 50 μm; electrode-pair spacing (D_{pel}): 80, 100 and 200 μm; and channel height (H_{ch}): 130 and 260 μm. The micropumps had successfully passed dozens of thermal-cycling tests between room temperature and the liquid nitrogen environment with an internal pressure of 500 kPa prior to testing. The micropumps were tested at different DC voltages ranging from 0 to 2.5 kV.

Table 4-1 Different designs of micropump

Design	D_{el}(μm)	D_{pel}(μm)	Emitter shape	Number of stages
(50,100,f)	50	100, $2D_{el}$	f	79
(50,100,s)	50	100, 2 D_{el}	s	74
(50,200,s)	50	200, 4 D_{el}	s	54
(20, 80, s)	20	80, 4 D_{el}	s	90

- f & s: electrode shapes (flat & saw-tooth)
- D_{el}: emitter-collector inter-electrode spacing
- D_{pel}: electrode-pair (stage) spacing
- H_{ch}: channel height (130, 260 μm)

4.1.2. Flow Channel and Top-cover Design

The micropump substrate cannot function by itself. It actually needs to be accompanied by a top-cover which acts as the fluid flow passage. The use of a flat substrate and very thin electrodes requires a shallow, flat channel to effectively cover the electrode area. Therefore, the top-cover provides a flow channel in addition to the inlet and outlet ports to let the working fluid easily flow in and out of the channel.

The flow channel was designed in accordance with the substrate shape and the electrode effective area. In this research, the overall substrate size and active electrode area are constant regardless of electrode shape and spacing. This makes channel height the only variable in the channel geometry as the channel width and length are kept constant.

To find the optimum channel height, the effect of the channel height and electrode thickness on pressure drop needs to be studied. Due to the sub-micron thickness of the electrodes, the pressure drop introduced by their presence in the fluid path can be considered negligible with a high degree of accuracy. Thus, the major pressure drop is because of the viscous shear stresses introduced by the channel walls. In an ion-drag pump, the pumping effect is achieved when the electric shear stresses become higher than the viscous shear stresses. Therefore, the optimum channel height is to be found as the result of the counterbalancing effects of the charge boundary layer (electric body sheer stress) and the pressure drop due to viscous shear stresses and fluid recirculation inside the channel. In deep channels (> 450 μm), the fluid recirculation contributes most to the pressure drop, while in extremely shallow channels (< 50 μm) the huge viscous losses make it impossible to create any flow.

The EHD phenomenon indicates that the charge boundary layer that is generated in the vicinity of the electrodes acts best with a several hundred-micrometer channel depth. Results of Benetis's numerical modeling along with the experimental data show that the optimum channel height for this substrate geometry and electrode effective area is about 260 μm for HFE 7100 as the working liquid (Benetis 2005).

In this research, most investigations were conducted with 260 μm channel heights. However, the effect of a 130-μm channel height was also studied briefly. Figure 4-3 shows a drawing and picture of the top-cover with a flow channel. The channel was carved onto one side of a small block of G-10 using micromachining techniques. The channel is a 14 mm x 27 mm flat, square-shaped conduit with round edges and two holes acting as the channel's inlet and outlet. The size of the G-10 block is 3 cm (width) x 5

cm (length) x 0.5 cm (height). The substrate was later glued between the top-cover and the bottom plate as part of the packaging process. The bottom plate was made from another piece of G-10 that was approximately 4 cm (width) x 6 cm (length) x 0.1 cm (height) as shown in Figure 4-9.

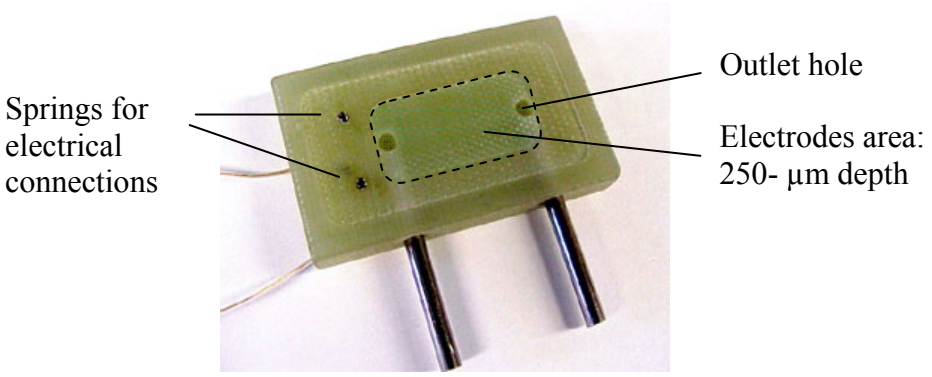

a) Inner side of a top-cover with embedded springs for electrical connections

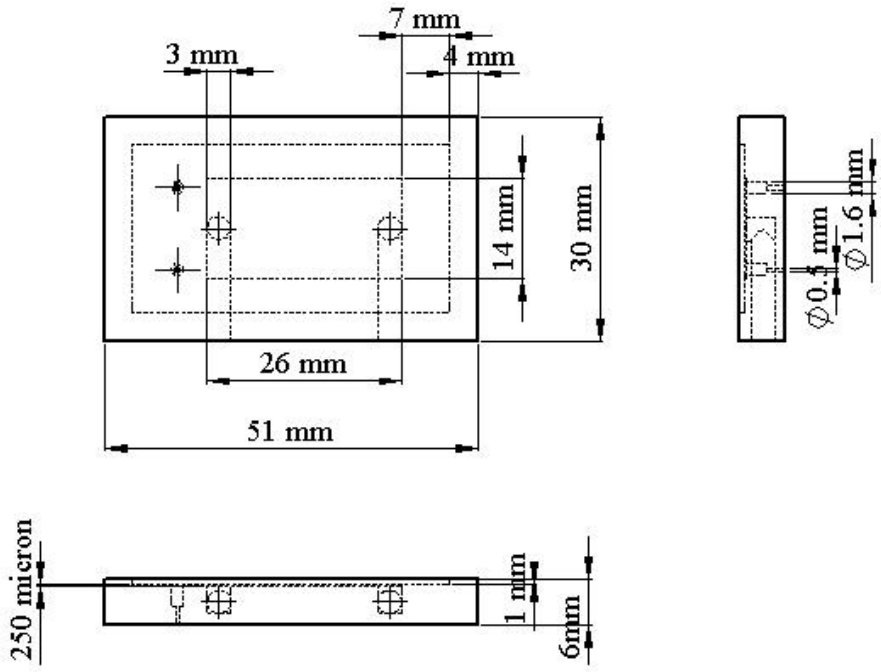

b) Drawing of 3 sides of a top-cover

Figure 4-3 Photograph and drawings of a micropump top-cover

4.2. Material Selection and Fabrication

The micropump in this study is a planar ion-drag micropump made of three major parts (Figure 4-1). Material selection for these parts is affected by a number of limiting factors, such as fabrication methods, the challenging nature of the EHD ion-drag phenomenon, the environment in which the micropump operates, and the compatibility of the materials in the working environment. Therefore, a thorough investigation of material compatibility and fabrication techniques was conducted before a successful prototype could be delivered.

4.2.1. Substrates and Electrodes

The micropump's main part is the substrate on which the electrodes are deposited. A thin layer of aluminum oxide (Al_2O_3) or alumina is by far the substrate material of choice in this research. Alumina is an excellent thermal and electrical insulator with higher durability and hardness than silicon. Its high electrical resistivity makes it particularly useful in EHD applications, where it ensures the isolation of metallic electrodes. In many applications, where a small temperature difference exists, oxidized silicon would be the perfect choice for the substrate due to its smoothness and commercial popularity in semiconductor industries. But in a cryogenic environment, where the system undergoes a temperature difference of often more than 200 K, all the system's components must be chosen so as to prevent crack formation or metal peeling due to differences in their coefficients of thermal expansion (CTE). Table 4-2 lists some physical properties of the materials used in different components of the micropump.

Table 4-2 Coefficient of thermal expansion of the materials used in the micropump

Material	stainless steel	chromium (Cr)	gold (Au)	platinum (Pt)	alumina (Al_2O_3)	SiO_2 (fibers)	G10
CTE ($10^{-6}K^{-1}$)	17.3	4.9	14.2	8.8	5.4- 8.7	0.4- 0.55	10-13

As shown in the table above, alumina, with its low CTE, is a much better choice for the substrate compared to silicon oxide. In addition, other features such as minimum outgassing and high thermal conductivity make it an excellent choice for the EHD micropumps.

Alumina substrates with an approximate size of 2.5 cm x 3.5 cm x 0.05 cm were purchased from CoorsTek in large quantities. Their low aspect ratio (width/length) worked well with photoresist spinning. They were polished by the manufacturer to different surface roughness: 0.2 μm and 0.02 μm. The former was mainly used in this research, as Benetis (2005) showed no dependency of the EHD pumping performance on the surface roughness and that more roughness created a stronger bond between the metal electrodes and the substrate, which prevented peeling.

Metal electrodes were fabricated from thin layers of gold and chromium deposited on the substrates. Gold was the main electrode metal, but since it does not adhere strongly to ceramic, a layer of chromium was deposited between the gold film and the substrate to provide sufficient adhesion.

Gold was chosen due to its high resistivity to oxidation. Working with high electric fields in EHD operations, the least corrodible metal with the least work function was desired. Platinum was the number one choice in terms of being the least corrodible metal, but its microfabrication yield was very low as it could be hardly etched. Gold was

therefore selected as the main electrode material in this research. It has quite a large work function compared to other metals such as aluminum and niobium, which is a disadvantage in EHD operations. But its overall high resistivity to corrosion outweighs its high work function and high cost. Benetis (2005) in his dissertation has listed oxidation potential and work function of different common metals.

4.2.1.1. Gold and chromium deposition

Initially thin layers of chromium and gold are deposited by thin film deposition technique on alumina substrates, and then patterned to the desired shape and geometry. However, before depositing the metal layers, wafers that have been in storage must be chemically cleaned to remove contamination. In this study, acid mixtures such as Aqua Regia and Piranha are used. The standard aqua regia is a mix of 3 parts 37% HCl: 1 part 70% HNO_3 (a diluted solution of aqua regia has additional 2 parts H_2O). Aqua regia targets noble metals and was found to etch gold, palladium, nickel, copper, molybdenum, and aluminum rapidly.

The Piranha (also known as sulfuric-peroxide) used here is a mix of about 50 parts 96% H_2SO_4: 1 part 30% H_2O_2 at T=120°C. It is used as a cleaning solution that strips organics and some metals. Piranha was found to etch photoresist, aluminum, nickel, and silver rapidly, but chromium slowly.

The wafers are soaked in aqua regia, rinsed with DI water and dried with N_2 before being cleaned in piranha solution for at least 15 minutes. They are then rinsed with DI water and dried before immediately being transferred into the e-beam chamber for gold and chromium deposition. Chromium and gold films with thickness of 200 Å

and 0.3 μm, respectively, are deposited on the substrates using the thermal evaporation technique (Figure 4-4b).

4.2.1.2. Multistep Microfabrication of Electrodes (Photolithography)

Series of gold electrodes (flat and/or saw-tooth) are patterned using the photolithography method (Figure 4-4b-h). A single cycle of photolithography combines several steps in sequence to selectively remove parts of a thin film. It uses light to transfer a geometric pattern from a photomask to a light-sensitive chemical (photoresist) on the substrate. A series of chemical treatments then engraves the exposure pattern onto the material underneath the photoresist.

This method is among the simplest and most cost-effective microfabrication techniques and allowed us to fabricate micropump prototypes at the University of Maryland microfabrication facilities at a fraction of the cost needed for similar commercial orders. Some of the micropump's features, such as electrode spacing and electrode geometrical dimensions, are restricted by microfabrication technology tolerances, but micropumps with flat and saw-tooth electrodes and electrode spacing down to 20 μm are produced at pretty high yield in this facility. The yield and fabrication tolerances have to do a lot with the air quality inside the clean room, the purity of materials, the quality of masks (budget considerations), and the electrode design.

The multistep microfabrication procedure using a positive mask for flat and saw-tooth electrodes is shown schematically in Figure 4-4a-h.

a) Wafer cleaning: aqua regia and piranha are used to clean the wafer from surfactants before gold and chromium are deposited on the wafer surface. The wafer is then heated to 110°C to drive off any moisture that may be present on the surface.

b) Deposition: thin films of chromium (200 Å) and gold (0.3 μm) are deposited on the substrates using the thermal evaporation technique.

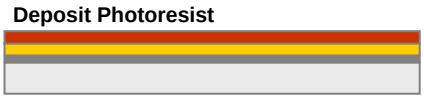

c) Photoresist application: the wafer is covered with positive photoresist by spin coating (at 4000 rpm for 20 s) to produce a layer of 1.5 μm thick. The photoresist-coated wafer is then prebaked (soft-baked) on a hot-plate at 80 °C for 1 minute to evaporate the coating solvent.

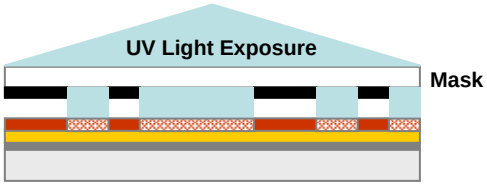

d) Alignment and exposure: the coated wafer is placed on the chuck of a lithography machine and aligned with the mask. The photoresist is exposed to UV light for 8 s.

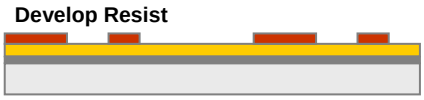

e) Developing: the coated wafer is rinsed with developer solution (CD 30) for 30 s to dissolve the exposed area on the photoresist layer. The wafer is then rinsed with DI water, and hard-baked for 8 minutes at 110 °C on a hot-plate.

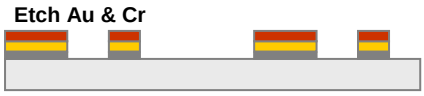

f) Etching: the wafer is first immersed inside gold etchant solution to remove the unprotected area of gold, then rinsed with DI water, and placed in chromium etchant solution to remove the unwanted area of chromium layer.

g) Photoresist removal (stripping): the photoresist, which is no longer needed, is removed from the substrate with liquid resist stripper.

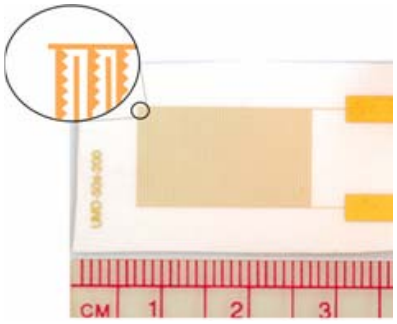

h) Top view of a micropump substrate, courtesy of S2TS lab

Figure 4-4 Multi-step microfabrication of micropump substrates (a-h)

Electrodes are inspected for defects, short circuits or broken bus lines during every stage of the fabrication process. Once the perfect samples are ready, they are photographed through a microscope, packaged, and prepared for testing. After each micropump is finished with testing, the package is disassembled and its electrodes are inspected again to measure the level of degradation and damage. Figure 4-5 shows photographs of perfect and imperfect electrodes coming right out of the final step of microfabrication.

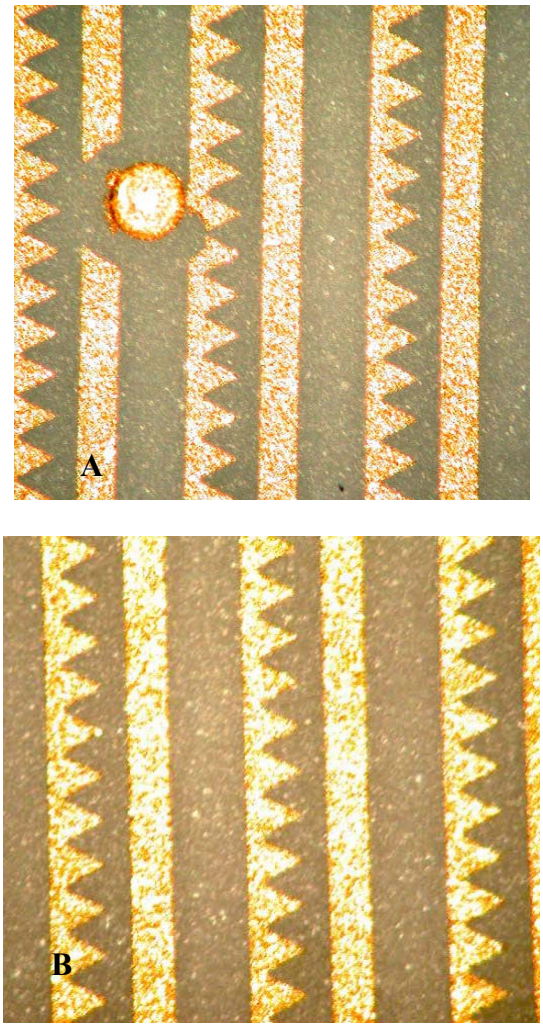

Figure 4-5 Photographs of newly made A) defected electrodes, and B) flawless electrodes

4.2.1.3. Platinum Electroplating

In ion-drag EHD pumping, high electric field gradients exist in the areas close to the electrodes. For various reasons, this could lead to local electric discharges that could raise the local temperature and cause the electrodes to corrode and melt. This issue affects run-to-run repeatability and reduces pump lifetime. Figure 4-6 shows some melted parts of the electrodes of a micropump that was tested for several hours.

Figure 4-6 Photographs of Cr/Au electrodes on alumina substrate, 40x objective.

One way to improve the lifetime of the electrodes is to use more corrosion-resistant material, such as platinum, for electrode fabrication. Since Pt is a very hard substance, it was very difficult to work with it in the microfabrication processes, and in most cases it resulted in a very low yield. However, platinum electroplating was considered as an alternative to make the micropumps more resistant to corrosion. Thus, initially micropumps with gold electrodes were fabricated, and then a layer of platinum was deposited on top of the gold electrodes using the Pt electroplating process. The specifications of the electroplating solution and the schematic drawing of the setup are shown in Figure 4-7.

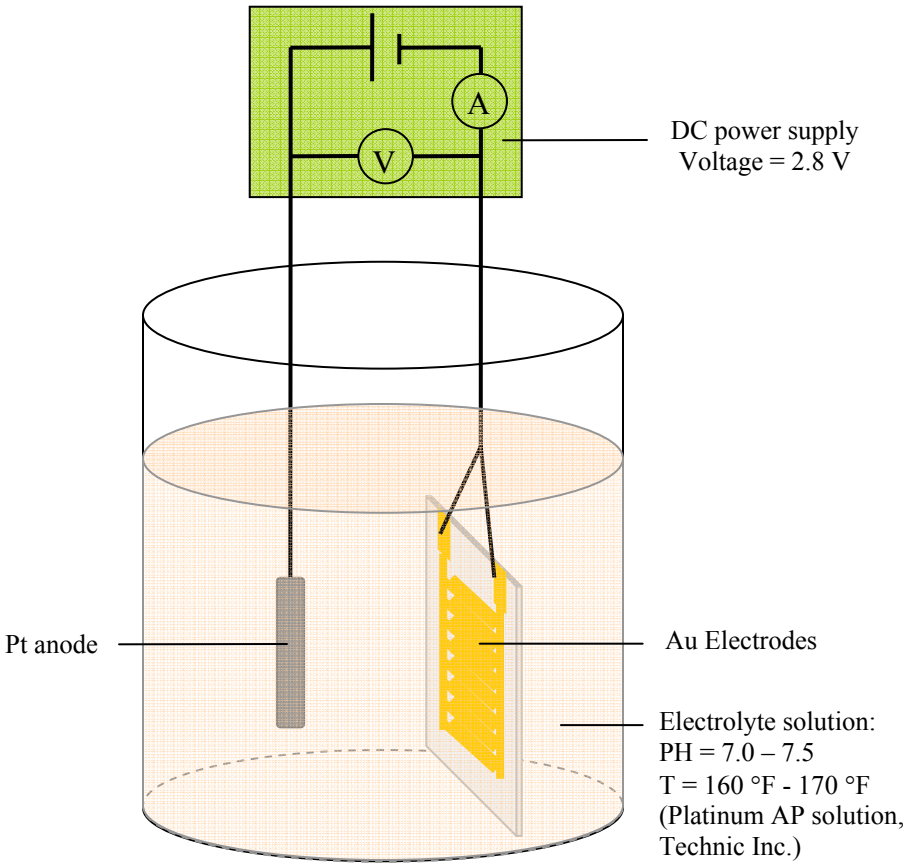

Figure 4-7 Schematic drawing of the Pt electroplating setup

After successfully fabricating some micropump substrates with platinum deposition, they were photographed, packaged and tested. Figure 4-8 shows a photograph of a micropump's electrodes with only emitters electroplated with Pt. The contrast clearly indicates that the gold emitters are completely covered by a layer of platinum.

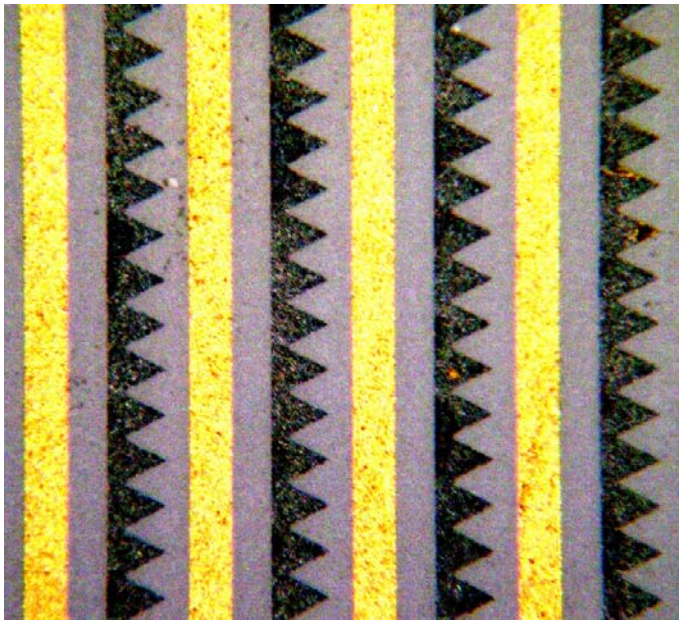

Figure 4-8 Photograph of a micropump's electrodes: gold collectors and Pt-plated gold emitters

4.2.2. Top-cover and Bottom Plate

G-10 is one the best candidates for the top-cover's main structure, whose key purpose is to create a flow channel over the substrate. G-10 or FR-4 grade is a continuous glass woven-fabric base impregnated with an epoxy resin binder under pressure and heat. G-10 was first introduced in the 1950's, but what is referred to as G-10 today is actually FR-4, the flame retardant version of G-10. It is available in many different sizes and shapes and has a natural yellowish to light green color.

G-10 was particularly selected because of its outstanding characteristics, such as high flexural strength, cryogenic serviceability and excellent dielectric stability both in ambient and cryogenic conditions, as well as for its close expansion coefficient to alumina.

In addition, it can be nicely machined to create a variety of channel heights with high precision at very low cost. Some of its properties and area of application are listed in Table 4-3.

Table 4-3 Properties and application areas of G-10

Properties	**Applications**	**Availability**
High dielectric strength Chemically resistant High flexural strength Dimensional stability Low moisture absorption Cryogenic serviceability	Electronics industries Aerospace industries Underwater conditions Cryogenic environment	Different sizes and shapes

The top-cover was made from a piece of G-10 of approximately 3 cm x 5 cm x 0.5 cm, and the bottom plate was made from a piece of 1-mm-thick G-10 of approximately 4 cm x 6 cm.

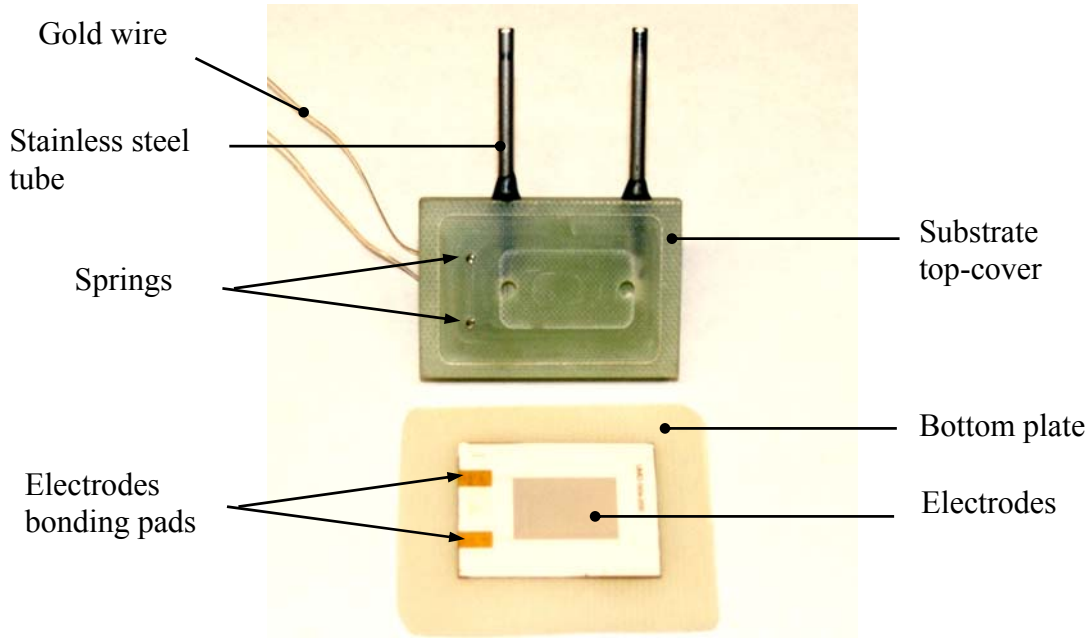

Figure 4-9 Picture of a micropump's components

Other components of the top-cover are the 0.125" (≈ 3.175 mm) stainless steel tubes used for the inlet and outlet ports and the stainless steel springs and gold wires used to provide electrical connections between the electrodes bonding pads and power supply and measurement devices.

4.2.3. Working Liquid Properties

In this study, liquid nitrogen was the main working fluid. Liquid nitrogen is a common cryogenic liquid that is extremely environmentally friendly and has a boiling point of 77K. Table 4-4 provides a list of some physical properties of common cryogenic liquids that are sorted based on their boiling points. Among those, only neon and helium have boiling points that are lower than nitrogen's boiling point. Most electronic devices which have components made of superconducting materials require cooling below 77K; this would leave LN_2 by far the greatest liquid for cryogenic cooling purposes. LN_2 can

also carry a fair amount of heat before its temperature rises one degree. Its specific heat as listed in Table 4-5 is almost one-half that of water.

Table 4-4 Boiling point and dielectric constant for common cryogenic liquids (CRC 1997)

	Boiling point (K)	**Freezing or triple point (K)**	**Dielectric constant**
Helium	4.2	----	1.05 @ 4.2K
Neon	27.2	83.8	1.52 @ 87K
Nitrogen	77.4	63.2	1.43 @ 77K
Argon	87.3	83.8	1.52 @ 87K
Oxygen	90.2	54.4	1.49 @ 90K
Methane	112	91	1.7 @ 112K
Ethane	184.5	90.35	1.94 @ 95K
Iso-Butane	261.4	113.6	1.4 @ 272K

The dielectric constant of most common cryogenic liquids is relatively lower than those of common refrigerants in ambient temperature. This is also valid for LN_2, which has a value of 1.43. This eventually leads to a pretty low pressure-head generation compared to those with liquids such as HFE7100. As explained before, the higher the dielectric constants, the higher the pressure head generation. LN_2 is considered an insulating liquid due to its extremely low electrical conductivity, which makes it a good candidate for high efficiency ion-drag pumping. Chapter 3 gives detailed information

about LN_2 electrochemical properties as well as ionization processes and their effect on the EHD phenomenon.

Table 4-5 Liquid nitrogen thermophysical properties

Boiling Point at 1 atm (K)	77.348
Liquid density (kg/m^3)	806.63
Liquid kinematic viscosity (cSt)	0.205
Liquid specific heat (J/kg.K)	2030
Thermal conductivity (W/m.K)	0.02598
Dielectric constant	1.434
Latent heat (kJ/kg)	198.3

4.3. Micropump Packaging

It is important and challenging to select proper materials and adhesive for bonding purposes at very low temperatures. The CTE mismatch between dissimilar materials increases at low temperatures and causes the failure of regular epoxies, which causes the packaging to fail. The packaging procedure developed in this study is cryogenic-compatible and enables the pump package to withstand several atmospheres of pressure and a drop in temperature of more than 200 K.

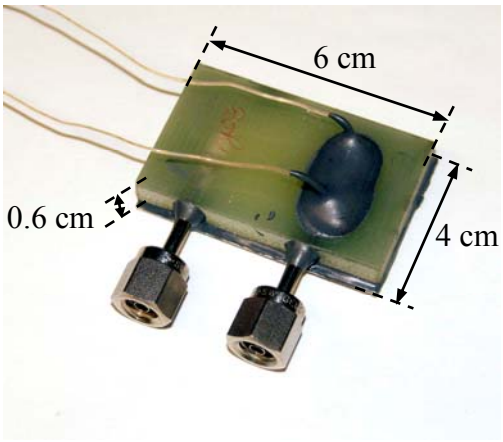

Figure 4-10 Picture of a packaged micropump

The package consists of a top-cover and a bottom plate that sandwich the substrate and are bonded together by a low-temperature compatible epoxy adhesive paste. Figure 4-10 shows a picture of micropump which is approximately 4 cm x 6 cm x 0.6 cm.

4.3.1. Electrical Connections

One of the main challenges of developing the micropump package is to integrate the electrical connection into the package main structure. Electrical connections connect the electrode bonding pads on the substrate to the power supply. When the first series of prototypes was fabricated, electrical wires were soldered to the bonding pads. That was inefficient and inconvenient; neither did it have a high yield. Therefore, a spring-type connection was designed and later replaced the wire-soldering method. In this technique, the electrical connection between a wire and a bonding pad is mechanically established by a small spring where the bonding pads on the front side of the substrate are pressed against the inner side of the top-cover.

The springs are first fixed into the top-cover by very small screws. Then, the spacing between the spring and the hole is filled with the epoxy glue.

4.3.2. Adhesive Paste

Another challenge faced while developing the package was the possibility of disassembling the micropump for further inspection and assembling it again if required. Therefore, fixing the position of bottom plate using some kind of epoxy paste was of critical importance. The bottom plate was initially designed to be fully glued to the back of the substrate and from the sides to the top-cover. This procedure made it almost impossible to disassemble the package safely and most often, the substrates and thus the electrodes were damaged. The current design, however, resolved the issue and allowed the top-covers to remain intact and even be reused. In the new design, the bottom plate was made of a thin layer of G-10 and cut larger than the top-cover in order to act as a base. As shown in Figure 4-9, the substrate was clamped between the top-cover and bottom plate, while the epoxy past adhesive was used to provide a strong bond between various components (Figure 4-10).

The epoxy adhesive paste used in this research is Hysol EA 9361 made by Henkel-Loctite Aerospace (Düsseldorf, Germany). It is a two-component paste adhesive that cures at room temperature and is suitable for applications that require high elongation, such as sealing and cryogenic applications.

4.4. Summary

This chapter was dedicated to the micropump design, material selection, fabrication methods, and packaging. Thin-film deposition and photolithography-etching techniques were employed to create several contiguous metallic electrode pairs (emitter and collector pairs) in a comb-like structure on the alumina substrate. The top-cover provides a flow channel as well as inlet and outlet ports. To evaluate the effect of various

geometrical parameters on micropump performance, a series of micropumps with various electrode geometries and spacings were introduced for further tests and experimental investigations.

CHAPTER 5: EXPERIMENTAL SETUPS AND MEASUREMENT TECHNIQUES

In this study, four designs of micropumps were selected to study the performance effect of various parameters. To test the micropumps, two test rigs (hereafter referred to as the first- and second-generation) were designed and built for different measurement purposes. They either measured flow rate or static pressure head at different applied voltages while the pump operated in a flow loop. Common characteristics of both test setups were their cryogenic compatibility, their ability to hold high vacuum, their liquid charging/discharging capabilities, and their sensitive instrumentations for low current and differential pressure head measurement.

5.1. Flow Rate Measurement Test Setup

The first generation test setup was designed to measure the generated flow rate. It consisted of a liquid nitrogen Dewar flask, a vacuum chamber, an external nitrogen gas tank, and a flow loop for evaluating flow rate generation as shown in Figure 5-1. The Dewar flask had an inner diameter of about 1 m to enclose the vacuum chamber properly. The vacuum chamber was designed to enclose the flow loop and help maintain a high vacuum around it for measurement purposes.

A series of feed-through connectors was used to carry all the electrical wires through the vacuum chamber flange cap. A computerized data acquisition system (DAS) was also used to collect and record the test data for further processing.

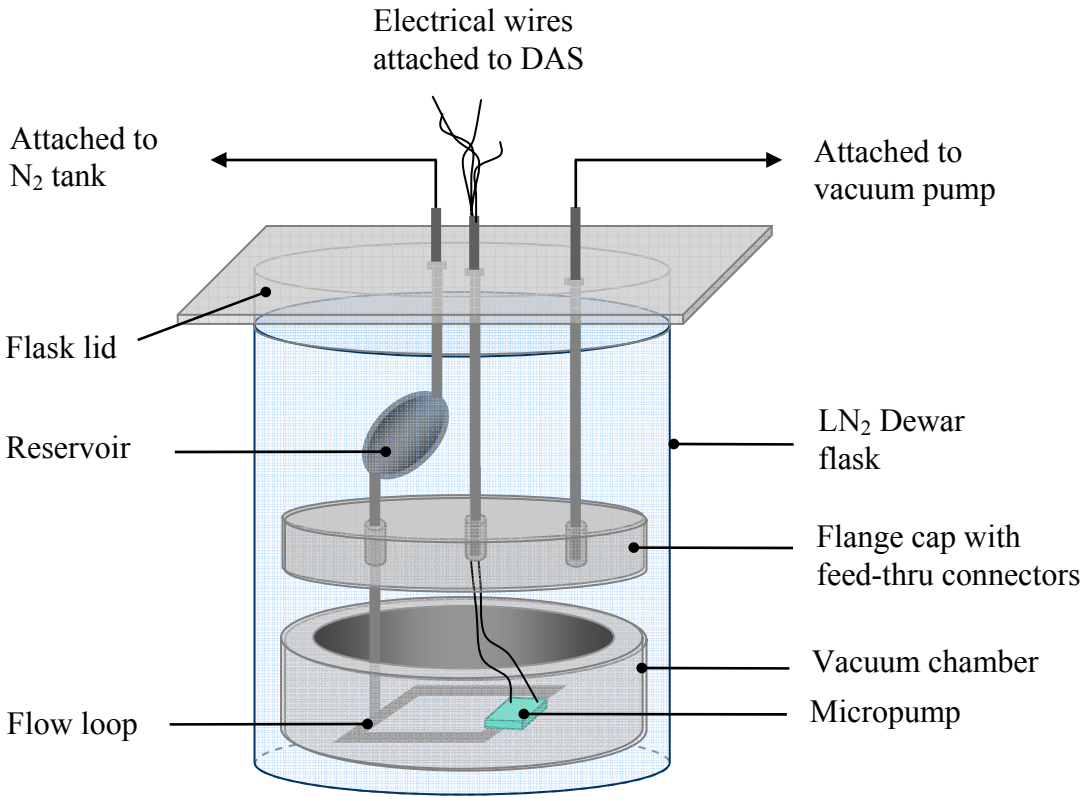

Figure 5-1 Schematic diagram of the first generation test facility

The flow loop was mainly made of stainless steel tubing with an outer diameter of 3.17 mm and a wall thickness of 0.25 mm. The loop consisted of a micropump, a heater, and a number of temperature sensors. It was attached to the inner wall of the flange cap by two pieces of stainless steel tube. The tubes were used as "cold fingers" and to attach the loop to the LN2 reservoir and the vacuum pump. Figure 5-2 shows a photograph of the flow loop mounted on the inner side of the cap.

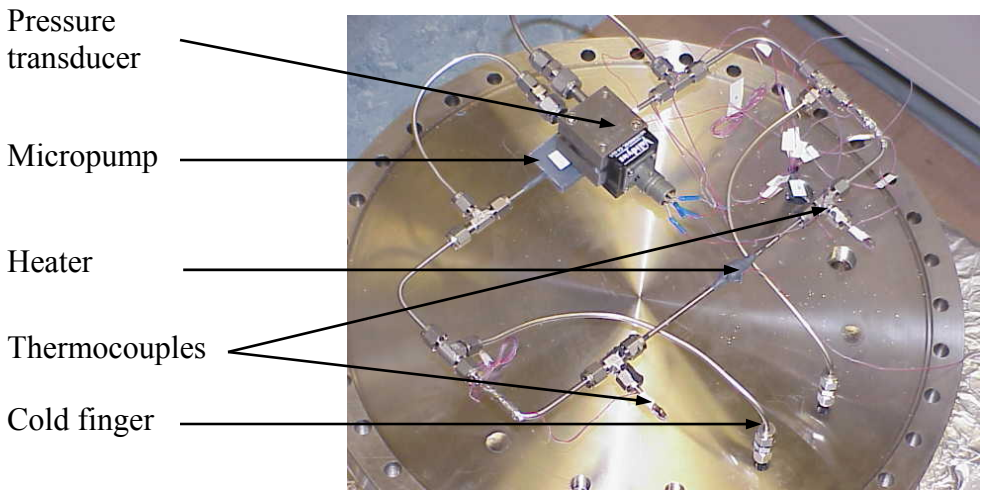

Figure 5-2 Photograph of the flow loop, part of the first-generation test set-up

Matched thermocouples were placed symmetrically up- and downstream of the heater, shown in Figure 5-2 and Figure 5-4. As will be explained later, these thermocouples were used to measure the mass flow rate of liquid nitrogen, based on an energy balance around a heating section of the loop.

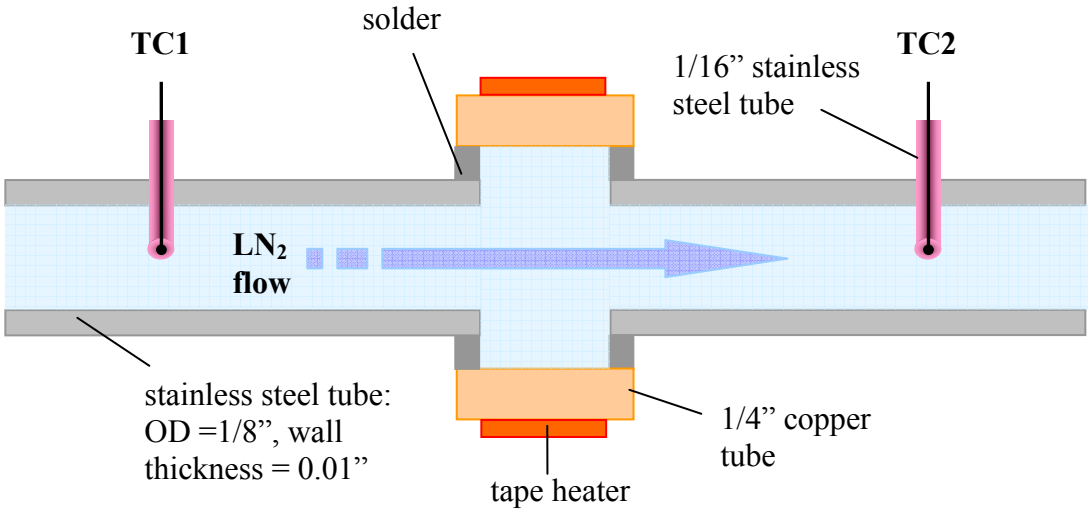

Not to scale

Figure 5-3 Cross-sectional view of the heating part of the flow loop

Other temperature sensors were installed inside the vacuum chamber and on different spots in the flow loop to allow monitoring of the temperatures at other locations and of other components.

5.1.1. Experimental Procedure

To prepare the test rig for experiments, the vacuum chamber and flow loop initially underwent a high vacuum (about 10 millitorr). The vacuum chamber was then placed inside the Dewar flask and completely submerged in liquid nitrogen. A copper gasket sealed the vacuum chamber. The external nitrogen gas tank fed ultra pure (99.998%) nitrogen gas into the test loop. This external tank also served as an expansion tank for dampening the pressure fluctuations in the test loop. The liquid nitrogen reservoir worked as a device for liquefaction of the nitrogen gas. The liquid nitrogen then flowed from the reservoir into the flow loop and cooled it down.

After the flow loop was completely filled with liquid nitrogen and the temperature sensors around the test loop uniformly read 77 K, the test was started by applying a DC voltage to the EHD micropump. During each test, average pressure and temperature inside the test loop were kept at 200 kPa and 77 K, respectively. Thus, the liquid nitrogen inside the loop was sub-cooled to approximately 7 K (boiling point of LN_2 at 200 kPa is approximately 84 K). That degree of subcoolness was enough to prevent the liquid nitrogen from boiling due to the slight heating applied for measuring the flow rate.

At each DC voltage, a small amount of heat was applied to the heater and the difference between upstream and downstream temperatures was measured. The temperature difference was then used to determine liquid nitrogen flow rate in the loop using an energy balance technique, which is explained in the next section.

5.1.2. Flow Measurement Based on Energy Balance

Tests were performed by applying DC voltage to the micropump. When the pumping effect began, LN_2 flowed around the loop. In this system, the flow rate could not be measured directly by conventional flow rate measurement devices. Instead, an energy balance technique was used to measure the flow rate. The concept of this technique is based on the first law of thermodynamics, which states that at steady-state condition, the total energy flowing into the system is equal to the total energy flowing out of the system. Figure 5-4 shows schematic diagram of the flow loop with the heater section and upstream and downstream thermocouples.

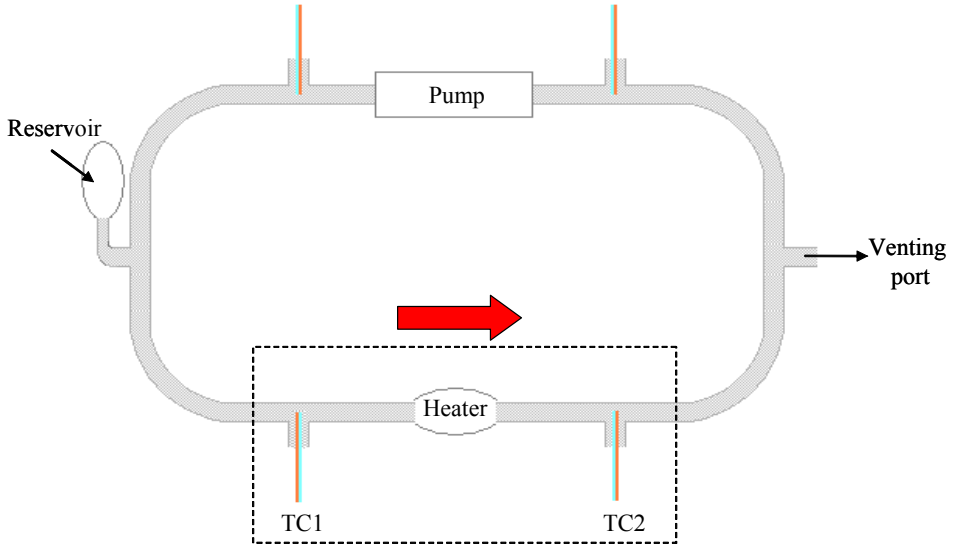

Figure 5-4 Schematic of the flow loop and the heating section

To measure the flow rate, a known amount of heat was applied to a small section around the circumference of the loop where the heater is located. The amount of heat was adjusted so that the liquid temperature adjacent to the heater remained below its saturation temperature at the applied pressure. Heat was then transferred to the fluid

flow, thus changing its temperature. At all times, temperatures upstream (TC1) and downstream (TC2) of the heater were measured with matched thermocouples. The difference between these two temperatures is a measure of the flow rate based on Equation (5-1):

$$\dot{V}_c = \frac{\dot{Q}_{heater}}{\rho c_p \Delta T_m} \tag{5-1}$$

where ΔT_m is the temperature difference between TC1 and TC2, which is measured by DAS, $\dot{Q}_{heater}$ is total heat generated by the heater or the product of voltage and current, and $\dot{V}_c$ is the flow rate, which is calculated based on Equation (5-1).

In reality, it is virtually impossible to completely prevent heat losses (Figure 5-5). Because of that, only a fraction of total heat, $\dot{Q}$, is transferred into the fluid flow ($\dot{Q} < \dot{Q}_{heater}$). As a result, the measured temperature difference is smaller than a temperature difference that would occur at a no-heat-loss condition. This causes the calculated flow rate to become larger than the actual flow rate or $\dot{V}_a < \dot{V}_c$ (Equation (5-2)).

$$\dot{V}_a = \frac{\dot{Q}}{\rho c_p \Delta T_m} \tag{5-2}$$

To reduce the measurement error, a calibration curve that relates the calculated flow rate, $\dot{V}_c$, to the actual flow rate, $\dot{V}_a$, had to be found. This was done through careful examination and simulation of the system, which is explained in the next section.

5.1.3. Numerical Calibration Curve

The calibration curve could not be obtained experimentally in the cryogenic environment due to the complexity of the system. Therefore, a numerical model was developed to simulate the system for the exact experimental condition. In the model, at a certain flow rate $\dot{V}_a$, a known amount of heat $\dot{Q}_{heater}$ was applied to the system and ΔT_m was measured. A flow rate $\dot{V}_c$ was then calculated for each $\dot{Q}_{heater}$ and ΔT_m and plotted versus $\dot{V}_a$. The numerical calibration curve was validated using experimental results from the tests conducted at ambient condition with water under vacuum. Because of the vacuum, heat losses are significantly reduced around the flow loop, similar to the cryogenic test conditions.

To start with the model, a clear understanding of all the heat losses was necessary. In this system, most losses are identified as radiative heat loss due to temperature difference between liquid inside the loop and its outside environment, heat loss due to natural convection around the tube because of the remaining air inside the vacuum chamber, and conductive heat loss through the stainless steel tubing. Figure 5-5 shows a schematic of the heating part of the flow loop with all the possible heat losses.

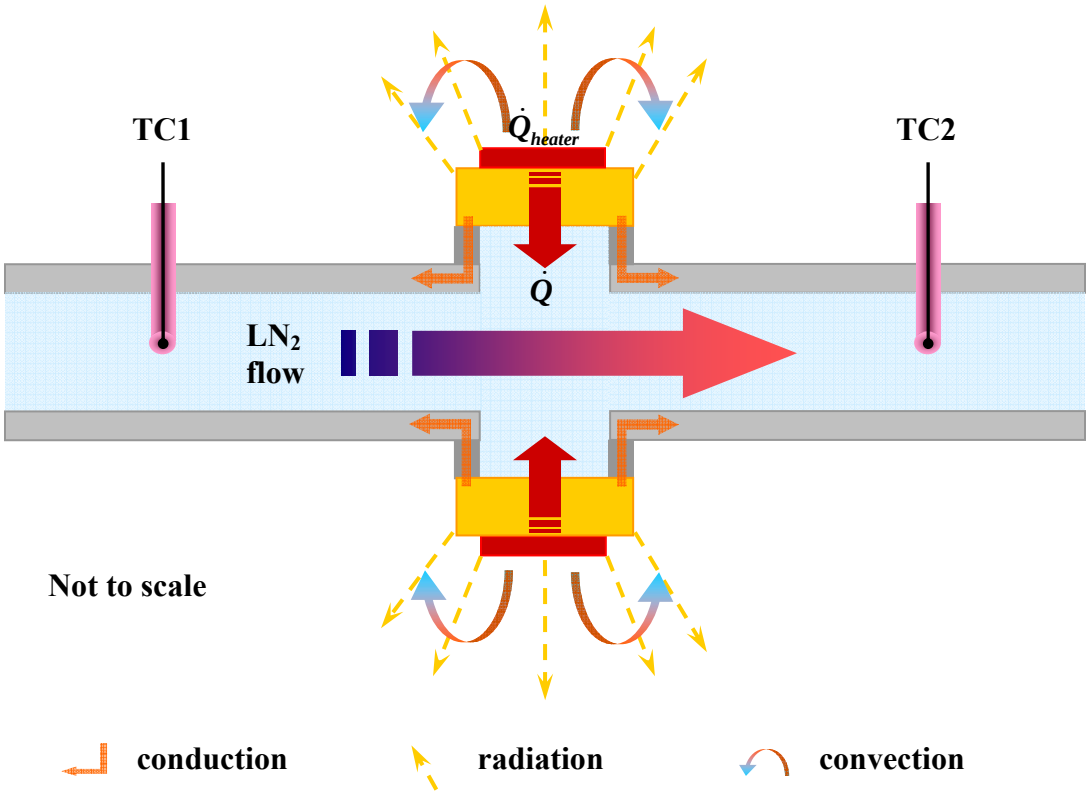

Figure 5-5 Cross-sectional schematic of the heating part of the flow loop with various heat transfer modes when heater is on and a flow exists

5.1.3.1. Convective Heat Loss

Since the flow loop is surrounded by a closed chamber, and there is no air or liquid flow around it, the convection coefficient is to be calculated only for natural convection around the loop. To do so, first the air density is calculated for the level of vacuum in the vacuum chamber. The vacuum pump can deliver vacuums up to 10^{-3} torr. However, in our calculation, we took the minimum deliverable vacuum to the chamber which is about 10^{-2} torr or 1.333 Pa. Therefore, the air density at P = 1.333 Pa and $T = \frac{T_s + T_\infty}{2} = \frac{85+77}{2} = 81K$ is estimated using equation (5-3):

$$\rho_{air} = \frac{P}{R_{air} T} = 5.545 \times 10^{-5} kg/m^3 \quad \textbf{(5-3)}$$

where R_{air} = 296.8 J/kg.K is the air gas constant, T_s is temperature of the heater surface, and T_∞ is the air temperature inside the chamber.

Other physical properties of air such as dynamic viscosity, thermal conductivity, and specific heat, were also found at 81 K: η_{air} = 5.358 x 10-6 kg/m.s, k_{air} = 0.00814 W/m.K, $c_{p,air}$ = 3129 J/kg.K (ASHRAE Handbook 2001).

The Rayleigh number (product of the Grashof and Prandtl numbers) for a long horizontal cylinder is calculated using equation (5-4) (Incropera and DeWitt, 2002):

$$Ra_D = Gr_D.\Pr = \frac{g\beta(T_s - T_\infty)D_h^3}{\nu\alpha} = 6.84\times10^{-6} \quad \textbf{(5-4)}$$

where T_∞ is the air temperature inside the chamber and far from the heater (77 K), α is the thermal diffusivity or $\alpha = \frac{k_{air}}{\rho_{air}\cdot c_{p,air}}$, β is the coefficient of thermal expansion, and D_h is the diameter of the copper tube where the heater is located.

The very small Rayleigh number is the result of the high vacuum around the loop. At high vacuums where the number of air molecules is significantly reduced, the effect of natural convection is expected to be insignificant or even negligible, instead the conduction and radiation are considered to be responsible for most of the heat transfer. The thermal conductivity of air at 81 K is approximately 0.00814 (ASHRAE Handbook 2001).

5.1.3.2. Radiative Heat Loss

The flow loop is located inside a vacuum chamber which itself is submerged in LN_2; therefore, the temperature difference between the heater surface and the loop's

surrounding (LN_2) hardly exceeds a few degrees, and therefore the amount of heat loss due to radiation can be safely considered negligible.

5.1.3.3. Conductive Heat Loss

The most significant heat loss is the conductive loss through SS tube walls. The amount of heat that is actually transferred to the flow and reaches thermocouples is therefore $\dot{Q} = \dot{Q}_{heater} - \dot{Q}_{loss}$ where $\dot{Q}_{loss}$ accounts mainly for the conductive losses.

5.1.3.4. Assumptions and Boundary Conditions

Working environment:

- Working liquid: LN_2
- Liquid nitrogen boiling temperature at 200 kPa = 84 K
- Ambient temperature = 77 K
- Heater input: 0.02 to 0.16 W (or 100-800 W/m^2)
- Flow direction: TC1 to TC2

Dimensions:

- Stainless steel tube ID = 0.105" (2.67 mm)
- Stainless steel tube OD = 0.125" (3.175 mm)
- Distance from the center of the heater to TC1 = 93 mm
- Distance from the center of the heater to TC2 = 78 mm
- Heater width = 10 mm
- Copper tube OD = 0.25" (6.35 mm)

Numerical model:

- Software: FEMLAB 3.0a, conduction and convection module

- Geometry: axisymmetric (2D)
- Coupling: a fully-developed pipe flow with parabolic profile was used

$$v_z = \frac{2\dot{V}}{\pi R^4}\left(R^2 - r^2\right)$$

where v_z is longitudinal velocity, $\dot{V}$ is flow rate, R is the pipe inner radius, and r is the radial dimension of the pipe.

Model boundary conditions:

- Heat generated by the heater: $\dot{Q}_{heater}$
- Conductive heat loss term applied at the heater and all external walls as shown in Figure 5-6.
- Upstream temperature far away from the heater: T_∞

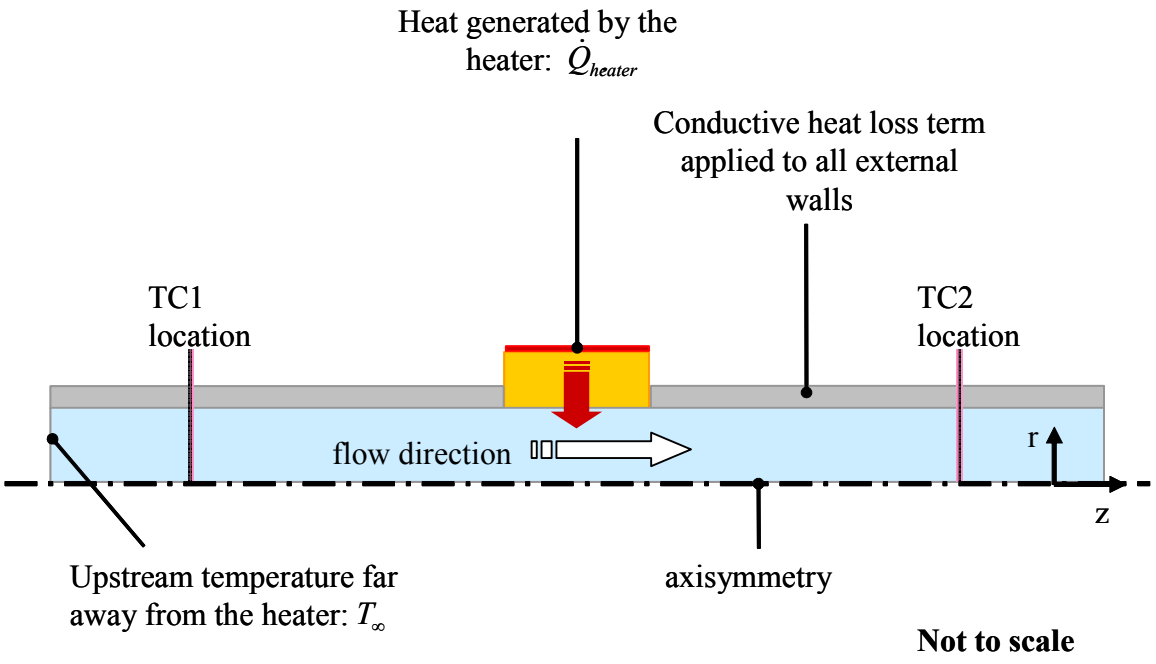

Figure 5-6 Schematic diagram of the heater, up- and downstream thermocouples in the flow loop

Material properties:

- Stainless steel tube : SS 4340 Industry standard properties
- Copper tube: c_p = 385 J/kg.K; k = 400 W/m.K; ρ = 8700 kg/m^3
- LN_2: physical properties from ASHRAE handbook

Mesh:

- Solution was found independent from the mesh.
- Model had 79500 elements which yielded 165000 degrees of freedom.

5.1.3.5. Numerical Results-Calibration Curve

This numerical simulation took into account the effects of heat dissipation to the environment, heat conduction through the tube wall, positions of the thermocouple probes with respect to the heater, and the effects of the temperature profiles at upstream and downstream locations. As mentioned before, the goal was to find a calibration curve that related the calculated flow rate, $\dot{V}_c$, to the actual flow rate, $\dot{V}_a$ (Equations (5-1) and (5-2)). The challenge was to accurately estimate the readings of TC1 and TC2 from the simulation results in order to accurately determine ΔT_m and the flow rate of liquid nitrogen.

In the real test setup, the thermocouple's tip was positioned inside a casing made from a piece of stainless steel tube with 1/16" OD. The tube was soldered closed at one end, which was inserted into the flow channel and was in touch with the liquid flow at the center of the channel (Figure 5-3). The numerical model however did not reflect the complicated geometry of this insertion. Instead, temperature profiles across the channel at TC1 (upstream) and TC2 (downstream) locations were calculated after some heat was applied to the system and a steady state condition was reached (Figure 4-4). Post-

processing was performed on the data to make it represent the actual system characteristics. It was assumed that there was no conduction heat transfer from the flow to the thermocouple's cover. In addition, since the thermocouple's tip was inside a casing of 1/16" OD, which was one half of the channel's diameter, it was assumed that the thermocouple's reading reflected the bulk temperature of the channel as liquid circulation around the probe would make the reading close to the bulk temperature.

From the numerical modeling results, it was found that as heat was added to the system for a wide range of flow rates as low as 0.5 ml/min, TC1 (upstream) temperature remained at 77 K and was uniform across the tube at this location (±0.003 K for 0.08 W heat energy), so it was safe to assume a constant TC1 of 77K. In addition, the results showed that the current position of TC1 was appropriate for the real-time tests.

Temperature profile at downstream (TC2) was a lot more complicated. Our results showed that there was a significant deviation between maximum and minimum temperatures across the channel even at high flow rates. Figure 5-7 illustrates the downstream temperature along the centerline of the flow loop at two different flow rates. The results (Figure 5-7) showed that a thermally fully developed region would not be reached until further downstream, so the temperature difference (downstream minus upstream) would not accurately estimate the flow rate of liquid nitrogen if not corrected. This effect could be minimized if the downstream thermocouple were moved further downstream from the heater, but the loop also had to be designed to minimize flow resistance and parasitic heat losses. Therefore a downstream length of 78 mm from the heater was selected.

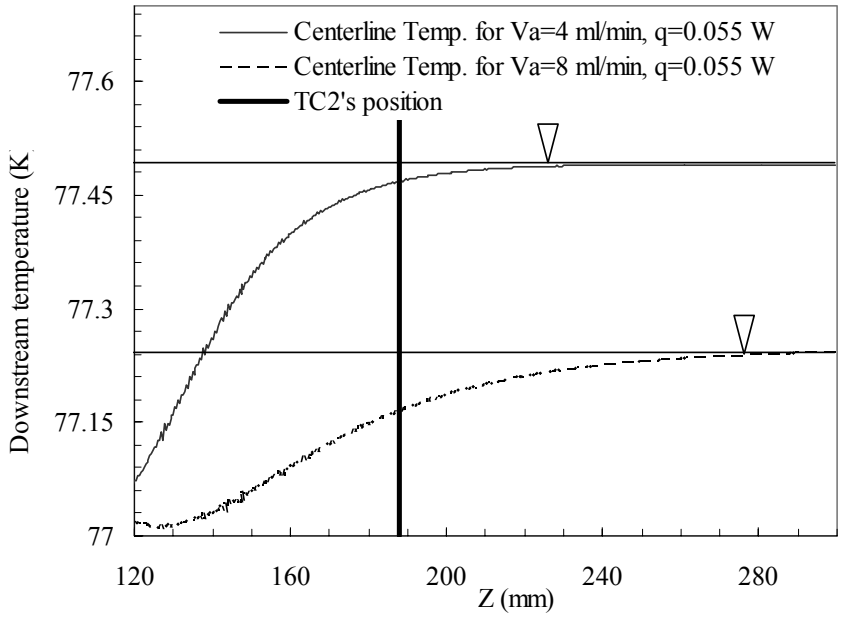

Figure 5-7 Schematic diagram of the heater section and the TC2 temperature reading

To account for the undeveloped temperature profile at the TC2 position and the dimension of the thermocouple's casing, the bulk temperature of the channel at TC2 was calculated. It was then used to calculate ΔT_m, to determine the measured flow rate from equation (5-2), and to obtain the calibration curve. The calibration curve (Figure 5-8) relates the actual flow rate generated by the micropump to the calculated flow rate, which is higher than the actual value. As mentioned before, tests conducted under vacuum at the ambient condition with water were used to validate the numerical calibration curve.

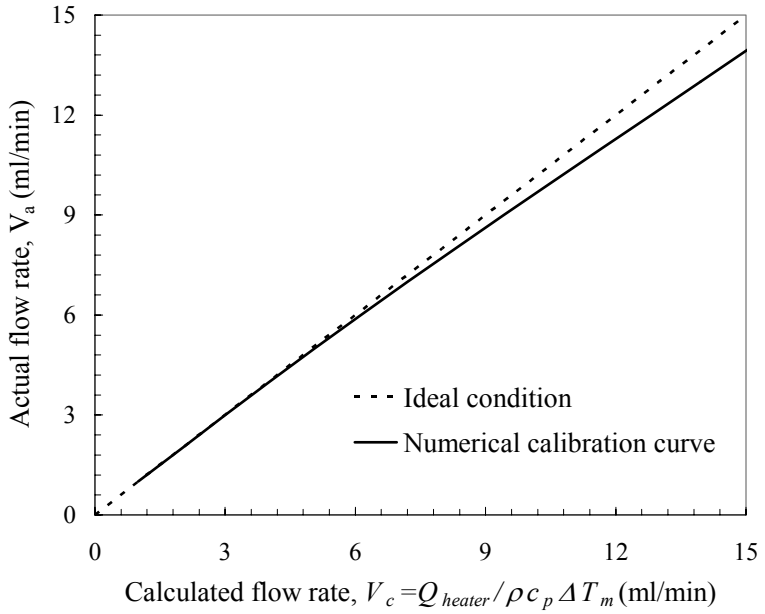

Figure 5-8 Calibration curve for the energy balance flow measurement technique

Therefore, for every $\dot{Q}_{heater}$ that was added to the system, a ΔT_m was measured. Then, $\dot{V}_c$ was calculated using Equations (5-1) and was related to the actual flow rate, $\dot{V}_a$, using the above calibration curve.

5.1.4. Pressure Drop-Flow Rate Relationship

As pointed out earlier, with the current test setup, only the liquid nitrogen flow rate could be measured. The generated pressure head of the micropump, which is an essential factor in evaluating the micropump, could not be measured by any pressure transducer due to the huge fluctuations in the reading. Therefore, a relationship between flow rate and pressure drop of the flow loop was found using a calibrated pressure transducer and a gas flow meter.

Since LN_2 evaporates quickly in ambient condition, the tests were carried out with air at ambient condition. An air flow was connected to the inlet of the flow loop. The air

pressure drop through the loop was measured by a calibrated pressure transducer for the flow rate range of interest. The result was then converted to that of LN_2 using equation (5-5). This equation was found using a pressure drop-flow rate relationship for an incompressible laminar flow inside a pipe. For same channel geometry and fixed pressure drop, flow rates of two fluids related to each other as the inverse ratio of their viscosities, shown in equation (5-5).

$$\dot{V}_{LN_2} = \frac{\eta_{air}}{\eta_{LN_2}} \cdot \dot{V}_{air} \qquad \textbf{(5-5)}$$

The air flow rate was measured accurately by a shielded gas flow meter. The gas flow meter was a GF-2060 made by Gilmont Instruments. Its flow range is 0- 80 ml/min, and its accuracy is ± 25% or ± 1 scale division (whichever is greater). Experimental data displayed high repeatability for several runs and a linear relationship at very low flow rates (<20 ml/min). Uncertainty of the measurements was determined to be 0.8 Pa for pressure and 0.1 ml/min for flow rate measurements.

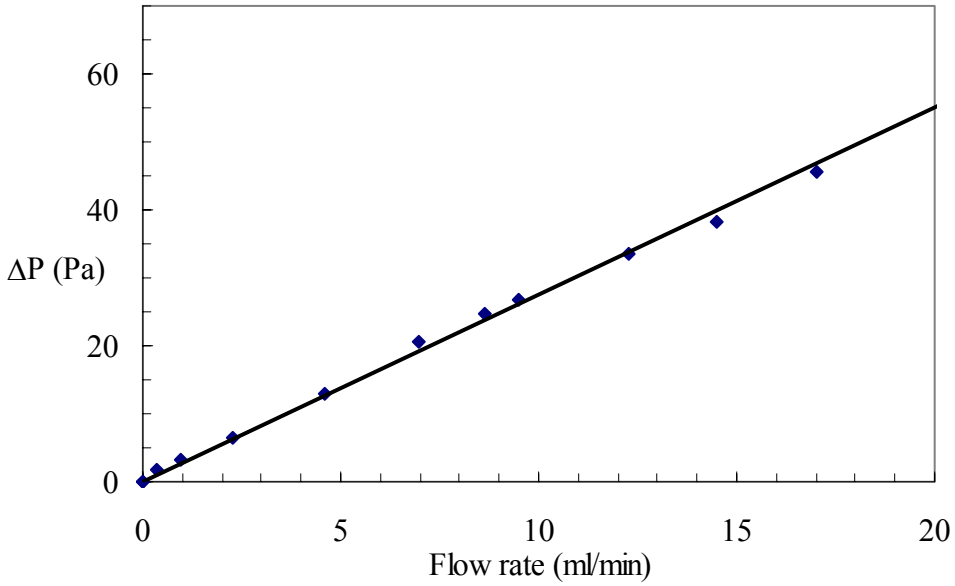

Figure 5-9 LN_2 pressure drop-flow rate relationship for the flow loop

Figure 5-9 presents the calibration curve, which relates the flow rate to pressure drop in the loop. It allows us to estimate the pressure head of the micropump by knowing the generated flow rate.

5.1.5. Challenges

Some of the challenges of the current test rig, designed for flow-rate measurement, are associated with the complexity of the test preparation procedure and susceptibility of the system to leakage. Therefore, a simplified test rig was designed and built for pressure head measurement purposes (shown in Figure 5-10). In the new test rig, the vacuum chamber was eliminated, and instead, a DP cell was installed to measure the static pressure head directly. Also, since creating a leak-proof system is always a major challenge in cryogenic tests, the simpler test rig, which eliminates many possible leak sources, saved us considerable time during the test-preparation process.

5.2. Pressure Measurement Test Setup

The experimental test rig shown in Figure 5-10 consisted of a liquid nitrogen Dewar flask, an external nitrogen gas tank (not shown in the Figure), the micropump, a differential pressure transducer (Validyne DP-15, range: 0 - 866 Pa, accuracy: ±0.1 Pa), a liquid nitrogen reservoir, and stainless steel tubing with an outer diameter of 3.17 mm and a wall thickness of 0.25 mm.

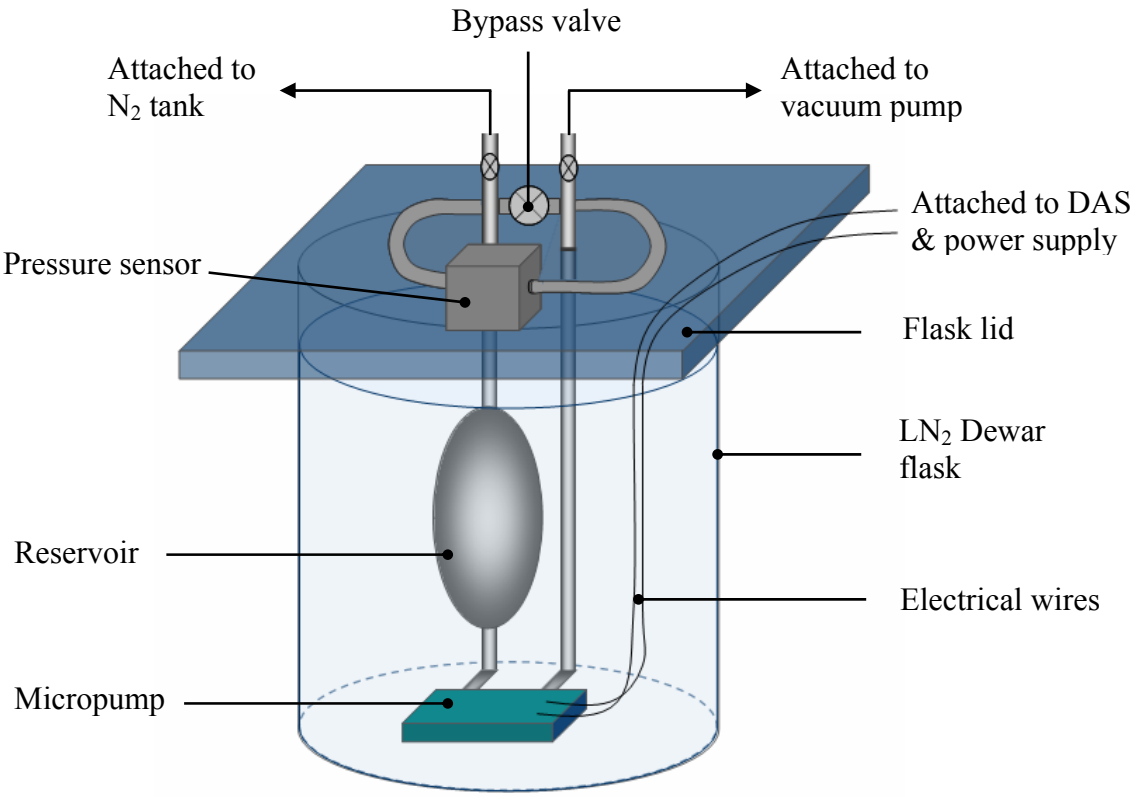

Figure 5-10 Schematic diagram of the liquid nitrogen test facility

The Dewar flask had an inner diameter of 150 mm to enclose the test loop properly. A few temperature sensors were installed inside the Dewar flask to allow monitoring of the temperatures at different locations. A foam lid was used to isolate the

interior space of the Dewar flask from the outside environment. Figure 5-11 shows a photograph of the test loop for static pressure head measurement. To minimize leakage, only welded joints and compression fittings were used to join sections of the loop together.

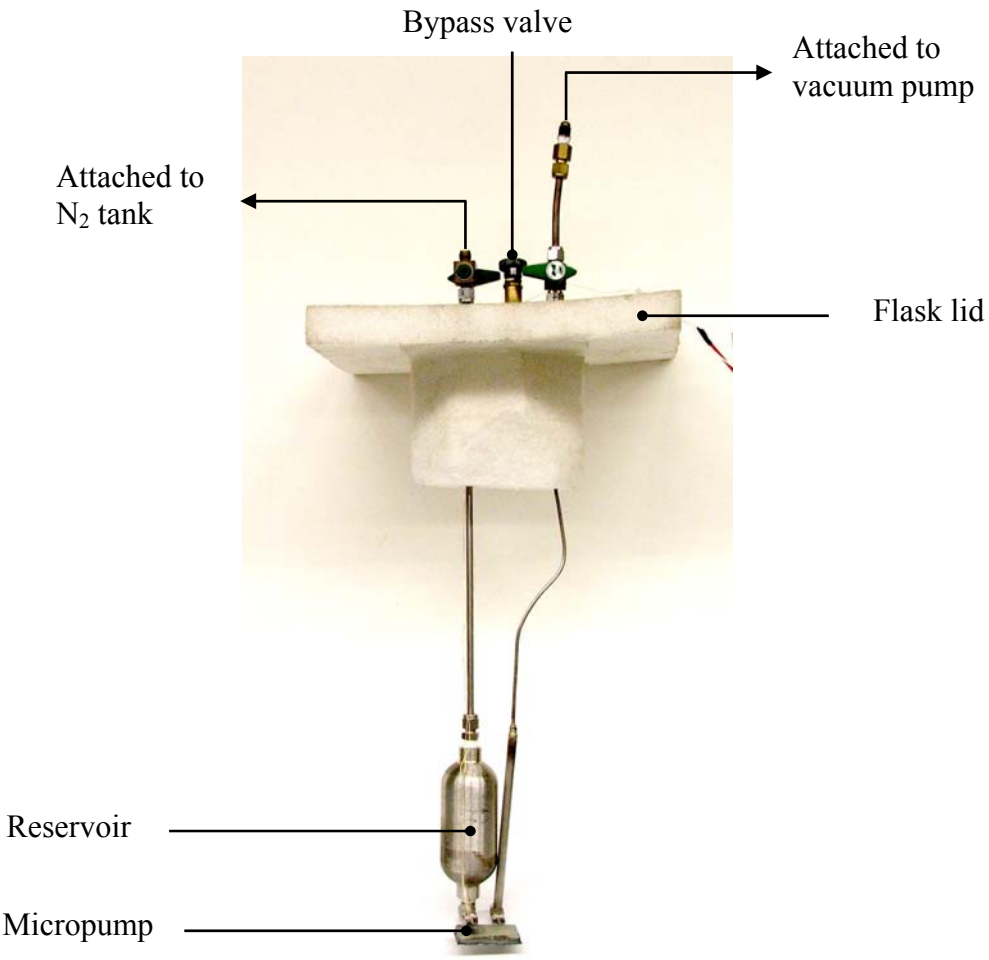

Figure 5-11 Photograph of the test loop developed for static pressure measurement

To prepare the test rig for the experiments, the system initially underwent a high vacuum (about 40 millitorr) and was then completely submerged in liquid nitrogen at 77 K. The submerging process included all the components that were in the Dewar flask, except the pressure transducer, which was positioned at a higher elevation outside the

flask. The external nitrogen gas tank was then used to feed ultra pure (99.998%) nitrogen gas into the test loop. The liquid nitrogen reservoir acted as a nitrogen-gas container for liquefaction purposes. The liquid nitrogen then flowed from the reservoir into the test loop and filled it.

After the system was fully charged with liquid nitrogen, helium gas at a gauge pressure of about 120 kPa was added to keep the LN_2 subcooled during tests and to prevent the forming of micro-bubbles (the boiling temperature of helium at a gauge pressure of 120 kPa is 5.2 K). During the experiment, the electric power consumption in the pump usually created a local temperature increase in the system, which could lead to micro-bubble formation and partial discharge (PD). According to Krahenbuhl et al. (1994), pressurizing the system greatly reduces the PD intensity and raises the inception stress. Since our experiments were run in a closed, well-vacuumed system, the possibility of oxygen solubility in LN_2 was greatly reduced. The oxygen boiling point at a gauge pressure of 120 kPa is 98.3 K, much higher than that of LN_2 (i.e. 84.5 K at 120 kPa gauge pressure), making it easily condensable into LN_2. In addition, oxygen is a highly reactive substance and can lead to significantly inaccurate measurements.

After the test rig was stabilized, the bypass valve was closed and tests were performed by applying DC voltage with positive (or negative) polarity at different increments to the micropump. The pressure head of the micropump was measured directly by the differential pressure cell, and the generated electric current was measured by an external electric resistant circuit and a data acquisition system (DAS).

5.2.1. Differential Pressure Transducer Calibration Curve

The pressure transducer was a variable reluctance sensor. It consisted of a magnetically-permeable stainless steel diaphragm clamped between two blocks of stainless steel. An inductance coil was embedded in each block. When a differential pressure was applied to the transducer, the diaphragm deflected toward the cavity with the lower pressure (decreasing one gap and increasing the other one), and changed the magnetic reluctance. A carrier demodulator (Validyne CD-280) was used with the pressure sensor. The carrier demodulator provided the required AC excitation, received the AC signal from the sensor, and converted it to a useful DC signal, which was recorded by a DAS.

The pressure transducer was calibrated using a manometer and another factory-calibrated transducer. Results shown in Figure 5-12 indicate high linearity and repeatability. Before every single test, the zero offset was corrected. The offset usually varied over time because of ambient temperature fluctuation, humidity, and mechanical stresses from previous operating conditions.

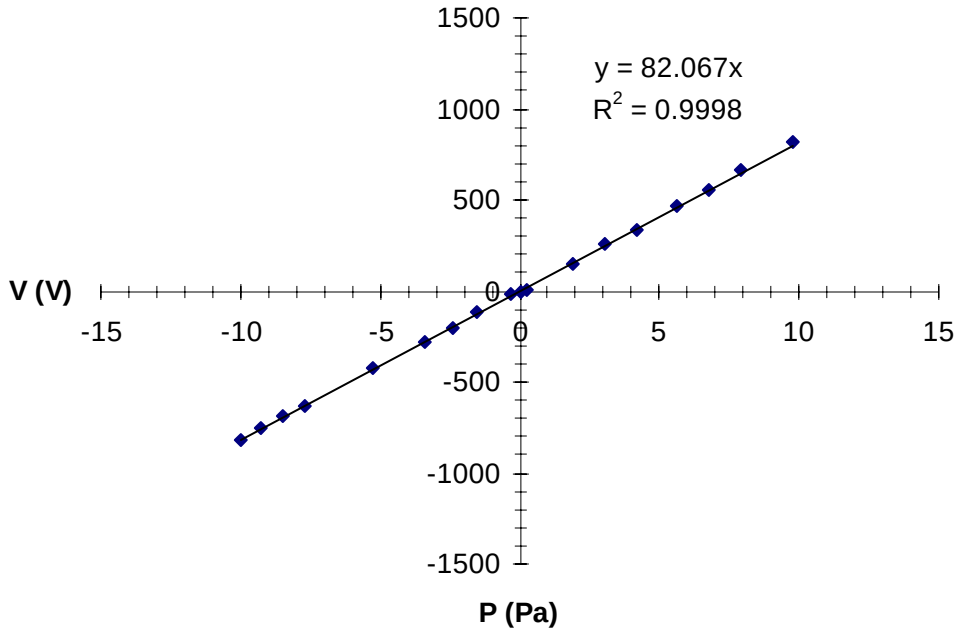

Figure 5-12 Pressure transducer (Validyne DP-15) calibration curve.

5.2.2. Electric Current Measurement

Results of preliminary experiments showed that the generated electric current that was created by the migration of ions from one electrode to another during the pressure generation process was in the order of a few hundred nA and could not be measured by common data acquisition systems. Therefore, an electric circuit was designed and added to the main circuit to measure the current, as shown in Figure 5-13.

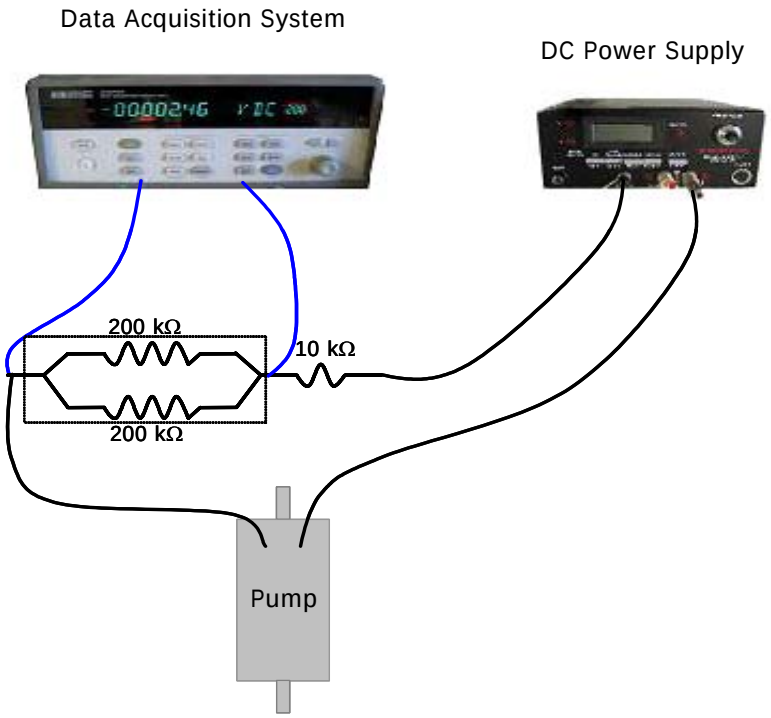

Figure 5-13 Schematic drawing of the current measurement circuit

The smaller resistance in the circuit (10 kΩ resistance) was only for protection purposes. It was used to reduce the high current and help prevent the DAS from getting damaged in case of an electrical short circuit (i.e. if the pump were to burn up). For every test, the electric potential difference across the circuit board was measured and then, was converted to current by dividing it by the total resistance.

5.3. Summary

This chapter introduced the two test rigs, which were designed and built for different measurement purposes, and explained the principle behind their operation. Experiments were performed by applying DC voltages to the micropumps while generated current and pressure were measured.

CHAPTER 6: RESULTS AND ANALYSIS

The micropumps were installed and tested in two different test rigs. One test rig was specially designed for flow-rate measurement and the other for static pressure head (hereon also referred to as pressure head or static head) measurement purposes. Therefore, the experimental results are presented in two sections, flow rate and static pressure head results. The test rig characteristics and test preparation procedures are explained in detail in Chapter 5.

The tests were started by applying DC electric potential difference to the pump electrodes. The generated flow rate and current values were collected every 5 seconds using a data acquisition system. To reduce the data at each voltage increment, the time average of pressure and current was taken and then plotted vs. the applied voltage.

6.1. Summary of Micropump Designs

In this study, four micropump designs were chosen to investigate the effect of various design parameters such as electrode shape geometry, electrode gaps, channel height, electrode material, and working liquid on the micropump performance. Each design had one or two parameters changed compared to one another. The designs included different emitter shapes: planar, saw-tooth; inter-electrode spacing (D_{el}): 20 and 50 μm; electrode-pair spacing (D_{pel}): 80, 100, and 200 μm; and channel height (H_{ch}): 130 and 260 μm. For each design, at least 5 prototypes were tested to validate repeatability of the results. Table 6-1 shows a list of the micropumps that were tested at different DC voltages ranging from 0 to 2.5 kV.

Table 6-1 Different designs of micropump

Design	D_{el}(μm)	D_{pel}(μm)	Emitter shape	Number of stages
(50,100,f)	50	100, $2D_{el}$	f	79
(50,100,s)	50	100, 2 D_{el}	s	74
(50,200,s)	50	200, 4 D_{el}	s	54
(20, 80, s)	20	80, 4 D_{el}	s	90

- f & s: electrode shapes (flat & saw-tooth)
- D_{el}: emitter-collector inter-electrode spacing
- D_{pel}: electrode-pair (stage) spacing
- H_{ch}: channel height (130 and 260 μm)

The micropumps had successfully passed dozens of thermal-cycling tests between ambient temperature and the liquid nitrogen environment with an internal pressure of 500 kPa before actually being tested.

6.2. Static Pressure Head Measurement Results

6.2.1. Testing Procedure and Data Reduction

The tests were started by applying DC electric potential difference to the micropump. The generated static pressure head and electric current were measured and recorded using a DAS. The experimental results which will be presented in this chapter were all taken with positive voltage polarity unless otherwise stated.

Figure 6-1 shows a sample data taken with a (50, 100, s) design with H_{ch} = 260 μm. The (50, 100, s) corresponds to D_{el} = 50 μm, and D_{pel} = 100 μm, saw-tooth emitter and planar (flat) collectors. The static pressure head and generated electric current

(caused by the migration of ions from one electrode to another) are plotted versus time. The positive voltage polarity was applied to the emitter electrodes, and the collector electrodes were grounded. The voltage increased slowly from 0 until the pumping onset occurred at around 1000 V. From then on, the voltage was increased in increments of 100 V until it reached 1600 V. To avoid the possibility of an electrical breakdown, the voltage was not increased further. After a few minutes, the voltage was decrementally decreased until it reached zero.

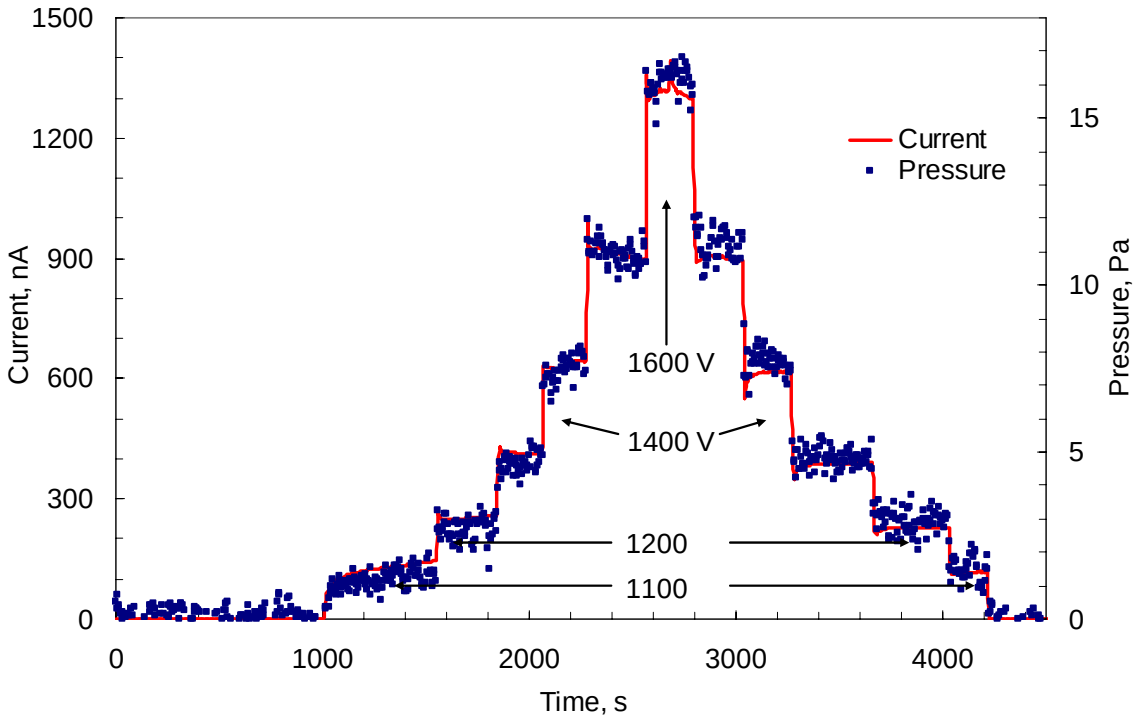

Figure 6-1 Experimental results of a (50,100,s) design (sample #1). (+) voltage polarity (0 – 1600 V) was applied to the emitter while the collector was grounded.

The data set shown above was reduced by taking the time average of pressure and current data points at each voltage increment and plotting them versus the applied voltage, as shown in Figure 6-2.

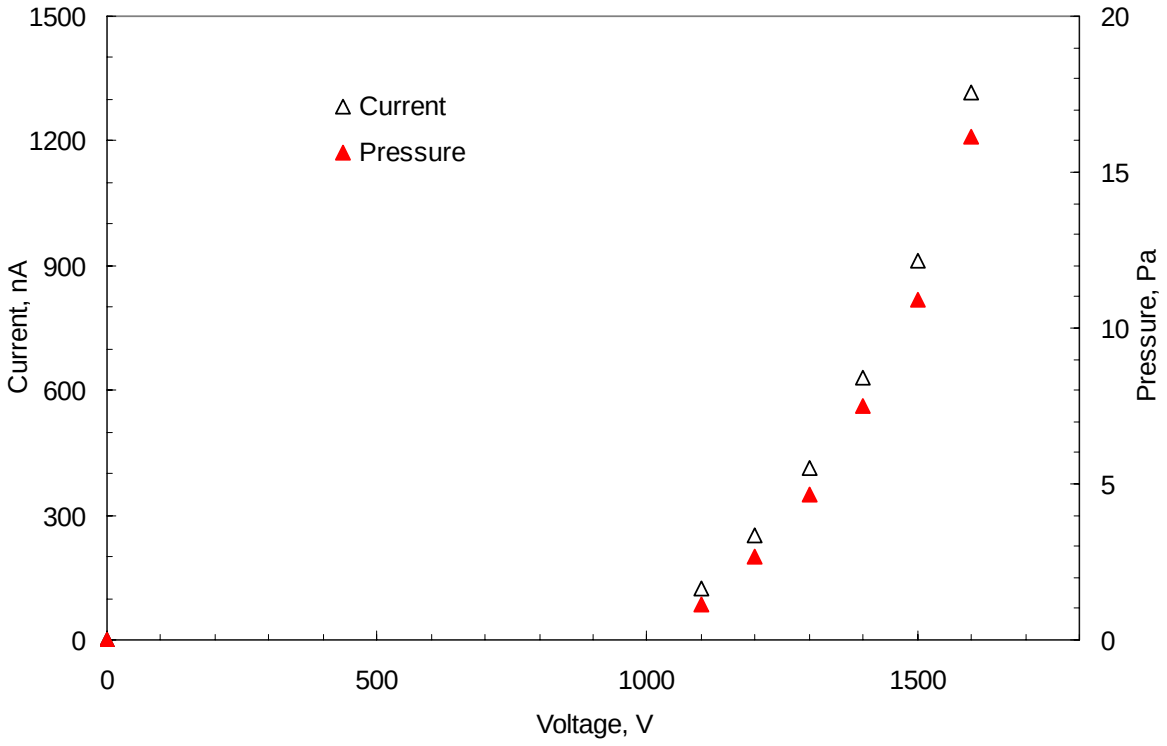

Figure 6-2 Time-averaged static pressure head and current vs. applied voltage for sample #1

As seen in the figure above, the onset voltage of pressure head and current for this design is around 1000 V. In the next section, more investigation on the onset voltage is presented. In addition to the P-V and I-V relationships, the pressure-current (P-I) relationship is also investigated later in this chapter.

6.2.2. Onset Voltage

One of the determining factors in selecting the proper design is the onset voltage. As with most microelectromechanical devices, the trend is to lower the electricity consumption of these devices to make them compatible with microelectronic devices and

to save electricity. Therefore, it is necessary to have a clear estimation of onset voltages for each micropump design.

Onset voltage could not be calculated theoretically due to the complexity of the EHD nature; therefore, a mathematical approach was used to estimate its value from experimental data for every single design. For that, the equation of the line which connected the first 2 data points in P-V and P-I curves for every test was determined and then the line intersection with the voltage axis was calculated and defined as the onset.

The onset voltages of pressure and current were calculated separately and compared for every design as shown in Figure 6-3 and Figure 6-4. The mean values of pressure and current onset voltages were expected to be identical, which was confirmed by the results. However, the uncertainty involved with the current was less than that of the pressure. This could be mainly due to measurement errors. The measurement error of the current was ±1 nA, and the measurement error of the pressure was ±0.5 Pa.

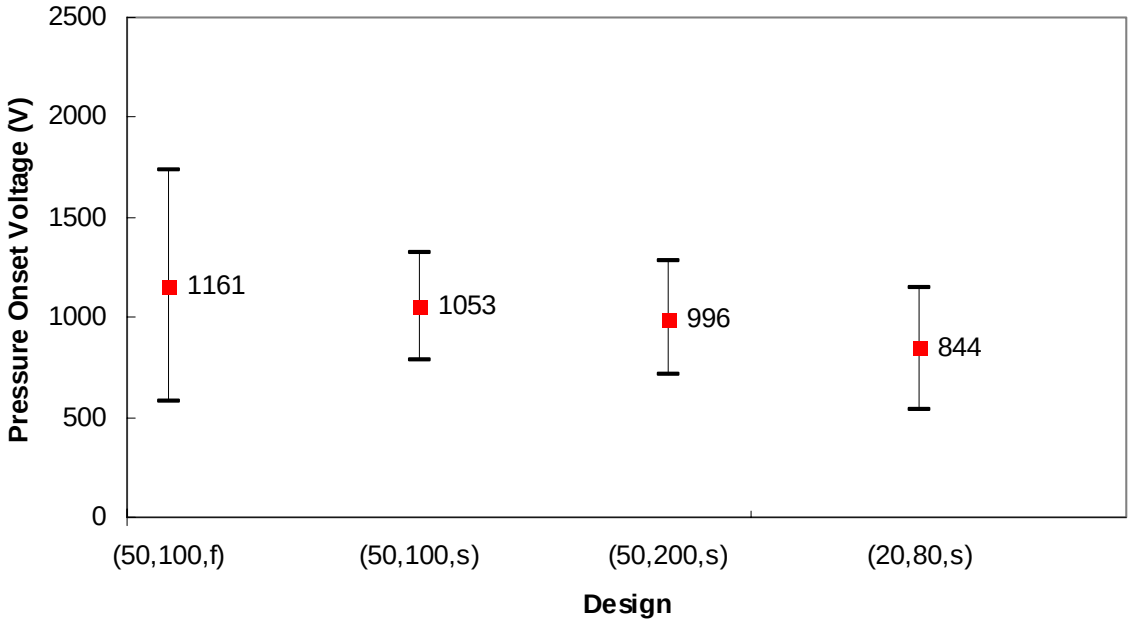

Figure 6-3 Onset voltage of pressure for various designs

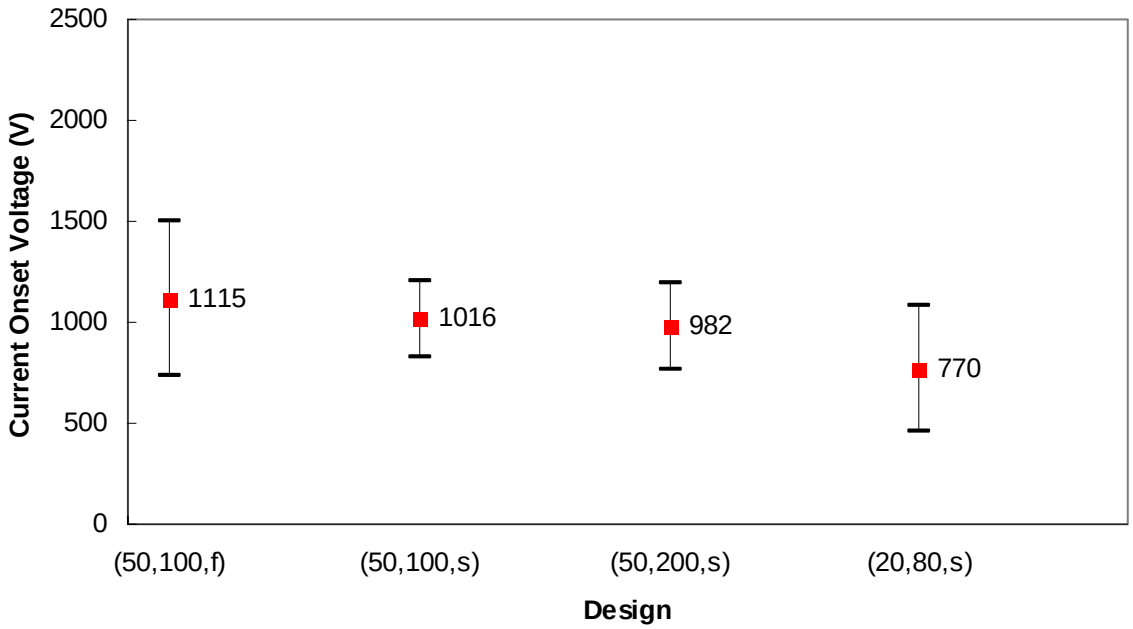

Figure 6-4 Onset voltage of current for various designs

6.2.2.1. Hysteresis

As mentioned before, for every single test, the voltage was first increased from the onset to a maximum value and later decreased from the maximum value to the offset transition. It was expected that the onset and offset values would be very close when the voltage was being increased or decreased, as shown in Figure 6-1; however, it was observed in many cases that the offset voltage was slightly less than that of the onset in one run. This hysteresis effect may be attributed to the energy barrier at the electrode/liquid interface, which should be overcome at a higher onset value. Once it was overcome on the way toward higher voltages, less energy (i.e. voltage) was required to keep the same amount of pressure when moving toward lower voltages. Overall, the results show very little hysterisis when the voltage was being increased or decreased;

therefore, the data of the voltage increasing and decreasing scenarios were pooled together, averaged and plotted for further processing.

6.2.2.2. Effect of Electrode Shape

As seen in Figure 6-3 and Figure 6-4, a comparison of the results of the (50,100,f) and (50,100,s) designs shows that the onset value of the saw-tooth shape emitter was at least 100 V less than that of the flat shape emitter. This phenomenon can be explained by the difference in their electrode geometries, which affect the local electric field and therefore the onset value. The electric field was constant between two flat electrodes, as was the case in (50,100,f). However, at the edge of the saw-tooth shaped emitters where the curvature was very small, the local electric field intensity became extremely high. This could eventually result in a lower onset value compared to that of the flat electrode case.

Also, these results indicate that the uncertainty of onset measurement for the (50,100,f) design is much higher. The primary reason for this might be the accuracy of the onset measurement. The onset measurement is affected by the slope of the P-V (or I-V) curve. In the case of (50,100,f), the pressure generation occurs very gradually, so it makes it difficult to define an exact onset value for this design. On the other hand, pressure generation with (50,100,s) occurs pretty rapidly at the onset voltage, which makes the P-V slope quite distinguishable, and therefore more accurate.

6.2.2.3. Effect of Electrode Spacing

The onset values are believed to be a function of the local electric field and the energy barrier at the metal/liquid interface. The energy barrier at the metal/liquid interface is a function of only the metal work function and liquid ionization energy, and is

therefore independent of electrode geometry and distance. The local electric field, on the other hand, is a function of the electrode geometry and the emitter-collector distance.

Similar onset values were obtained with the (50,100,s) and (50,200,s) designs. Both designs had identical emitter geometries (saw-tooth) and emitter-collector gaps (50 μm), which resulted in identical local electric fields at their emitter/LN_2 interfaces, and therefore created similar onset values. The results also prove that the electrode-pair distance does not affect the onset value.

Results of the (20,80,s) design shows an onset value 1.3 times lower than that of the (50,100,s) and (50,200,s). In all these designs, the emitter geometries were saw-tooth shaped. However the emitter- collector gap in the (20,80,s) was 2.5 times smaller than that of the (50,100,s) and (50,200,s). This indicates that lowering the gap between electrodes results in higher electric field between them, which can eventually initiate the pumping phenomenon at a lower voltage. It is worth noting that although the onset value was affected by the emitter-collector distance, it did not behave linearly with the ratio of the gaps.

6.2.2.4. Effect of Channel Height

To investigate the effect of channel height on the onset voltage, two identical micropumps of (50,100,s) design were tested with different channel heights: 130 and 260 μm. The results plotted in Figure 6-5 show that channel height had little effect on the onset voltage. This is because channel height does not have any impact on the local electric field, which, in turn, is one of the main factors affecting the onset value.

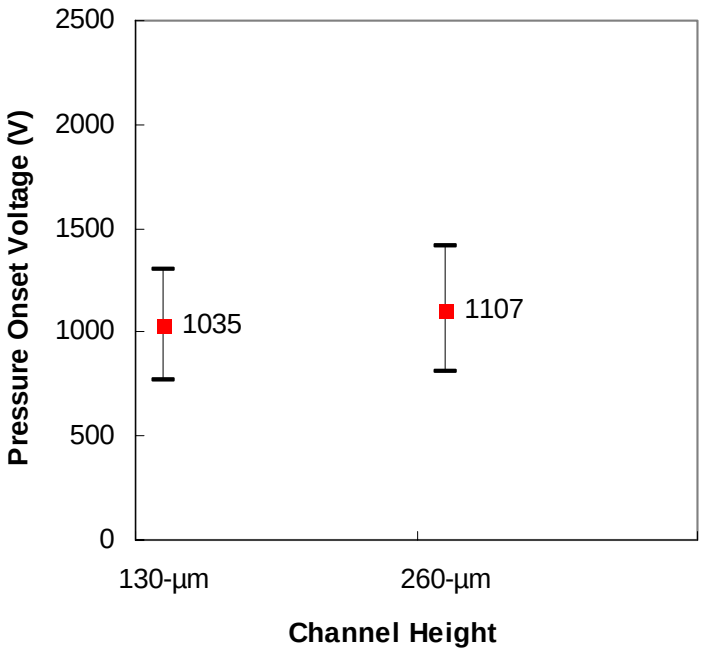

Figure 6-5 Pressure onset voltage for (50,100,s) design with different channel heights

6.2.2.5. Effect of Voltage Polarity

In most dielectric liquids, the onset voltage of the EHD pressure generation is lower with a certain polarity. That polarity can be either positive or negative, depending on the work function of the metal electrode and the ionization energy of the dielectric liquid. In Chapter 3, the work of Schmidt (1997) on the energy barriers for field-ionization (the primary ion generation process at the positive electrode) and field-emission (the primary ion or electron generation process at the negative electrode) phenomena at the metal electrode/liquid interface was discussed extensively. Schmidt indicated that for most non-polar liquids the energy barrier of field emission is less than that of field ionization, meaning that the pumping begins at a lower voltage if (-) polarity is applied. Following Schmidt's footsteps, a simple calculation was used to determine the energy barriers of field emission and field ionization at the gold/ LN_2 interface. The

theoretical results showed a slightly smaller field emission energy barrier than that of the field ionization. That was later confirmed when these micropumps tested with both (+) and (-) voltage polarities.

Figure 6-6 shows a set of experimental data taken with a (50,200,s) design (D_{el} = 50 μm, D_{pel} = 200 μm, saw-tooth emitter and flat collector) with H_{ch} = 260 μm. Both tests were performed at similar experimental conditions, including the same liquid. DC voltage within the range of 0 to 1600 V was applied to the emitter electrodes while the collector electrodes were grounded. The first test was performed with (-) polarity, followed by the second test with (+) polarity. As seen in the graph, pressure heads and currents generated with (+) were slightly higher than those with (-) polarity, but overall, the results indicated that the voltage polarity had little effect on the onset voltage at the Au/LN_2 interface.

There were also cases in which when the polarity was switched, initially no pressure head was generated. This was believed to be possibly due to an abundance of un-relaxed charges with opposite polarity already existing inside the liquid from previous tests.

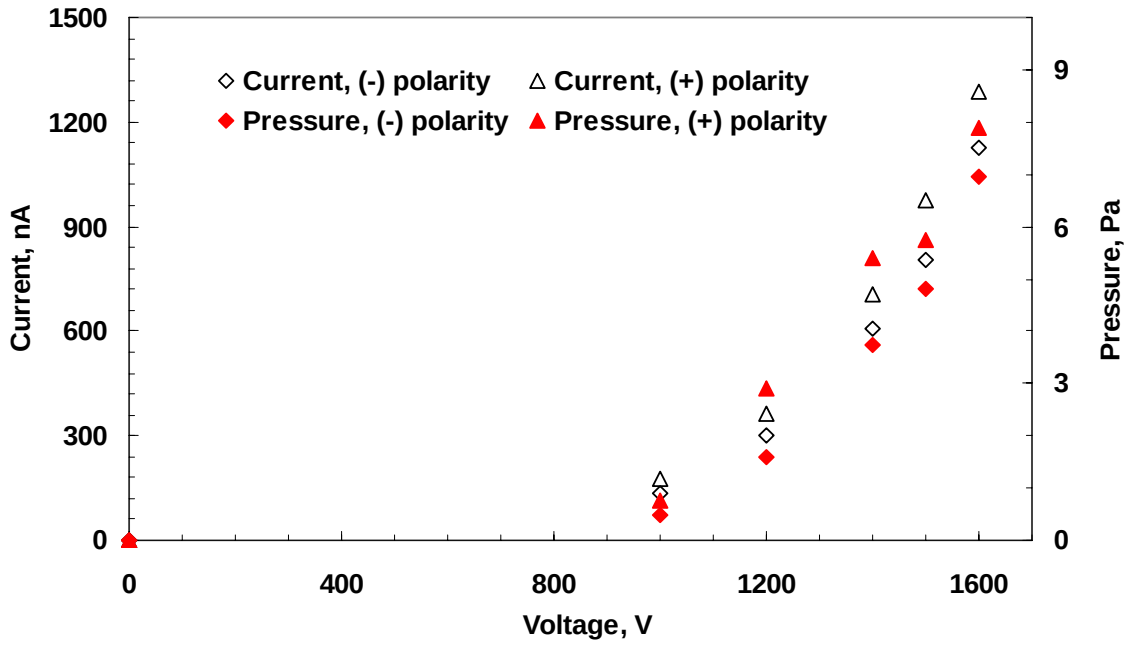

Figure 6-6 Effect of voltage polarity on pressure and current generation: a (50,200,s) design tested with (+) and (-) voltage polarities

DC voltage with positive polarity was used for most of the tests in this study, in part because scientists such as Krahenbuhl et al. (1994) have shown that the breakdown in LN_2 with (+) polarity is less aggressive than that with (-) polarity at the same voltage level.

6.2.3. P-V and I-V Characteristic Curves

It was shown at the beginning of this chapter (Figure 6-1) that the generated pressure and electric current relationships with voltage always resemble each other in the general trend. This clearly indicates that the ions creating the electric current are also responsible for the pressure generation, as well. This also demonstrates that the pressure head is accurately controllable with the applied voltage, which is another advantage of the EHD micropumps.

In this section, for the sake of simplicity, only the P-V relationship of various designs is analyzed. The experiment shown in Figure 6-1 was repeated 9 times. Time-averaged pressure head values are plotted versus applied voltage for all the tests in Figure 6-7.

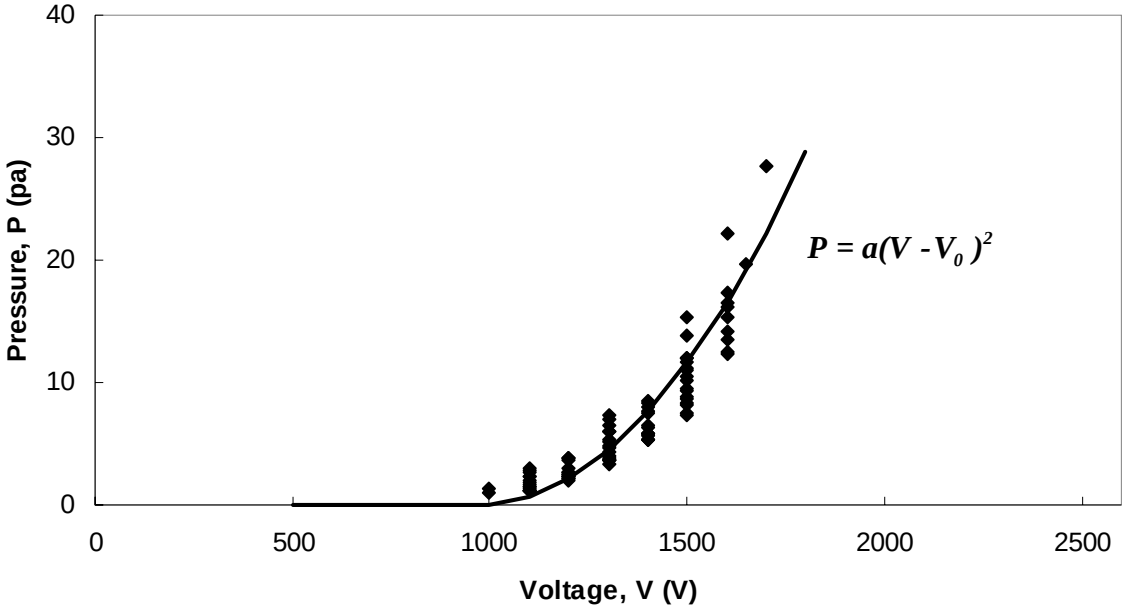

Figure 6-7 Pressure data points represent the result of 9 series of test run with a (50,100,s) design (sample #1). (+) voltage polarity was applied to the emitter (0 – 1700 V)

The best-fit line to the data, shown in the figure above, resembles a parabola. The equation of the line is a 2nd degree polynomial function, which is shown in Equation (6-1) as

$$P = a(V - V_0)^2 \tag{6-1}$$

where a is the leading coefficient of the equation and V_0 is the onset voltage.

Early experiments showed that the leading coefficient of the P-V line was unique for each design and accurately reflected the design characteristics. Therefore, to better

understand the effect of design parameters on micropump performance, the leading coefficient of Equation (6-1) with 70% confidence bound, corresponding to different designs, calculated based on their experimental data are compared in Figure 6-8. All the designs had the same channel height of 260 μm and were tested with (+) voltage polarity. More information on the effect of voltage polarity on pressure and current generation can be found in previous section and Figure 6-6.

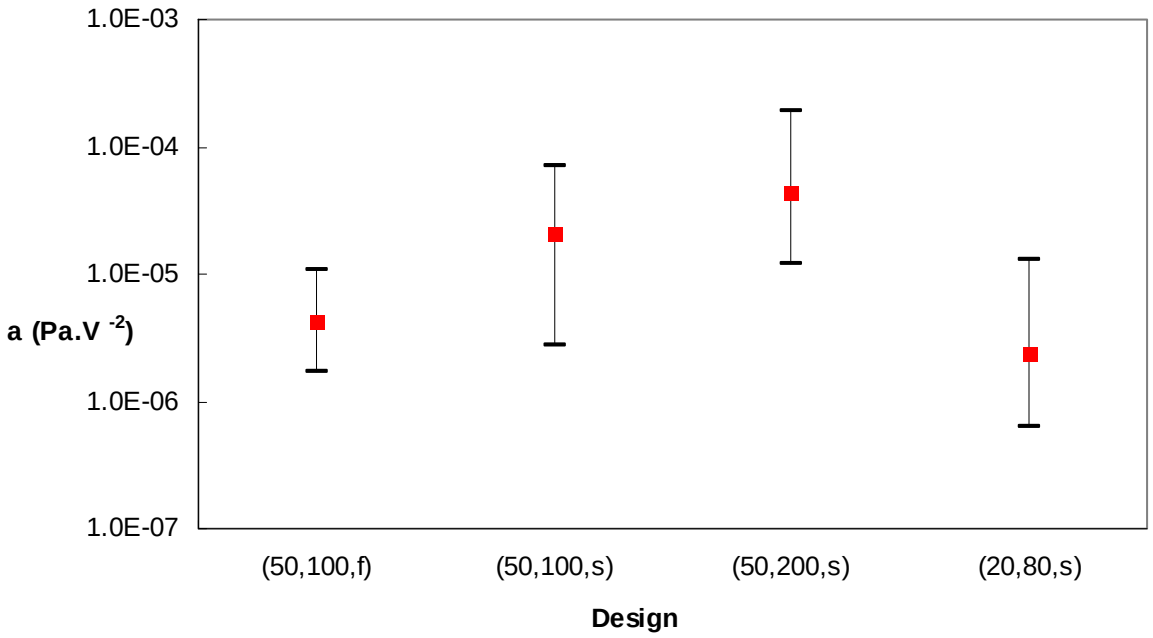

Figure 6-8 Parameter of P-V model of different designs tested with (+) voltage polarity applied to the emitters

The mean values of *a* plotted in the figure above indicate that at a given voltage, the maximum and minimum pressure heads were for the (50,200,s) and (20,80,s) designs, respectively.

To explain the differences seen in the *a* values, the following factors should be taken into consideration: the emitter shape, and the electrode spacing, which determines the number of pumping stages (i.e. the electrode pairs). The number of pumping stages is

reduced when inter-electrode and electrode-pair spacings are increased for a constant substrate length. That is, the (50,100,s) design had more pumping stages compared to a (50,200,s) design.

If two successive electrode pairs become too close, the interaction between their electric fields may result in generating backflow that would dramatically reduce the pressure head. This may explain why the generated pressure head by (50,200,s) surpassed the one obtained by (50,100,s). As in the latter, the effect of the opposite electric field between successive pairs was higher than that of the former because of closer spacing.

And finally, if emitter and collector become too close, the electric field intensity between them increases dramatically, which can lead to electric breakdown at lower voltages compared to other designs. That could explain why the least pressure head was generated by the (20,80,s) design, despite its having more pumping stages. More than 5 prototypes of the (20,80,s) design were tested, none of which tolerated voltages higher than 1800 V. This design was initially expected to generate the highest pressure head, but apparently, the effect of the electrodes being too close cancels out the benefit of having more pumping stages and lower onset voltage.

To analyze the effect of the emitter geometry on the performance, the results of (50,100,s) and (50,100,f) designs are compared next. Both designs had similar characteristics in every aspect except the emitter geometry. The former had saw-tooth shaped emitters, and the latter had flat shape emitters. Test results in Figure 6-9 show that incorporating saw-tooth shaped emitters generated a much higher pressure head at the same input voltage. As mentioned before, electrode geometry plays an important role

in creating ions at the emitter/liquid interface (Benetis 2005; Mirotvorsky and Stishkov 1996); therefore, a saw-tooth shaped emitter with stronger injection sites compared to flat shaped electrodes is expected to generate higher pressure heads.

Also, it is worth noticing that for the (50,100,f) design, the emitter and collector electrodes were alike in shape, and there was a high possibility of an ion-injection process taking place at both electrodes, thereby generating opposite polarity ions. The electric current represents the overall number of ions migrating from one electrode to another-not only the ions generated at the emitter/liquid interface but also those with opposite polarity generated at the collector/liquid interface. Pressure head, on the other hand, represents only the net number of migrating ions. As the positive and negative ions move in opposite directions, they cancel out each other's contribution to the pressure generation. This again could explain the relatively low pressure head and high current results from the (50,100,f) design.

6.2.4. P-I Characteristic Curve

As was shown earlier in Figure 6-1, the generated pressure head and electric current relationships with voltage always represented similar trends. As a result, the pressure-current (P-I) relationship was expected to be linear because pressure and current were both direct results of ion generation and transportation. To better analyze the result, time-averaged pressure values were plotted versus time-averaged current at every voltage for all the tests run with one prototype.

Figure 6-9 shows the P-I graph drawn for the same test results previously shown in Figure 6-3 and Figure 6-7 performed with a micropump of (50,100,s) design and H_{ch} = 260 μm. During those tests, all the experimental conditions were kept unchanged.

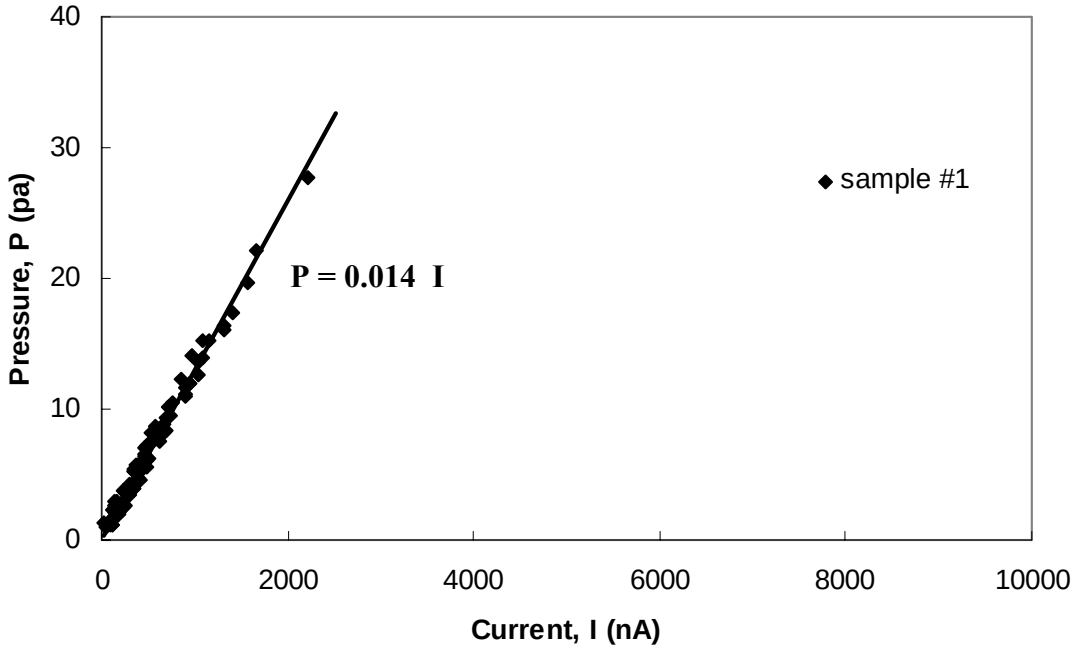

Figure 6-9 P-I characteristic of a (50,100,s) design (sample #1) with H_{ch}=260 μm. The slope is 0.014 Pa/nA.

Theses results support the idea that the P-I characteristic curve is indeed linear and that its slope remain unchanged for all the tests run with one sample, although it sometimes varied from one sample to another. Therefore, it is appropriate to say that for each micropump, the generated pressure head is a function of current as

$$P = m\,I \tag{6-2}$$

where m is the slope of the P-I line.

The slope of the P-I curve is believed to be affected by the following factors: ion mobility of the working liquid and geometrical parameters of the design such as electrode geometry, electrode thickness, electrode spacing, electrode length, and channel height.

To examine the effect of abovementioned parameters on the P-I relationship, 5 prototypes of the same design (50,100,s) were tested: 3 of them had 260-μm channel

height and 2 had 160-µm channel height. The slope of all the P-I curves are plotted in Figure 6-10 as $m \pm \sigma$, which covers 70% of the data points in each series of tests. As the graph shows, the slope mean value varied from one prototype to another. However, the average of mean values of #4 and #5, which had 130-µm channel height, was overall higher than that of samples #1, 2, 3 which had 260-µm channel height. This confirms Benetis's (2005) findings that at lower channel heights, higher static pressure heads can be achieved. However, such higher static pressure head is achieved at a cost of generating less flow rate due to increasing pressure drop inside the shallower channels.

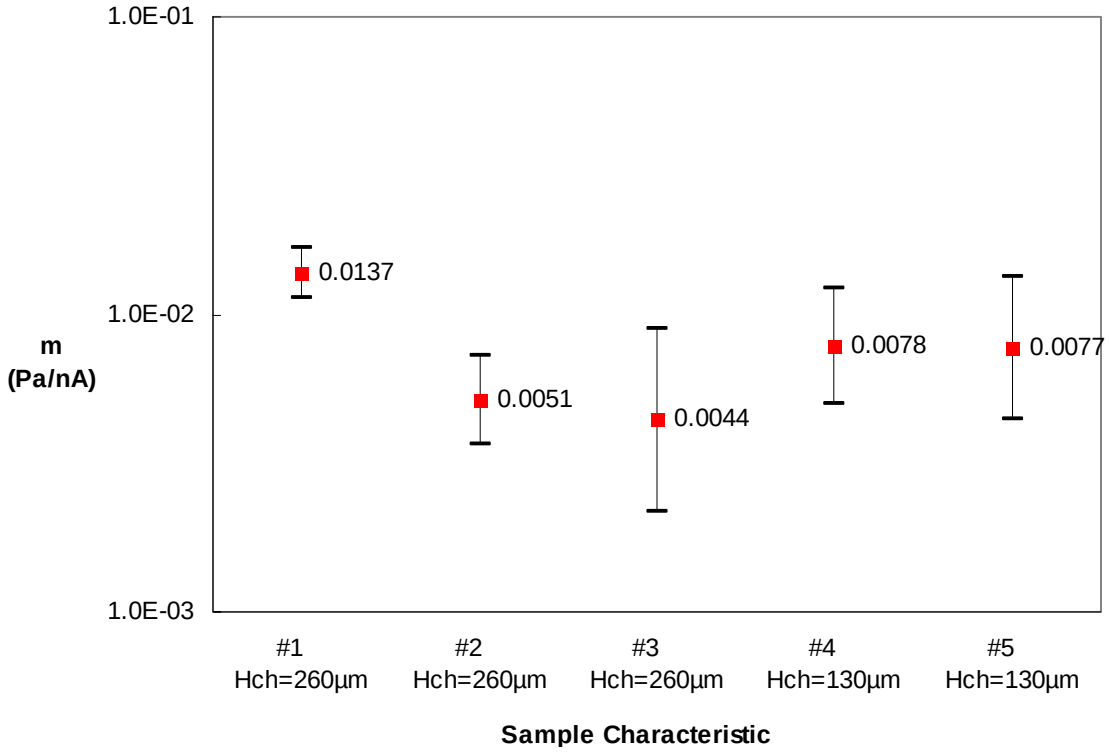

Figure 6-10 Slope of P-I characteristic curve of 5 prototypes of (50,100,s) design with H_{ch}=130 and 260 µm

6.2.4.1. Uncertainty Analysis-Effect of Microfabrication Accuracy and Working Liquid Purity

The sources of uncertainty seen in the m values are mainly due to impurity molecules in the working liquid and microscopic differences existing in the electrode structure. As discussed in Chapter 3, the ion mobility of a pure liquid is expected to remain constant at certain temperatures and test conditions. However, impurity molecules under high electric fields can dissociate and introduce a number of different types of ions into the system, thus changing the average mobility of liquid molecules and affecting electric current generation, which, in turn, changes the slope of the P-I line.

The impurity molecules may be from three sources: 1) those that might have existed in the working liquid, 2) those (i.e. oxygen) that entered the system from air during the liquid charging process, and 3) those that come from the oxide layer on the surface of the electrodes, which under high electric field are detached and dissolved in the liquid. The metal electrodes can be oxidized and degraded under high electric field because of the existing oxygen molecules that might have entered the system from air. Although visual inspection of the electrodes after the tests showed a very low level of degradation, that would still be enough to affect the P-I slope considerably.

Comparing the m values of the first three samples, which have similar designs, it is clear that a certain level of inconsistency exists among them. The main reason for this behavior in identical designs is probably the microscopic variation of the electrodes' geometrical parameters such as thickness, spacing, and the angle of the saw-tooth points. These variations are direct results of the accuracy of the microfabrication process. As mentioned before, the micropump substrates were microfabricated manually at the

facilities on campus. It is believed that by batch-fabricating electrodes, the level of inconsistency could be significantly lowered and therefore, the data of similar design prototypes would look more similar.

6.2.4.2. Effect of Electrode Design

To analyze the effect of electrode design parameters such as emitter shape, emitter-collector spacing, and electrode-pair spacing, the slope of P-I linear model for all 4 designs are plotted in Figure 6-11.

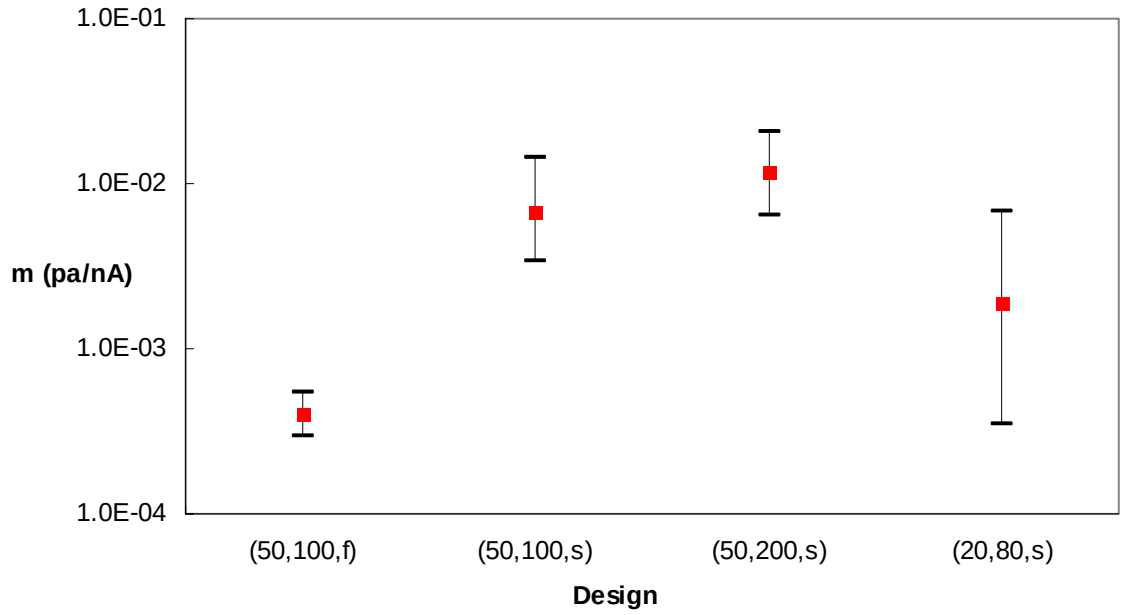

Figure 6-11 Slope of P-I linear model for various designs

Comparing the *m* values of all designs, it is clear that at a certain current, prototypes of (50,200,s) design generated the highest pressure head, while prototypes of (50,100,f) design did the lowest.

The lowest value of (50,100,f) is because it only has flat electrodes, which, compared to other designs with saw-tooth shaped emitters, lack a lot of ion generation sites.

Going from (50,100,s) to (50,200,s), it is obvious that the distance between neighboring emitter-collector pairs is doubled. This decreases the effect of unwanted electric field in the opposite direction, which is responsible for the so-called back flow generation. On the other hand, a reduction in number of electrode pairs causes a negative effect on pressure generation. But, overall the effect of doubling the electrode-pair distance seems to have surpassed the reduction in the number of pairs.

6.2.5. Uncertainty Analysis-Micropump Life Cycle

On many occasions, after running consecutive tests on many micropumps, three repetitive operation stages have been recognized: the initial, the intermediate, and the final stages. During the initial operating stage (i.e. the burn-in period), when the pump was being tested for the first few times, the micropump performance was random, inconsistent, and hardly repeatable. As testing on the pump continued, the performance became more repeatable after a long time, often exceeding 10 hours of operation. The final stage set in as degradation in the pressure head and the measured current were observed. Keeping the pressure head as high as its previous level required increased voltage. In other words, in the final stage, the coefficient of the P-V characteristic curve decreases and the pumping onset voltage moves to higher levels.

6.2.5.1. Effect of Working Fluid

One of the factors responsible for the non-repeatability of the test results was assumed to be impurities in the working liquid or inside the system itself. High-purity

nitrogen was used in this research; however, there was still the possibility of impurity molecules entering the system during the liquid charging process. Dissociation of impurity molecules creates numbers of positive and negative ions, which, under the influence of an electric field, can not only lead to additional input power requirements for the pump, but can also affect the net force on the liquid and alter the pressure head (Crowley et al., 1990).

Since only limited studies have been conducted on the EHD pumping phenomenon in LN_2, author's knowledge was limited to those carried out on the electrochemical behavior of LN_2 under an intense electric field. Byatt and Secker (1968) did not find the conduction current data in LN_2 to be accurately repeatable from day to day. Comparing their data from air and LN_2, they found oxygen ions responsible for most of the inaccuracy observed. Halpern and Gomer (1969b), in their paper on the Field Ionization in Liquids, reported "erratic and noisy emission at low currents" and that "it was not possible to see a well-defined tunneling regime" in LN_2. Nitrogen is in fact a very inert substance, but impurity molecules that enter the system and which might get dissolved in the working liquid can substantially change electrochemical properties of the liquid and cause non-repeatable test results for consecutive runs.

Generally, in ion-drag EHD pumps, high electric field gradients can affect the liquid molecular structure and cause corrosion of the electrodes, which can affect run-to-run repeatability and reduce the pump's lifetime. For this reason, liquid nitrogen was expected to be a better choice for ion drag pumping compared to other refrigerants since its molecular structure is highly stable. However, during system charging, there is no practical way to prevent all contaminants (including dissolved gases) from entering into

the system. Depending on the nature of contaminants, under high electric voltage, the impurity molecules can become ionized and add an unidentified number of ions into the system or even lead to electric discharges. The electric discharges can result in a local increase in temperature and eventually melted spots of electrode (Figure 4-5).

6.2.5.2. Electrode Degradation

Another factor responsible for the uncertainty of the result is the gradual degradation of the electrodes. The corrosion of the metal electrodes under the local intense electric field can substantially change the electrochemical properties of the liquid by increasing the liquid impurity level. At the same time, it decreases the sharpness of the electrodes, resulting in fewer ion-injection sites.

As explained in Chapter 4, in working with LN_2, no sign of oxidation was detected on the electrodes, however in many occasions, melted spots on the electrodes were observed. To reduce this effect, it was decided to fabricate platinum electrodes. However, Pt due to its hardness is very difficult to etch and work with. For that, a method of electroplating was developed to electroplate the already-fabricated gold electrodes with a layer of platinum. Preliminary test results of a couple of prototypes demonstrated a lower level of electrode degradation; however, more tests need to be performed for further analysis. Therefore, it is believed that platinum-plated electrodes can increase the lifetime of the micropumps by strengthening the electrodes.

6.3. Flow-rate Measurement Results

To measure the flow rate of a micropump, the pump was placed in the flow rate measurement test setup. The tests were begun by applying DC voltages to the

micropump. The generated flow rate was measured using an energy balance technique in which a certain amount of heat was applied to the system and the temperatures upstream and downstream of the heater were measured. The temperature difference was later related to flow rate using a calibration curve. The detail regarding the test setup characteristics and flow measurement techniques were explained in Chapter 5. During the experiments, the amount of applied heat was adjusted to avoid boiling the liquid nitrogen but sufficient to generate a reasonable downstream-upstream temperature difference.

A micropump with (50,200,s) design (D_{el} = 50 μm, D_{pel} = 200 μm, saw-tooth emitter and flat collector) with H_{ch} = 260 μm was tested at a DC voltage of 1000 V. The first test was a transient test in which about 0.14 W of power was supplied to the heater for about 60 seconds. The response of the upstream and downstream thermocouples is shown in Figure 6-12. The downstream temperature of the fluid increased, while the upstream temperature remained constant after the pulse of heat. This asymmetrical response indicates that liquid nitrogen was being pumped around the loop.

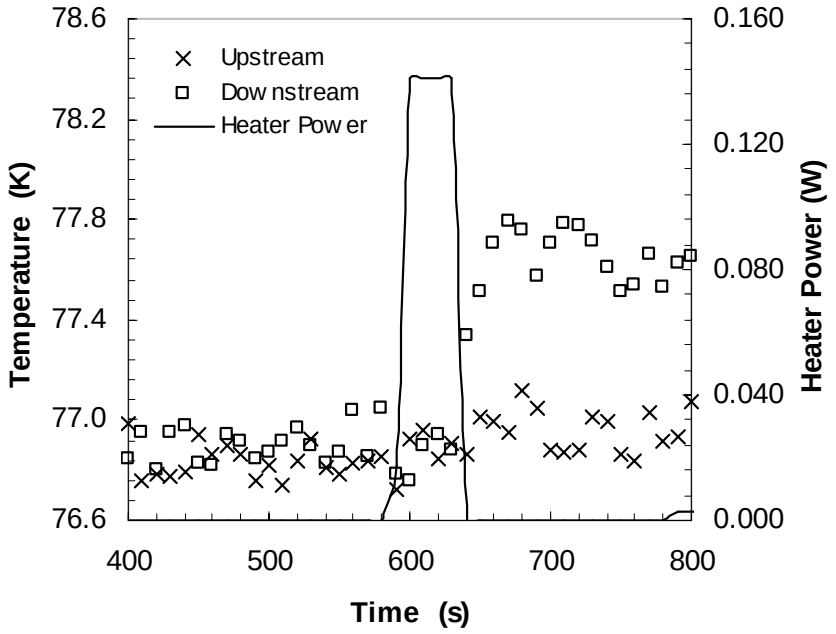

Figure 6-12 Response of TC1 and TC2 readings to a heat pulse when a (50,200,s) micropump is being tested at 1000 V.

The response of the upstream and downstream thermocouples to a different type of test in which the heater was temporarily turned off and restarted is shown in Figure 6-13. In that test, a heat of 0.068 W was being supplied by the heater long enough to reach steady state. Then, the heater was turned off for about 1000 seconds. As soon as the heater was turned off, the temperature difference between the upstream and downstream locations returned to zero. Also, as soon as the heater was turned back on, a difference in temperature was established between the upstream and downstream locations. During the test, the applied voltage was held constant at 1000 V. The fact that the only downstream fluid temperature was affected by the heater power and the upstream fluid temperature remained fairly constant was further proof that the liquid nitrogen was being pumped around the loop by the micropump.

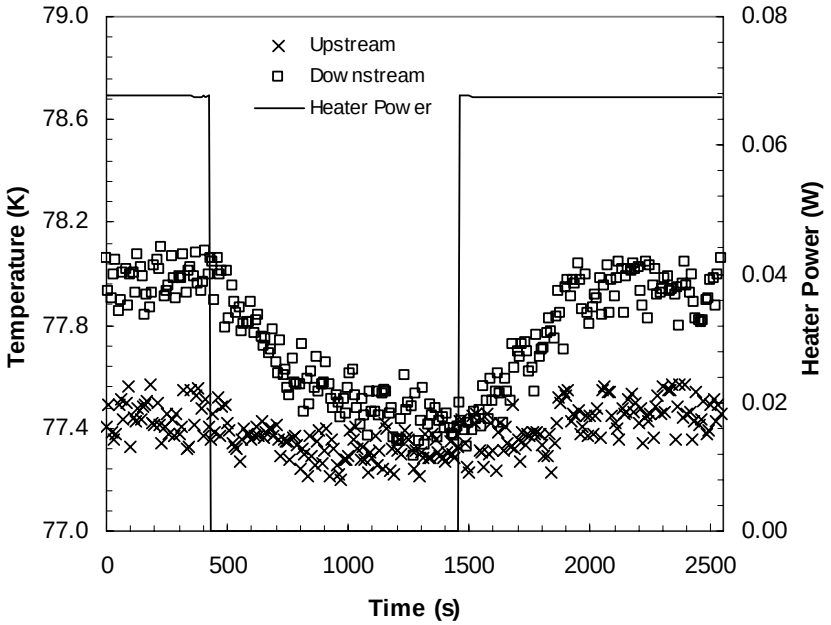

Figure 6-13 Experimental results of a (50,200,s) micropump tested at 1000 V, TC1 and TC2 readings vs. time

The difference in these two temperatures corresponded to a flow rate of 5±2 ml/min based on the flow rate calibration curve. That flow rate was enough to overcome a pressure drop of 13±3 Pa inside the flow loop based on the pressure drop-flow rate calibration curve. The product of the pressure head and flow rate is defined as the pumping power of the micropump, which for this case is 1.1×10^{-6} Pa.m^3/s.

6.4. Conclusions

In previous sections, the P-I and P-V characteristics curves were defined, and their parameters and coefficients for various designs were plotted. Using those parameters, two performance curves were created for every design, as shown in Figure 6-14 and Figure 6-15. For the sake of simplicity, the error bars are not marked on these graphs; however, their average values can be found in Figure 6-8 and Figure 6-10.

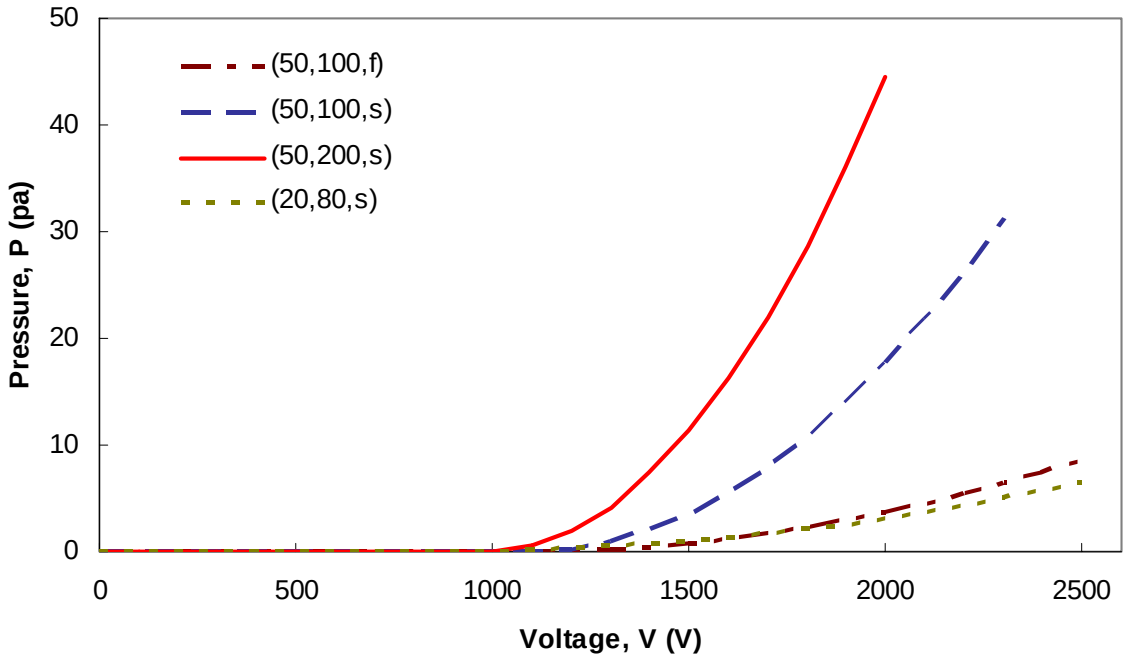

Figure 6-14 Pressure head generation for various designs predicted by the empirical model

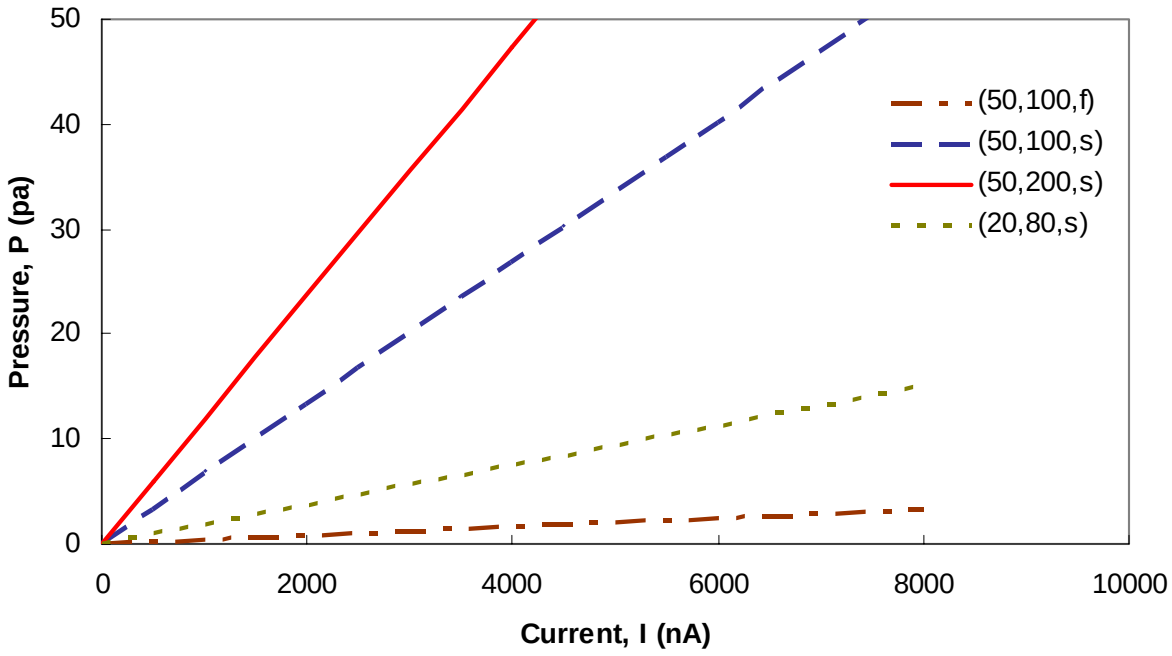

Figure 6-15 Pressure head versus generated current for various designs predicted by the empirical model

One may define the best design as the one that begins pumping at the lowest onset voltage and yet generates the highest pressure head. The (20,80,s) design operates with

the least onset voltage but does not generate an acceptable pressure head compared to the rest of the designs. The (50,200,s) design, followed closely by the (50,100,s), generates the highest pressure head with an onset value slightly higher than that of the (20,80,s). Nevertheless, the benefit of generating a high pressure head seems to compensate well for its higher onset value; therefore, (50,200,s) is selected as the most successful design.

Also based on the above discussion, an alternative prototype can be designed as (20,200,s), combining the inter-electrode spacing of (20,80,s) for a low onset value and the pair spacing of (50,200,s) for a high pressure head. However, a downfall of such low inter-electrode spacing might be the possibility of dielectric breakdown at a DC voltage of about 1800 V, which was frequently seen with (20,80,s) design.

CHAPTER 7: CONCLUDING REMARKS AND FUTURE WORK

7.1. Concluding Remarks

This dissertation presented a theoretical and experimental study on micropumping of liquid nitrogen, which has a wide range of applications in cryogenic liquid cooling devices, as well as in bioengineering applications where a small dose of LN_2 needs to be delivered to a particular spot. To the best knowledge of the author, this study was the first of its kind to thoroughly characterize an EHD micropump for working with cryogenic working liquids such as liquid nitrogen (LN_2). Following is a summary of the major accomplishments of this work:

- A selective literature survey on EHD ion-drag/ion-injection pumps in two main areas of application, ambient temperature and cryogenic, was conducted.
- The theoretical fundamentals of the EHD pumping phenomena and relevant governing equations were reviewed.
- Fundamentals of generation and transport of electric charge carriers in nonpolar liquids, e.g. liquid nitrogen, under the influence of intense electric field were reviewed.
- The energy barriers for positive and negative voltage polarities (i.e. field ionization and field emission, respectively) at different metal/liquid interfaces, i.e., Au/LN_2 and Au/Pt, were determined using the method suggested by Arii and Schmidt (1984).

- The design requirements for an ion-drag micropump were introduced, based on which several prototypes were fabricated. A finished micropump consisted of a substrate on which metal electrodes were deposited, a top-cover which provided the substrate with a flow channel, and a bottom plate.
- Details on the thin-film deposition and photolithography-etching techniques, employed to create several contiguous metallic electrode pairs on the substrate, were explained.
- A method of electroplating was developed to electroplate the already-made gold electrodes with a layer of platinum.
- A packaging technique compatible with a cryogenic environment was developed.
- A series of prototypes with various designs was selected to evaluate the effect of geometrical parameters on the performance.
- Two test rigs were designed and built for flow rate and static pressure head measurement purposes.
- A technique based on the heat balance was developed to measure the volumetric fluid flow rate.
- Experiments were performed by applying DC voltages to the prototypes while the generated current and pressure were measured.
- The relationships between pressure/current (P-I) and pressure/voltage (P-V) for various designs were investigated experimentally. The results showed good agreement with the general analytical trends reported for EHD pumping in the literature.

- The experimental results demonstrated that decreasing the distance between electrodes was effective in decreasing the pressure onset voltage; however, this did not always lead into higher pressure heads, since small electrode gaps caused the electric breakdown to start at a lower voltage.
- Three repetitive operation stages were recognized during experiments: the initial, the intermediate, and the final stage.

7.2. Future Work

The major recommendation for future work on this study is to reduce the uncertainty involved with the experimental results and to improve the life of the micropumps. The main sources of uncertainty seen in the results are believed to be impurity molecules in the working liquid and microscopic differences existing in the electrode structure. To address the issues, it is worthwhile to consider the following recommendations:

- The electrodes were fabricated manually on campus. Although all the electrodes were visually inspected before being tested, but there was no way to detect and control microscopic defects. Those microscopic defects are to be blamed for much of the uncertainty. Batch-fabrication of the electrodes is therefore recommended to lowering the uncertainty.
- The second most important source of uncertainty was the impurity molecules entering the system from outside during liquid charging process, or the impurity molecules detaching from the electrode surface and entering the liquid. To address the issue, the system, for example, could be charged in a high-quality clean room where there is less impurity.

- Another factor responsible for the uncertainty of the results was the gradual degradation of the electrodes. As explained in Chapter 4, a method of electroplating was utilized to electroplate the already-made gold electrodes with a layer of platinum. Experiments on a couple of samples demonstrated much less electrode degradation. Therefore, it is believed that platinum-plated electrodes would be a valuable option in further development of EHD micropumps.
- Based on the results shown in Chapter 6, an alternative prototype can be designed as (20,200,s), combining the inter-electrode spacing of (20,80,s) for a low onset value and the pair spacing of (50,200,s) for a high pressure head. However, a downfall of such low inter-electrode spacing might be the possibility of dielectric breakdown at a low DC voltage.
- And finally, it is recommended to develop a new packaging method on which multiple substrates can be stacked so as to generate more pressure.

REFERENCES

Ahn, S. H., and Kim, Y. K., 1998, "Fabrication and Experiment of Planar Micro Ion Drag Pump," Sensors and Actuators A: Physical, **70**(1-2): 1-5.

Asano, K., and Yatsuzuka, K., 1999, "Fundamental Study of EHD Pump with Needle-Cylinder Electrodes," *Proc. IEEE Conference on Electrical Insulation and Dielectric Phenomena, 1999*: 785-788.

ASHRAE Handbook, 2001, *Fundamentals*, SI Edition, Refrigerant 729 (air), 20.59.

Arii, K., and Schmidt, W. F., 1984, "Current Injection and Light Emission in Liquid Argon and Xenon in a Divergent Electric Field," IEEE Transactions on Electrical Insulation, **19**(1): 16-23.

Avsec, D., and Luntz, M., 1936, Comptes-Rendus Paris, **203**: 1140.

Avsec, D., and Luntz, M., 1937, Comptes-Rendus Paris, **204**: 420.

Avsec, D., and Luntz, M., 1939, Comptes-Rendus Paris, **208**: 1886.

Barbini G., Coletti G., 1995, "Influence of Electrode Geometry on Ion-drag Pump Static Pressure," IEEE Transactions on Dielectric and Electrical Insulation, **2** (6): 1100-5.

Benetis, V., 2005, "Experimental and Computational Investigation of Planar Ion Drag Micropump Geometrical Design Parameters," Ph.D. Dissertation, University of Maryland, College Park, USA.

Benetis, V., Shooshtari, A., Foroughi, P., and Ohadi, M. M., 2003, "A Source-Integrated Micropump for Cooling of High Heat Flux Electronics," *19th Annual IEEE Semi-Therm Symposium, March 2003*, 236 – 241.

Bologa, M. K., Kozhevnikov, I. V., and Kozhukhari, I. A., 2000, "Multistage Electrohydrodynamical Pump," *Proc. IEEE Conference on Electrical Insulation and Dielectric Phenomena*, 2000: 57-60.

Born, M., 1920, "Volumen und Hydratationswarme der Ionen," Z. Physik, **1**: 45-48.

Boyarintsev, V. I., Kuznetsov, S. F., Molotov, P. E., and Parinov, Yu. V., 1992, "Investigation of the EHD Effect in Liquid Nitrogen," translated from Inzhenerno-Fizichezkii Zhurnal, October 1992, **63** (4): 387-392.

Bryan, J.E., and Seyed-Yagoobi, J., 1991, "Experimental Study of Ion-drag Pumping Using Various Working Fluids," IEEE Transactions on Electrical Insulation, **26** (4): 647-55.

Bryan, J.E., and Seyed-Yagoobi, J., 1992, "An Experimental Investigation on Ion-drag Pump in a Vertical and Axisymmetric Configuration," IEEE Transactions on Industry Applications, **28**: 310-16.

Butcher, M. D., 2005, "Mechanisms of Charge Conduction and Breakdown in Liquid Dielectrics," Ph.D. Dissertation, Texas Tech University, USA.

Byatt, S. W., and Secker, P. E., 1968, "Electrical Conduction in Liquid Air and Liquid Nitrogen," British Journal of Applied Physics, **2**(1): 1011-1017.

Castellanos, A., 1991, "Coulomb-driven Convection in Electrohydrodynamics," IEEE Transactions on Electrical Insulations, **26**(6): 1201-1215.

Castellanos, A., 1998, *Electrohydrodynamics*, New York, Springer-Verlag.

Chen, C.-L., Selvarasah, S., Chao, S.-H., Khanicheh, A., Mavroidis, C. and Dokmeci, M. R., 2007, "An Electrohydrodynamic Micropump for On-Chip Fluid Pumping on

Flexible Parylene Substrates," *Proc. IEEE NEMS Conference, Bangkok*, Thailand 2007: 826-29.

Coelho, R., and Sibillot, P., 1969, "Direct Current Pre-breakdown Phenomena in Liquid Nitrogen," Nature, **221**(5182): 757.

Coletti, G., and Bozzo R., 1996, "A Contribution to the Evaluation of Electrohydrodynamic Pumps for Insulating Oils," *Annual Report of the 1996 IEEE Conference on Electrical Insulation and Dielectric Phenomena*.

CRC, 1997, *Handbook of Chemistry and Physics*, 77th, Cleveland, Ohio, CRC Press.

Crowley, J. M., Wright, G. S., and Chato, J.C., 1990, "Selecting a Working Fluid to Increase the Efficiency and Flow Rate of an EHD Pump," IEEE Transactions on Industry Applications, **26**(1): 42-49.

Darabi, J., 1999, "Micro and Macro Scale Electrohydrodynamic Enhancement of Thin-Film Evaporation," Ph.D. Dissertation, University of Maryland, College Park, USA.

Darabi, J., Rada, M., Ohadi M. M., and Lawler, J., 2002, "Design, Fabrication, and Testing of an Electrohydrodynamic Ion-Drag Micropump," J. Microelectromechanical Systems, **11**: 684-690.

Darabi, J., and Wang, H., 2005, "Development of an EHD Injection Micropump and Potential Application in Pumping Fluids in Cryogenic Cooling Systems," Journal of Microelectromechanical Systems, **14** (4): 747-755.

Denat, A., Jomni, F., Aitken, F., and Bonifaci, N., 1999, "Generation of Bubbles in Liquid Argon and Nitrogen in Divergent Electric Fields," *Proc. 13th Int'l Conference on Dielectric Liquids*, Japan, July 99: 384-387.

Doake, C.S.M., and Gribbon, P.W.F., 1971, "Ion Motion in Liquid Nitrogen," J. Phys. A: Gen. Phys., **4**: 952-961.

Foroughi, P., Benetis, V., Ohadi, M., Zhao, Y., and Lawler, J., 2005, "Design, Testing and Optimization of a Micropump for Cryogenic Spot Cooling Applications," *21st Annual IEEE Semi-Therm Symposium*, 15-17 March 2005: 335 – 340.

Foroughi, P., Dessiatoun, S., Shooshtari, A., and Ohadi, M., 2007, "Experimental Characterization of an EHD Ion-Drag Micropump for Cryogenic Micro-pumping Applications," *Proc. 2007 ASME International Mechanical Engineering Congress and Exposition*, Seattle, Washington, IMECE2007-42177.

Frayssines, P. E., Bonifaci, N., Denat, A., and Lesaint, A., 2002, "Streamers in Liquid Nitrogen: Characterization and Spectroscopic Determination of Gaseous Filament Temperature and Electron Density," J. Physics D, **35**: 369-377.

Freeman, G. R., 1987, *Kinetics of Nonhomogeneous Processes*. New York, John Wiley & Sons.

Gallagher, T. J., 1975, *Simple Dielectric Liquids: Mobility, Conduction, and Breakdown*. Oxford [Eng.], Clarendon Press.

Gee, N., Floriano, A. M., Toshinori, W., Huang S. S., and Freeman G.R., 1985, "Ion and Electron Mobilities in Cryogenic Liquids: Argon, Nitrogen, Methane, and Ethane," Journal of Applied Physics, **57** (4): 1097-1101.

Gemant, A., 1929, Electrotech. Zeit., **34**: 1225.

Gray, E. and Lewis, T.J., 1969, "The Effect of Liquid Motion on Ion Mobility in Hexane," British Journal of Applied Physics, **2** (2): 93-100.

Halpern, B., and Gomer, R., 1969a, "Field Emission in Liquids," J. of Chem. Phys., **51** (3): 1031-1047.

Halpern, B., and Gomer, R., 1969b, "Field Ionization in Liquids," J. of Chem. Phys., **51** (3): 1048-1056.

Hanaoka, R., Ishibashi, R., Kasama, M., Uchiyama, A., and Kawaguchi, A., 1993, "Pre-Breakdown Current in Liquid Nitrogen under DC Nonuniform Field," Nuclear Instruments and Methods in Physics Research Section A, **327** (1): 107-110.

Haus, H. A., and Melcher J. R., 1998, *6.013 Electromagnetism*, Chapter 7.7., http://web.mit.edu/6.013_book/www/book.html.

Hofmann, R., 1934, Z. Physik, **92**: 759.

Holroyd, A., and Schmidt, W. F., 1989, "Transport of Electrons in Nonpolar Fluids," Annual Review of Physical Chemistry, **40**: 439-68.

IEEE-DEIS-EHD Technical Committee, 2003, "Recommended International Standard for Dimensionless Parameters Used in Electrohydrodynamics," IEEE Transactions on Dielectrics & Electrical Insulation, **10**(1): 3-6.

Incropera, F. P., and DeWitt, D. P., 2002, *Fundamentals of Heat and Mass Transfer*, 5th Edition, John Wiley & Sons.

Jackson, J. D., 1999, *Classical Electrodynamics*, New York, Wiley.

Jones, H.M., and Kunhardt, E.E., 1994, "Development of Pulsed Dielectric Breakdown in Liquids", J. Phys. D: Appl. Phys., **28**: 178-188.

Kattan, R., Denat, A., and Lesaint, O., 1991, "Formation of Vapor Bubbles in Non-polar Liquids Initiated by Current Pulses," IEEE Trans. on Electrical Insulation, **26** (4): 656-662.

Krahenbuhl, F., Bernstein, B., Danikas, M., Densley, J., Kadotani, K., Kahle, M., Kosaki, M., Mitsui, H., Nagao, M., Smit, J, and Tanaka, T., 1994, "Properties of Electrical Insulating Materials at Cryogenic Temperatures: a Literature Review," IEEE Electrical Insulation Magazine, **10**(4): 10-22.

Lewis, T. J., 1994, "Basic Electrical Processes in Dielectric Liquids," IEEE Transactions on Dielectrics & Electrical Insulation, **1**(4): 630-643.

McClintock, P. V. E., 1973, "Field Emission and Field Ionization in Liquid ^{3}He above 0.25 K," Journal of Low Temperature Physics, **11** (1-2): 15-31.

McCluskey, F.M.J., and Denat, A., 1996, "The Behavior of Small Bubbles Generated by Electrical Current Impulses over a Wide Range of Applied Pressures," J. Appl. Phys., **80**: 2049-2059.

Melcher, J. R., 1981, *Continuum Electromechanics*, Cambridge, Mass., MIT Press.

Melcher, J. R., and Taylor, G. I., 1969, "Electrohydrodynamics: A Review of the Role of Interfacial Sheer Stresses," Annual Review of Fluid Mechanics, **1**: 111-146.

Middendorf, W. H., and Brown, G. H., 1958, Trans. AIEE, Power and Systems, **77** (III): 795.

Mirotvorsky, V. O., and Y. K. Stishkov, 1996, "Influence of Near-Electrode Reaction on Distribution of Electric Characteristics of Electrodes-Liquid Dielectric System," *12th International Conference on Conduction and Breakdown in Dielectric Liquids (ICDL)*, 1996.

Moeller, T., 1982, *Inorganic Chemistry: A Modern Introduction*, New York, Wiley.

Nosseir, A., and Megahed, I., 1970, "Pre-Breakdown Conduction Current Pulses in Insulating Oils under Non-Uniform Field Conditions", J. Phys. D: Appl. Phys., **3**: 1205-1211.

Ohadi, M.M., Darabi, J., and Roget, B., 2001, "Electrode Design, Fabrication, and Materials Science for EHD-Enhanced Heat and Mass Transport," Annual Review of Heat Transfer, **11**: 563-623.

Ostroumov, G. A., 1954, J. Tech. Phys., USSR, **24**: 1915.

Panofsky W. K. H., and Phillips, M., 1962, *Classical Electricity and Magnetism*, Addison-Wesley Publishing Company.

Pickard, W. F., 1963a, "Ion-Drag Pumping: I Theory," J. Appl. Phys., **34** (3): 246–250.

Pickard, W. F., 1963b, "Ion-Drag Pumping: II Experiment," J. Appl. Phys., **34** (3): 251–258.

Pompili, M., and Mazzetti, C., 1995, "Early Stages of Negative PD Development in Dielectric Liquids," IEEE Trans. on Dielectrics and Electrical Insulation, **2**(4): 602-613.

Rada, M., 2004, "Electrohydrodynamics (EHD) Pumping of Liquid Nitrogen – Application to Spot Cryogenic Cooling of Sensors and Detectors," Ph.D. Dissertation, University of Maryland, College Park, USA.

Ramanan, G., and Freeman, G. R., 1987, "Electron Thermalization Distances and Free Ion Yields in Liquid Nitrogen From 77K to Near T_c," J. Chem. Phys., **57** (1): 319-324.

Richter, A., Plettner, A., Hofmann, K. A., and Sandmaier, H., 1991, "A Micromachined Electrohydrodynamic (EHD) Pump," Sensors and Actuators, **29:** 159-168.

Schmidt, W. F., 1991, "Electrons in Nonpolar Dielectric Liquids," IEEE Transactions on Electrical Insulation, **26**(4): 560-567.

Schmidt, W. F., 1997, *Liquid State Electronics of Insulating Liquids*, New York, CRC Press.

Schmidt, W. F., 1999, "Electrons, Holes and Ions in Non-Polar Dielectric Liquids," *Proc. 13th International Conference on Dielectric Liquids*, Nara, Japan.

Sharbaugh, H. A., and Walker, G. W., 1985, "The Design and Evaluation of an Ion-drag Dielectric Pump to Enhance Cooling in a Small Oil-filled Transformer," IEEE Transactions on Industry Applications, **21**: 950-5.

Shooshtari, A., 2004, "Experimental and Computational Analysis of an Electrohydrodynamic Mesopump for Spot Cooling Applications," Ph.D. Dissertation, University of Maryland, College Park, USA.

Stratton, J. A., 1941, *Electromagnetic Theory*, New York, London, McGraw-Hill Book Company, Inc.

Stuetzer, O. M., 1959, "Ion Drag Pressure Generation," J. Appl. Phys., **30** (7): 984–994.

Stuetzer, O. M., 1960, "Ion Drag Pumps," J. Appl. Phys., **31** (1): 136–146.

Sugimoto, H., Nishikawa, T., Tsuda, T., Hondou, Y., Akita, Y., Takeda, T., Okazaki, T., Ohashi, S., and Yoshida, Y., 2006, "Trial Manufacture of Liquid Nitrogen Cooling High Temperature Superconductivity Motor," Journal of Physics, **43**: 780-783.

Takashima, T., Hanaoka, R., Ishibashi, R., and Ohtsubo, A., 1988, "I-V Characteristics and Liquid Motion in Needle-to-Plane and Razor Blade-to-Plane Configurations

in Transformer Oil and Liquid Nitrogen," IEEE Transactions on Industrial Insulation, **23** (4): 645- 658.

Tobazeon, R., 1984, "Electrohydrodynamic Instabilities and Electroconvection in the Transient and A.C. Regime of Unipolar Injection in Insulating Liquids: a Review," Journal of Electrostatics, **15**: 359-384.

Tobazeon, R., 1994, "Prebreakdown Phenomena in Dielectric Liquids," IEEE Trans. on Dielectrics and Electrical Insulation, **1**(6): 1132-1147.

Walker, G., Ellison, W., and Zylstra, S., 1988, "Cryocoolers for the New High-Temperature Superconductors," Journal of Superconductivity, **1**(2): 197-209.

Wikipedia, The Free Encyclopedia, "Dielectric Breakdown", http://en.wikipedia.org/wiki/Dielectric_breakdown, accessed October 2007.

Wikipedia, The Free Encyclopedia, "Electrohydrodynamics", http://en.wikipedia.org/wiki/Electrohydrodynamics, accessed October 2007.

Wong, C. C., Chu, D., Liu, S. L., Tuck, M. R., Mahmud, Z., and Amatucci, V., 1995, "Rapid Prototyping of a Micro Pump with Laser Micromachining," *Proc. SPIE: Micromachined Devices and Components*.

Yanada, H., Hakama, S., Miyashita, T. and Zhanet, N., 2002, "An Investigation of an Ion Drag Pump Using a Needle-Mesh Electrode Configuration," Proceedings of the Institution of Mechanical Engineers, Part C: Journal of Mechanical Engineering Science, **216**(3): 325-334.

Yang, L.-J., Wang, J.-M., and Huang, Y.-L., 2003, "The Micro Ion Drag Pump Using Indium-Tin-Oxide (ITO) Electrodes," *IEEE 16th Annual International Conference on MEMS*, 2003: 112-115.

Zhao, Y., Foroughi, P., Lawler, J., and Ohadi, M., 2003, "Development of an Electrohydrodynamic (EHD) Micro Pump for LN2 Spot Cooling," *Proceedings of the 2003 ASME International Mechanical Engineering Congress and Exposition*, Washington, D.C., Nov. 2003, IMECE2003-55625.